Ph.D. Thesis

Wideband observation of radio pulsars towards detection of low-frequency gravitational waves

Author: **Tomonosuke Kikunaga**
ID: **211-D9021**
Supervisor: **Prof. Keitaro Takahashi**

Graduate School of Science and Technology (GSST)
Kumamoto University

March, 2024

Abstract

In 2015, gravitational waves (GWs) were detected for the first time by the US laser interferometer LIGO. The source of these GWs are black hole (BH) binaries of stellar mass which radiate GWs with frequency of 100 Hz-10 kHz. On the other hand, there are Supermassive BHs (SMBHs) in the universe with masses more than one billion times the mass of the Sun. A SMBH binary is thought to radiate low-frequency GWs in the nHz-μHz range, which does not correspond to the frequency range observed by laser interferometers such as LIGO. BHs of stellar mass magnitude are known to be formed by stellar supernova explosions, but the formation process of SMBHs is still a mystery. Therefore, the detection of gravitational waves emitted from them is expected to provide information on the evolution of SMBHs. One method for detecting these low-frequency gravitational waves is the Pulsar Timing Array (PTA). PTA aims to detect gravitational waves by using celestial objects called pulsars as clocks. Pulsars are objects that are observed as periodic pulses, and pulses can be observed with a stable period. Millisecond pulsars with millisecond-scale pulse periods are particularly stable, and the arrival time of these pulses can be accurately predicted. However, it has been observed that pulse arrival times deviate from predictions due to mechanisms other than gravitational waves, and clarification of such deviations and understanding of the mechanisms that emit the pulses will be important for future gravitational wave detection. In this paper, we describe a radio observation study of pulsars aimed at understanding the noise in pulse arrival times for the coming era of low-frequency gravitational wave astronomy.

In Chapter 2, we describe a method to constraint on ultra-low frequency GWs from an eccentric SMBH binary. Millisecond pulsars with highly stable periods can be considered as very precise clocks and can be used for PTAs, which attempt to detect nanohertz GWs directly. The main sources of nanohertz GWs are SMBH binaries with sub-parsec-scale orbits. On the other hand, an SMBH binary in an earlier phase with a parsec-scale orbit emits ultra-low-frequency ($<$ nHz) GWs and cannot be detected with the conventional PTA methodology. Such binaries tend to attain high eccentricity, possibly $\sim$0.9. In this chapter, we develop a formalism for extending the constraints on GW amplitudes from single sources obtained by PTAs toward ultra-low frequencies considering the waveform expected from an eccentric SMBH binary. GWs from eccentric binaries are contributed from higher harmonics and therefore have a different waveform to those from circular binaries. Furthermore, we apply our formalism to several hypothetical SMBH binaries at the centre of nearby galaxies, including M87, using the constraints from NANOGrav's 11-yr data set. For a hypothetical SMBH binary at the centre of M87, the typical upper limit on the mass ratio is 0.16 for an eccentricity of 0.9 and a semimajor axis of $a = 1$ pc, assuming the binary phase to be the pericentre.

In chapter 3, we describe pulse jitter measurements of PSR J0437$-$4715 with the upgraded Giant Metrewave Radio Telescope (uGMRT). High-precision pulsar timing observations are limited in their accuracy by the jitter noise that appears in the arrival time of pulses. Therefore, it is important to systematically characterise the amplitude of the jitter noise and its variation with frequency. In this paper, we provide jitter measurements from low-frequency wideband observations of PSR J0437$-$4715 using data obtained as part of the Indian Pulsar Timing Array experiment. We were able to detect jitter in both the 300 - 500 MHz and 1260 - 1460 MHz observations of the uGMRT. The former is the first jitter measurement for this pulsar below 700 MHz, and the latter is in good agreement with results from previous studies. In addition, at 300 - 500 MHz, we investigated the frequency dependence of the jitter by calculating the jitter for each sub-banded arrival time of pulses. We found that the jitter amplitude increases with frequency. This trend is opposite as compared to previous studies, indicating that there is a turnover at intermediate frequencies. It will be possible to investigate this in more detail with uGMRT observations at 550 - 750 MHz and future high sensitive wideband observations from next generation telescopes,

such as the Square Kilometre Array. We also explored the effect of jitter on the high precision dispersion measure (DM) measurements derived from short duration observations. We find that even though the DM precision will be better at lower frequencies due to the smaller amplitude of jitter noise, it will limit the DM precision for high signal-to-noise observations, which are of short durations. This limitation can be overcome by integrating for a long enough duration optimised for a given pulsar.

In chapter 4, we describe spectropolarimetric observation of the bright radio emissions from PSR J1107−5907. Using single pulse and folded observations of PSR J1107−5907 with the Parkes (*Murriyang*) radio telescope, we provide a wide-bandwidth (704–4032 MHz) analysis of the pulsar in its bright state. We compare the folded pulse profiles with previous narrower-band observations and present phase-resolved measurements of the spectral index, polarisation properties, and rotation measure. We analyse 500- individual pulses. These pulses provide a wealth of information including modulation indices, polarisation properties, spectral index distribution, wide-band pulse shape evolution, etc. We compare the properties of those pulses to the emission from magnetars and, in particular, explore the implications of orthogonal emission modes detected in the single pulse data stream.

Contents

List of Tables

List of Figures

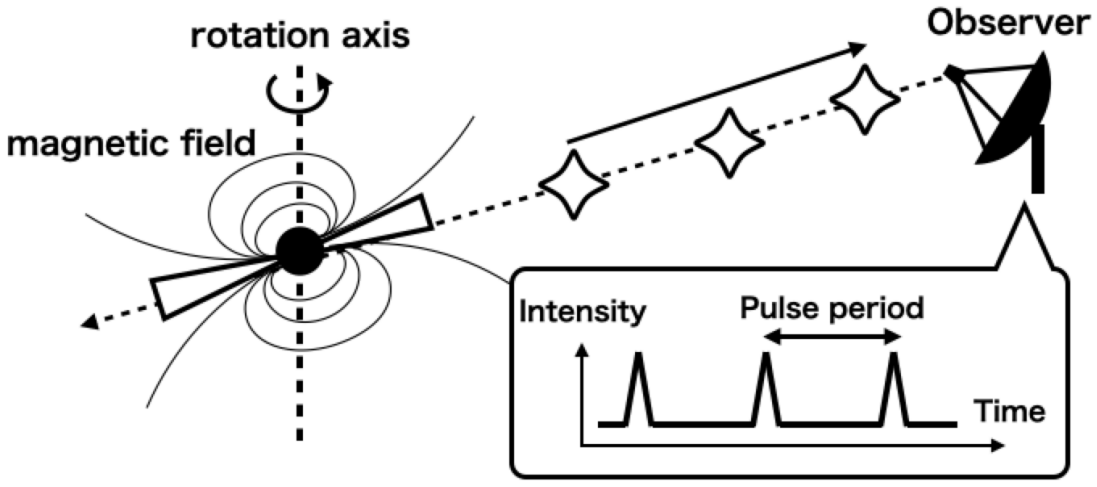

Figure 1: A schematic view of pulsar observation.

1 Introduction

1.1 Gravitational Waves

In Einstein's general theory of relativity, time and space are treated as a unified four-dimensional space-time, and the gravitational field is interpreted as a distortion of space-time. The equation of the gravitational field is described by the Einstein equation

$$G_{\mu\nu} = R_{\mu\nu} - \frac{1}{2}Rg_{\mu\nu} = \frac{8\pi G}{c^4}T_{\mu\nu}, \tag{1}$$

where, $G_{\mu\nu}$ is Einstein tensor, $R_{\mu\nu}$is Ricci tensor $R = R^{\mu}_{\mu}$ is Ricci scalar $g_{\mu\nu}$ is the metric of the spacetime, and $T_{\mu\nu}$ is the energy-momentum tensor. The Einstein tensor on the left hand side represents the spacetime distortion, and the energy-momentum tensor on the right side represents the matter distribution. This means that where an object is located, there is a distortion of space-time and a gravitational field, and if the object moves, the distortion of space-time will fluctuate. This distortion propagates as waves and therefore is called gravitational waves (GWs). GWs are generated by the motion of objects, but their amplitude is so small that they are impossible to detect, and they are considered to exist only theoretically.

A turning point came in 1974. A binary pulsar was discovered by Russel Hulse and Joseph Taylor (Hulse and Taylor, 1975). Pulsars are objects that are observed as periodic pulses (see Figure 1), and the change in their orbits can be measured by continuously measuring the arrival time of pulses. In such a highly relativistic system, orbital changes due to GWs can be measured. The changes in their orbital periods were consistent with the changes predicted by general relativity (see Figure 2). This indirectly proved the existence of GWs, and efforts toward the direct detection of GWs began in earnest.

In September 2015, the direct detection of GWs was finally accomplished by Laser-interferometric GWs detector, LIGO (Abbott et al., 2016). The GWs was radiated by the merging of black hole (BH) binary. This

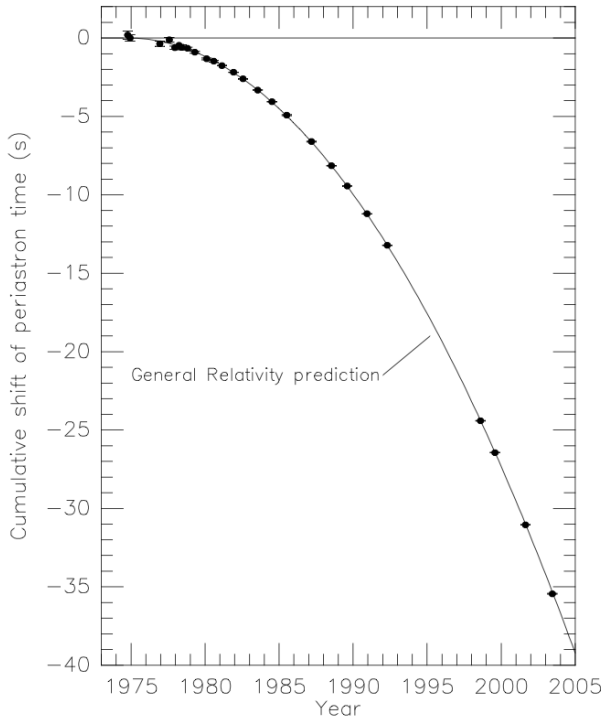

Figure 2: Orbital decay of PSR B1913+16. Black points indicate observed decay (Weisberg and Taylor, 2005), and the solid line shows theoretical prediction.

confirmed the existence of GWs and opened the door to GW astronomy. Because the waveform of the GW represents the orbit of the BH binary, we can "see" the merging of BH binary in detail, which cannot be observed with light.

The target of LIGO are GWs of about 1 Hz to 10 kHz, which are emitted from a stellar mass BH binary. On the other hand, BHs of various masses exist in our universe. In particular, Supermassive Blackholes (SMBHs), which exist at the centers of a galaxy, typically have masses of about $10^6 - 10^9$ solar masses. SMBHs are thought to grow by forming binary and merging in the process of reaching that mass. However, the merging process is thought to take longer than the age of the universe, which cannot explain the mass of the SMBHs that exist today. Therefore, direct observation of GWs from SMBH binaries to investigate how their orbits are contracting is also important for studying the evolution of SMBH binary. However, GWs from SMBH binaries are thought to be at nHz - μHz, which cannot be detected by laser interferometers such as LIGO. Therefore, it is necessary to observe such GWs with a different observation method.

1.2 Pulsar Timing Array

Pulsar Timing Array (PTA) is a method expected for detecting GWs in the nHz - μHz range within a few years (Foster and Backer, 1990a). PTA aims to detect GWs by observing pulsars with very stable period. Millisecond pulsars (MSPs), which emit pulses with a millisecond period, are particularly stable, and their typical variation rate of period is about 10^{-20} (see Figure 4). PTA aims to detect gravitational waves by using the arrival time of millisecond pulsar pulses as a clock. PTA detects GWs by observing MSPs once every

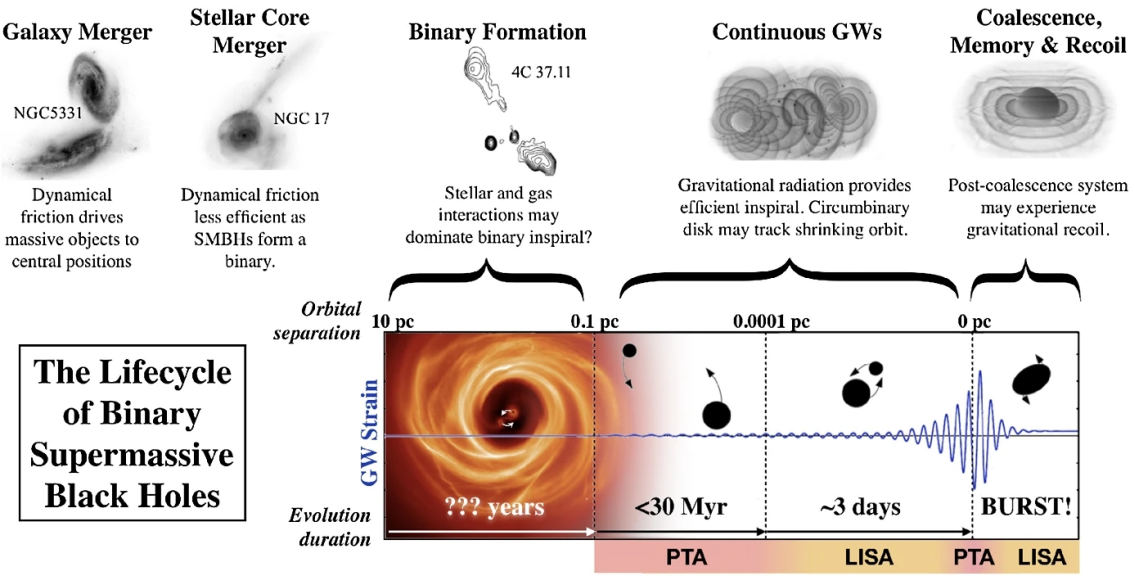

Figure 3: Schematic view of an SMBH binary evolution. (Burke-Spolaor et al., 2019)

few weeks for a decade or more long term. The reciprocal of the cadence of these observations and the total observation period corresponds to the observable frequency of GWs, which is nHz - μHz range.
The following PTA groups are currently operating around the world:

- North American Nanohertz Observatory for Gravitational Waves (NANOGrav, McLaughlin (2013a))
- European PTA (EPTA, Kramer and Champion (2013b))
- Parkes PTA (PPTA, Hobbs (2013); Manchester et al. (2013))
- Indian PTA (InPTA, Joshi et al. (2018b, 2022))
- Chinese PTA (CPTA, Lee (2016b))
- MeerTime PTA (MPTA, Bailes et al. (2020); Spiewak et al. (2022))

In addition, the International PTA (IPTA), consisting of NANOGrav, EPTA, PPTA, and InPTA, has also been organized (Hobbs et al., 2010), and the teams are cooperating with each other to combine data in an attempt to detect nanohertz GWs.

1.3 the Indian PTA

InPTA is a PTA team established around 2015. inPTA monitors MSPs using the Giant Metrewave radio telescope (uGMRT, see Figure 5), which located in India and consists of 30 antennas with its diameter of 45 m. The uGMRT is capable of simultaneous multi-band observations. InPTA monitors MSP in two bands, Band 3 (300 - 500 MHz) and Band 5 (1260 - 1460 MHz). The low-frequency Band 3 observations are unique in the world, as no other PTA monitors MSPs with such a low-frequency band and can accurately measure the effects of dispersion delays on pulses. Dispersion delay is a phenomenon in which the group velocity of

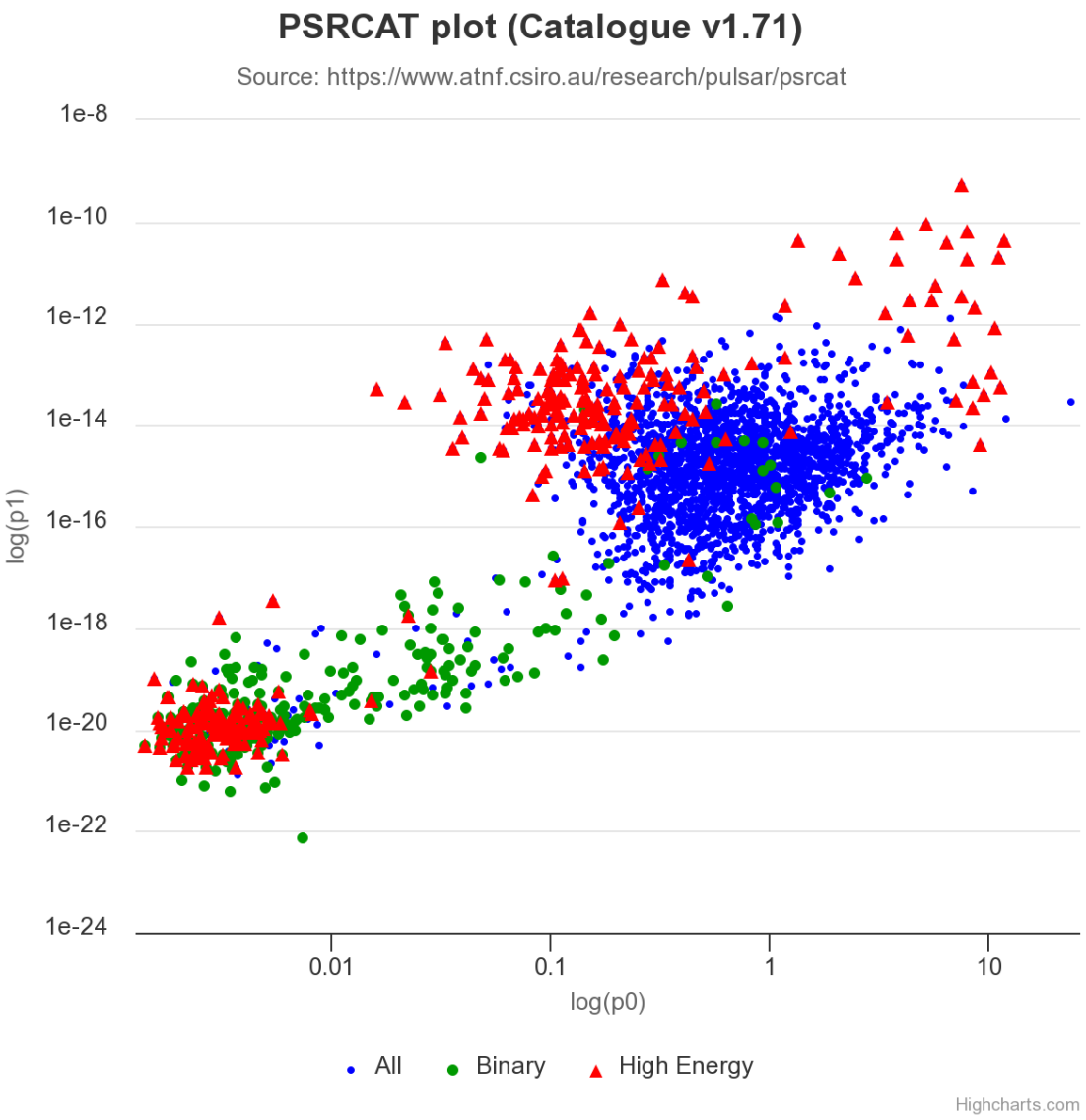

Figure 4: A scatter plot of pulse period and its derivative of known pulsars (Manchester et al., 2005). This plot is called the P-Pdot diagram.

Figure 5: The Giant Metrewave radio telescope. Credit:NCRA

electromagnetic waves propagating in interstellar plasma varies with frequency, and the delay is known to be proportional to inverse of the square of the radio frequency (see Figure 6).

$$\Delta t = 4.16(f_1^2 - f_2^2) \times \mathrm{DM} \tag{2}$$

where, f_1, f_2 are observing frequencies and DM is called Dispersion Measure. DM is written as follows:

$$\mathrm{DM} = \int_0^D n_e dl \tag{3}$$

where D is the distance from the earth to the pulsar, and n_e is electron density of the interstellar plasma. Since n_e is not given to a priori, the DM is determined by correcting the observed delay of lower frequency pulses. Indian PTA, with its low-frequency observations, is outstanding in this respect and can obtain DM with the highest accuracy. This is an indispensable element for high-precision pulsar timing observations. Indian PTA has released its first data release recording 3.5 years of 14 MSPs observation (Tarafdar et al., 2022). Along with the pulse arrival times, DM time series data for six pulsars were also released. This is expected to play a complementary role when combined with other PTA data, bringing us much closer to low-frequency GWs detection.

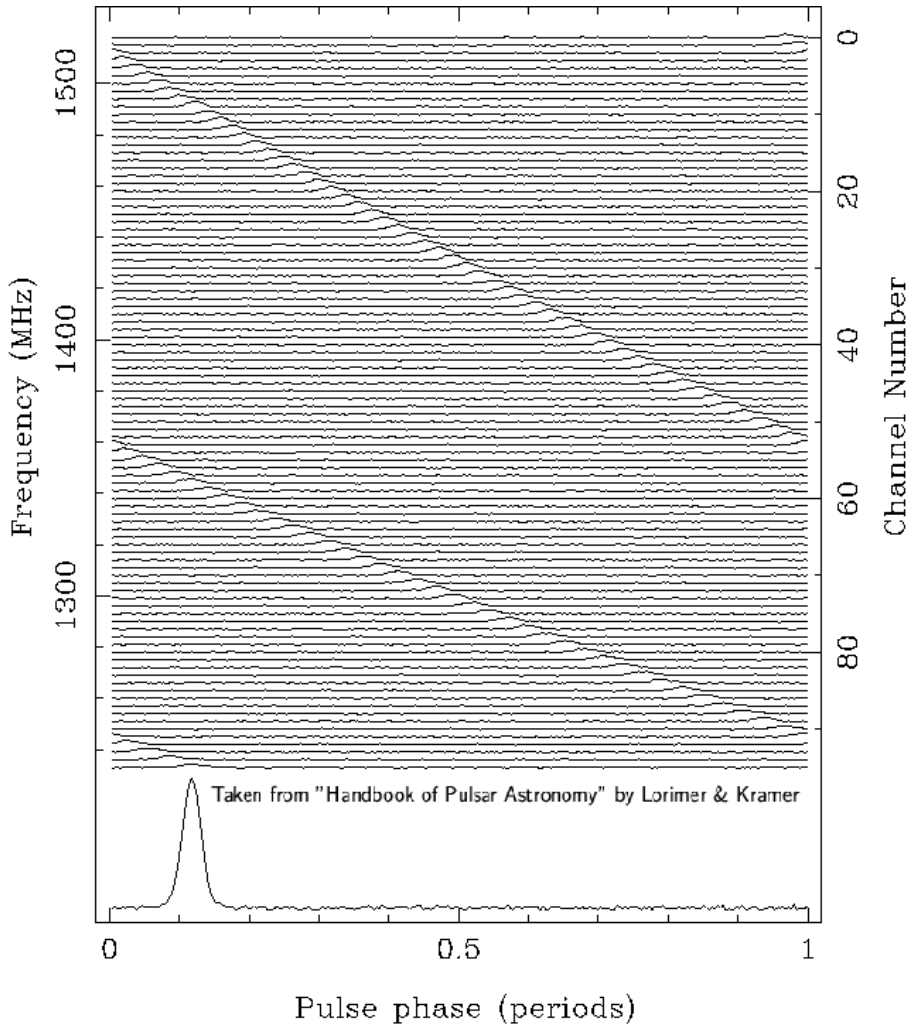

Figure 6: An example of dispersion delay (Lorimer and Kramer, 2004). The horizontal axis corresponds to time. The vertical axis is frequency. We can see lower frequency pulses arrive later compaired to higher frequency.

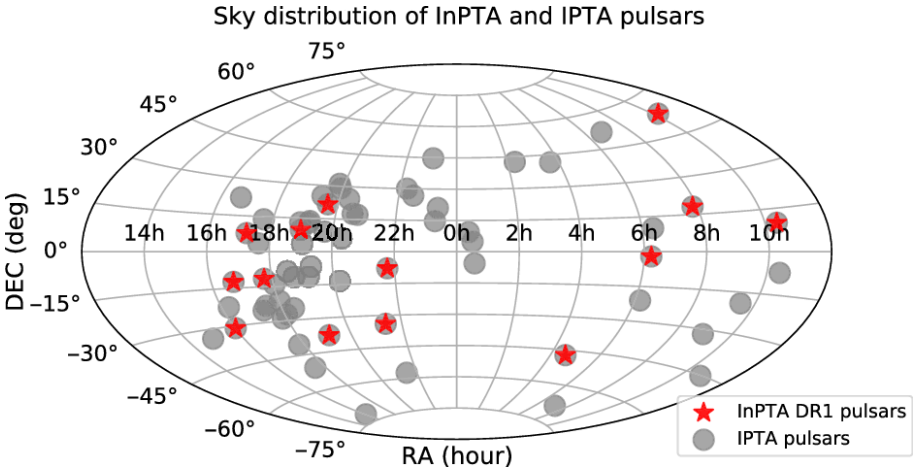

Figure 7: Location of InPTA pulsars (Tarafdar et al., 2022).

2 Constraints on ultra-low frequency GWs from an eccentric Supermassive blackhole binary

2.1 Introduction

Milli-second pulsars (MSPs) with very stable periods can be used as precise clocks. If gravitational waves (GWs) exist in the space between the earth and pulsars, the arrival time of pulses is changed. With this effect, we can detect low-frequency GWs (10^{-9} - 10^{-6} Hz) and this method is called pulsar timing array (PTA) (Foster and Backer, 1990b). So far, three PTA experiments have been conducting long-term observations of MSPs: the Parkes PTA in Australia (Manchester et al., 2013), the European PTA (Kramer and Champion, 2013a), and NANOGrav in North America (McLaughlin, 2013b). Further, Chinese PTA (Lee, 2016a) and Indian PTA (Joshi et al., 2018a) have started in recent years.

One of the major GW sources in the frequency range of PTA is supermassive black hole (SMBH) binaries in the late stage of the evolution with sub-pc scale orbital radii. NANOGrav have released 11 years of pulsar observation data (Arzoumanian et al., 2018) and searched GWs from an individual source (Aggarwal et al., 2019). Although they could not find GWs in their 11-year data set they placed 95% upper limits on GWs amplitude and a chirp mass of a hypothetical SMBH binary in the Virgo Cluster. Recently, they also put limits on mass of SMBH binary in nearby massive galaxies (Arzoumanian et al., 2021).

On the other hand, binaries in the early stage of the evolution interact efficiently with the environmental gas and stars and their orbital radii are reduced rapidly (Escala et al., 2005; Dotti et al., 2007; Sesana et al., 2008). However, when the orbital radius becomes a few pc, the interaction becomes weak and the orbital radius shrink only through GW emission. GW emission at this stage is not efficient and the expected merger time exceeds the Hubble time (Lodato et al., 2009; Milosavljević and Merritt, 2001). This is called "the final parsec problem". Therefore, to understand the evolution of SMBH binaries, it is important to detect GWs from binaries at this stage. However, such GWs have sub-nHz frequencies and are out of the sensitivity range of the conventional PTA method.

In our previous work (Yonemaru et al., 2016), we proposed a new detection method for these ultra-low-frequency GWs from a single source. The method utilizes the fact that the spin-down rate of MSPs is biased by ultra-low-frequency GWs and it was shown that the time derivative of GW amplitude is constrained from the statistics of spatial pattern of pulsar spin-down rates in the sky. Then we evaluated the sensitivity with Monte-Carlo simulations (Yonemaru et al., 2018; Hisano et al., 2019) and put constraints on GWs from the Galactic Center and M87 as $\dot{h} < 6.2 \times 10^{-18}\,\mathrm{sec}^{-1}$ and $\dot{h} < 8.1 \times 10^{-18}\,\mathrm{sec}^{-1}$, respectively, for $f_{\mathrm{GW}} = 1/(1000\,\mathrm{year})$ (Kumamoto et al., 2019), where h is the GW amplitude and the dot represents the time derivative.

On the other hand, in Moore et al. (2015), they extended the sensitivity curve of PTAs toward lower frequencies in a different way. They considered the Taylor expansion of GW waveform in low-frequency limit and proposed to extract the GW amplitude from the third and higher order terms, while terms below the second-order are absorbed by pulsar parameters. Then, signal-to-noise ratio of GWs in lower frequencies were calculated. As a result, the sensitivity curve of GWs was shown to be proportional to f^{-2} at lower frequencies.

A critical assumption in Moore et al. (2015) is that an SMBH binary has a circular orbit. Therefore, their method is not applicable to binaries with eccentric orbits because GWs from an eccentric binary include higher harmonics and, therefore, have a very different waveform compared to that of GWs from a circular binary (Peters and Mathews, 1963). In fact, it has been shown by numerical simulations that pc-scale SMBH binaries tend to obtain high eccentricity (typically $e = 0.9$ for mass ratio $q \sim 10^{-3}$) via interaction with their environment (Sesana, 2010). Thus, it is important to probe sub-nHz GWs from not only circular binaries but eccentric binaries. In this paper, we propose a method which is applicable to eccentric SMBH binaries extending the formalism of (Moore et al., 2015).

The structure of this paper is following. In section 2.2, we briefly review the Kepler problem and analytical solution of GWs from an eccentric binary. Then, upper limits on eccentric GWs amplitude are derived expanding the Moore et al. (2015)'s method in section 2.2.4. In section 2.3, we apply our formalism to several possible SMBH binaries in nearby galaxies and derive limits on binary parameters. Finally, our results are summarized in section 2.4. For the rest of this paper we set $c = G = 1$, unless otherwise specified.

2.2 Eccentric gravitational waveform

2.2.1 Eccentric SMBH binary

Let us consider an eccentric binary system consisting of masses m_1 and m_2 ($m_1 > m_2$), reiterating some of the notation and formalism of Yunes et al. (2009) and Taylor et al. (2016). Such a system is well-known as the Kepler problem. Considering a coordinate system with a total mass $M_{\rm tot}$ as the center of mass, the binary system can be described as

$$r = a(1 - e\cos u), \tag{4}$$

$$\omega(t - t_0) = l = u - e\sin u, \tag{5}$$

$$\Phi - \Phi_0 = 2\arctan\left[\left(\frac{1+e}{1-e}\right)^{1/2}\tan\frac{u}{2}\right], \tag{6}$$

$$\omega = 2\pi f = 2\pi\sqrt{\frac{M_{\rm tot}}{a^3}}, \tag{7}$$

where r is the distance from m_1 to m_2, a is the semi-major axis of the orbit, e is the orbital eccentricity, u is the eccentric anomaly, ω is the average angular frequency, $l = \omega t + l_0 = 2\pi f t + l_0$ is the mean anomaly, Φ is the orbital phase, and $\Phi_0 = \Phi(0)$. In order to express Φ as the function of time, we use the first Bessel function J_n and we have,

$$\cos\Phi = -e + \frac{2}{e}(1-e^2)\sum_{n=1}^{\infty} J_n(ne)\cos(nl), \tag{8}$$

$$\sin\Phi = (1-e^2)^{1/2}\sum_{n=1}^{\infty}[J_{n-1}(ne) - J_{n+1}(ne)]\sin(nl). \tag{9}$$

2.2.2 GW waveform

Imposing the transverse-traceless gauge (TT gauge), the GW tensor can be expressed as a superposition of two polarization modes and given by,

$$h_{ij}(t,\hat{\Omega}) = h_{+}(t)e^{+}_{ij}(\hat{\Omega}) + h_{\times}(t)e^{\times}_{ij}(\hat{\Omega}), \tag{10}$$

where $\hat{\Omega}$ is the direction of GW propagation, and $e^{+,\times}_{ij}$ are polarization tensors. If a SMBH binary has non-zero eccentricity, GWs emitted from it have higher harmonics components and the amplitude of two polarization modes is as follows (Peters and Mathews, 1963; Barack and Cutler, 2004):

$$\begin{aligned} h_{+}(t) =& h_0 \sum_n -\left(1+\cos^2\iota\right)\left[a_n(t)\cos(2\gamma) - b_n(t)\sin(2\gamma)\right] \\ &+ \left(1-\cos^2\iota\right)c_n(t), \end{aligned} \tag{11}$$

$$h_{\times}(t) = h_0 \sum_n 2\cos\iota\left[b_n(t)\cos(2\gamma) + a_n(t)\sin(2\gamma)\right], \tag{12}$$

where

$$h_0 = \frac{2m_1m_2}{Da}, \tag{13}$$

$$a_n(t) = x_{a_n}(e)\cos[nl(t)], \tag{14}$$

$$b_n(t) = x_{b_n}(e)\sin[nl(t)], \tag{15}$$

$$c_n(t) = x_{c_n}(e)\cos[nl(t)], \tag{16}$$

$$\begin{aligned} x_{a_n}(e) =& -\frac{n}{2}\Big[J_{n-2}(ne) - 2eJ_{n-1}(ne) + \frac{2}{n}J_n(ne) \\ &+ 2eJ_{n+1}(ne) - J_{n+2}(ne)\Big], \end{aligned} \tag{17}$$

$$x_{b_n}(e) = -\frac{n}{2}\sqrt{1-e^2}\left[J_{n-2}(ne) - 2J_n(ne) + J_{n+2}(ne)\right], \tag{18}$$

$$x_{c_n}(e) = J_n(ne). \tag{19}$$

Here, m_1 and m_2 are the mass of the main SMBH and second BH, respectively, D is the distance from the Earth to the source, ι is the orbital inclination, and γ is the azimuthal angle measuring the direction of pericenter. In the case of a circular binary, i.e. $e = 0$, only $n = 2$ terms remain in Eqs. (14) to (19). In this expression, $h_{+,\times}$ depends on time through the trigonometric functions. Then, we combine them into a cosine

function:

$$h_M(t) = h_0 \sum_n \sqrt{A_{M,n}^2 + B_{M,n}^2} \cos\left(nl(t) + \alpha_{M,n}\right), \tag{20}$$

$$A_{+,n} = \left(1 + \cos^2\iota\right) x_{b_n} \sin(2\gamma), \tag{21}$$

$$B_{+,n} = \left(1 - \cos^2\iota\right) x_{c_n} - \left(1 + \cos^2\iota\right) x_{a_n} \cos(2\gamma), \tag{22}$$

$$A_{\times,n} = 2x_{b_n} \cos\iota \cos 2\gamma, \tag{23}$$

$$B_{\times,n} = 2x_{a_n} \cos\iota \sin 2\gamma, \tag{24}$$

$$\alpha_{M,n} = \tan^{-1}\left(-\frac{A_{M,n}}{B_{M,n}}\right), \tag{25}$$

where M represents two polarization mode $(+, \times)$.

2.2.3 Pulsar Timing Residuals

If GWs pass between the Earth and pulsars, the propagation path of pulses is changed, and the arrival time of pulses is also changed. The difference between the actual and predicted arrival time of pulses is called a timing residual. The timing residual induced by GWs for a-th pulsar is written by

$$R_a(t, \hat{\Omega}) = \int_0^t dt\, z_a(t, \hat{\Omega}), \tag{26}$$

where $z_a(t, \hat{\Omega})$ is the rate of change in the arrival time of pulses. Using the direction of unit vector $\hat{p}_a = (\sin\theta_a \cos\phi_a, \sin\theta_a \sin\phi_a, \cos\theta_a)$, z_a can be written as follows:

$$z_a(t, \hat{\Omega}) = \frac{1}{2} \frac{\hat{p}_a^i \hat{p}_a^j}{1 + \hat{p}_a \cdot \hat{\Omega}} \left(h_{ij}(t, \hat{\Omega}) - h_{ij}(t_p, \hat{\Omega})\right), \tag{27}$$

where $t_p = t - L_a\left(1 + \hat{p}_a \cdot \hat{\Omega}\right)$ is time when the GW passes the a-th pulsar and L_a is the distance from it to the Earth. In Eq. (27) the first and second terms are called "the Earth term" and "the pulsar term", respectively. As the puslar term behaves as $\propto \cos(2\pi f_{\rm gw} L)$, the effect depends on the GW frequency. When the GW wavelength is much shorter than the typical pulsar distance ($\sim$ kpc), i.e, GW frequency is much larger than 10^{-13} Hz, the pulsar term contributes as random noise with zero mean (see Fig. 8 in Hisano et al. (2019)). Thus, the pulsar term can be ignored as noise which averages to zero when calculating correlations between pulsar residuals as is also assumed in Moore et al. (2015). In this work, we consider a situation where the GW frequency is $\gtrsim 10^{-11}$ Hz and, therefore, we consider only the Earth term in the following section.
Using the antenna beam pattern $F_a^M(\hat{\Omega})$ given by Anholm et al. (2009), Eq. (26) is written as follows:

$$R_a(t, \hat{\Omega}) = \sum_{M=+,\times} F_a^M \int_0^t dt h_M(t), \tag{28}$$

$$F_a^M(\hat{\Omega}) = \frac{1}{2} \frac{\hat{p}_a^i \hat{p}_a^j}{1 + \hat{p}_a \cdot \hat{\Omega}} e_{ij}^M(\hat{\Omega}). \tag{29}$$

To proceed the calculation analytically, following Moore et al. (2015), we assume pulsar distribution as uniform in the sky, and average Eq. (28) with the direction of pulsars. Eq. (28) depends on the direction of pulsars only through $F_a^M(\hat{\Omega})$. However, because $F_a^M(\hat{\Omega})$ itself becomes zero when averaged with respect to the direction of pulsars, we use the root-mean-square of $F_a^M(\hat{\Omega})$. Furthermore, the dependence of polarization vanishes by this procedure. Then we can calculate the GW amplitude with either polarization. Therefore the averaged timing residual can be written as

$$R_M(t) = \bar{F} \int_0^t dt\ h_M(t), \tag{30}$$

$$\bar{F} = \int d\hat{p}_a^3 \sqrt{(F_a^M)^2} \tag{31}$$

where $\hat{F}$ is the root mean square of $F_a^M(\hat{\Omega})$. Substituting Eq. (20), we obtain

$$R_M(t) = \bar{F} h_0 \sum_n \frac{1}{2\pi n f} \sqrt{A_{M,n}^2 + B_{M,n}^2} \sin(2\pi n f t + n l_0 + \alpha_{M,n}) \tag{32}$$

As we explained above, the assumption of uniform distribution of pulsars is necessary for analytic evaluation. In fact, as can be seen in Arzoumanian et al. (2018), the observed distribution is highly concentrated on the Galactic plane and we need numerical calculations for more quantitative evaluation, which is beyond the scope of our paper.

2.2.4 Upper limits on ultra-low-frequency GWs from eccentric binary

In this section, we develop a formalism to derive upper limits on ultra-low-frequency GWs from an eccentric SMBH binary. The signal-to-noise ratio of PTA satisfies the following equation (see Moore et al. (2015)):

$$\rho^2 = \sum_b \sum_{a>b} \frac{8}{T} \int df \frac{|R_a(f)|^2 |R_b(f)|^2}{S_{n,a}^2}, \tag{33}$$

$$S_{n,a} = \delta t_a \sigma_a^2, \tag{34}$$

where T and $1/\delta t_a$ are the observing time span and cadence, respectively, and σ_a is the root mean square in the timing residuals for the a-th pulsar. Here, we consider sky averaged timing residuals and Eq. (33) is written as

$$\rho^2 = \sum_{M=+,\times} \frac{1}{2} N_p (N_p - 1) \frac{8}{T} \int df \frac{|R_M(f)|^4}{\delta t^2 \sigma^4}, \tag{35}$$

where N_p is the number of pulsars in PTAs. Considering Parseval's theorem to change the frequency integral to a time integral, Eq. (35) can be written approximately as

$$\rho^2 \approx \sum_{M=+,\times} \frac{1}{2} N_p (N_p - 1) T \int_0^T dt \frac{|R_M(t)|^4}{\delta t^2 \sigma^4}. \tag{36}$$

Substituting Eq. (32), we obtain

$$\rho^2 = \frac{N_p(N_p-1)T\bar{F}^4 h_0^4}{2\delta t^2 \sigma^4} \sum_{M=+,\times} \int_0^T dt \times \left(\sum_n \frac{1}{nf} \sqrt{A_{M,n}^2 + B_{M,n}^2} \sin(2\pi n f t + n l_0 + \alpha_{M,n}) \right)^4 . \tag{37}$$

In the high frequency limit ($ft \gg 1$), right hand side can be approximated as $h_0^4(\eta_+ + \eta_\times)/f^4$, where η is the factor which depend on orbital elements (see Appendix 2.4). Therefore, upper limits in the high frequency limits behave as

$$h_{\rm lim}^{\rm HIGH} \propto f(\eta_+ + \eta_\times)^{-1/4}. \tag{38}$$

On the other hand, in the low-frequency limit ($ft \ll 1$), the sine function is expanded as a power series

$$\sin(2\pi n f t + \phi_n) = \sin\phi_n + (2\pi n f t)\cos\phi_n - \frac{(2\pi n f t)^2}{2!}\sin\phi_n - \frac{(2\pi n f t)^3}{3!}\cos\phi_n + O(f^4 t^4). \tag{39}$$

The first term in this expansion degenerate with the distance to the pulsar. The second and third terms degenerate with the pulse period and spin-down rate respectively. Therefore, these terms are absorbed when parameter fitting of the pulsar model is carried out. Consequently, upper limits in the low-frequency limits is obtained from the fourth term and behave as,

$$h_{\rm lim}^{\rm LOW} \propto f^{-2}(\xi_+ + \xi_\times)^{-1}, \tag{40}$$

$$\xi_M = \left| \sum_n n^2 \sqrt{A_{M,n}^2 + B_{M,n}^2} \cos(n l_0 + \alpha_{M,n}) \right| . \tag{41}$$

Coefficients on the right hand side of Eqs. (38) and (40) can be given by current PTAs observation. The most recent limits on GWs from individual SMBH binary comes from NANOGrav (Aggarwal et al., 2019), which placed 95% upper limits with $f_{\rm gw} = 8\,{\rm nHz}$ as a function of sky position from an analysis of their 11-year data set (see Figure 5 in their paper). Then we can set upper limits on the GW from eccentric SMBH binary at higher and lower frequencies as follows:

$$h_{\rm lim} = h_{\rm lim}^{\rm NANOGrav}\left(f_{\rm gw} = 8\,{\rm nHz}, \hat{\Omega}\right) \times \left[\left(\frac{8\,{\rm nHz}}{2f} \right)^2 (\xi_+ + \xi_\times)^{-1} + \left(\frac{2f}{8\,{\rm nHz}} \right) (\eta_+ + \eta_\times)^{-1} \right] \tag{42}$$

Note that $f_{\rm gw}$ is the frequency of GWs from a circular binary and corresponding to $n = 2$. Therefore we choose $2f$ as the normalized frequency in Eq. (42). The right-hand side of Eq. (42) is determined by giving orbital parameters of the assumed SMBH binary $(m_1, m_2, a, e, l_0, \iota, \gamma)$. Finally, we obtain constraints on these parameters by comparing $h_{\rm lim}$ and h_0.

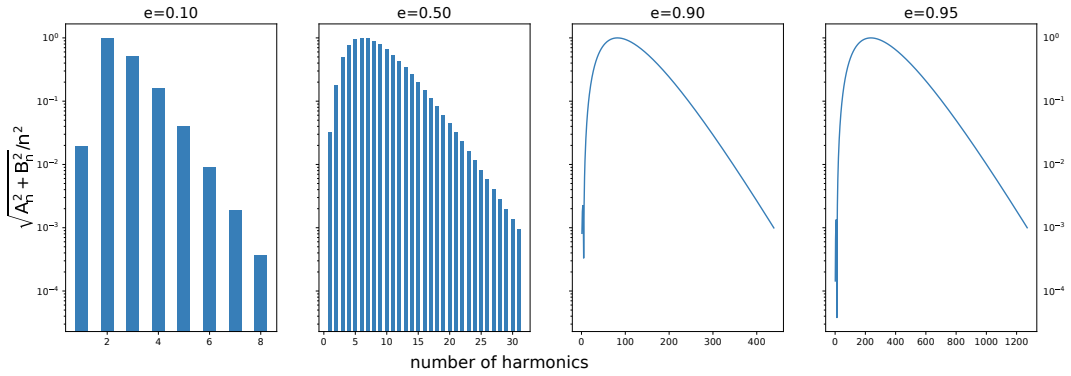

Figure 8: The contribution of higher harmonic components to ξ_+ normalized by the most contributing harmonic component for $(l_0, \iota, \gamma) = (0^\circ, 0^\circ, 0^\circ)$.

Finally, it should be noted that the NANOGrav limits were obtained with Bayesian analysis, while our approach is based on frequentist analysis. However, using the Baysian limits rather than frequentist limits, which are not given in NANOGrav paper, is reasonable for our purpose because Baysian and frequentist limits are expected to be the same order.

2.3 Application

In this section, we apply our formalism to several nearby SMBH binary candidates. In the numerical evaluation of upper limits, it is necessary to terminate the calculation of the sum of η and ξ with the required accuracy. In our work, we terminate the calculation when the following conditions are satisfied:

$$\frac{\frac{1}{i}\sqrt{A_{M,i}^2 + B_{M,i}^2}}{\max_n\left(\frac{1}{n}\sqrt{A_{M,n}^2 + B_{M,n}^2}\right)} < 10^{-3} \quad (\text{for } \eta), \tag{43}$$

$$\frac{i^2\sqrt{A_{M,i}^2 + B_{M,i}^2}}{\max_n\left(n^2\sqrt{A_{M,n}^2 + B_{M,n}^2}\right)} < 10^{-3} \quad (\text{for } \xi). \tag{44}$$

In Fig. 8, we show the contribution of higher harmonic components to ξ_+ for several values of eccentricity. In this figure, other binary parameters are set as $(l_0, \iota, \gamma) = (0^\circ, 0^\circ, 0^\circ)$. We can see that the contribution of higher harmonics is larger for a larger value of eccentricity. For example, $n \sim 300$ modes are contributing the most for the case of $e = 0.95$. In this case, we need to conduct the summation of Eq. (41) up to $n = 1270$, while the summation up to $n = 8$ is sufficient for $e = 0.1$. We note that the number of harmonics is much smaller in timing residual space (Taylor et al., 2016).

First, let us show limits on a possible SMBH binary located at the center of M87 suggested by (Lena et al., 2014). The mass of the SMBH in the center of M87 is estimated to be $6.5 \times 10^9 M_\odot$ and the distance from earth is 16.8 Mpc (Event Horizon Telescope Collaboration et al., 2019). The value of NANOGrav's limit in

the direction of M87 is approximately given as

$$h^{\rm NANOGrav}_{\rm lim,M87}\left(f_{\rm gw}=8\,{\rm nHz},\hat{\Omega}_{\rm M87}\right)\approx 3.66\times10^{-15}. \tag{45}$$

Figure. 9 represents the rejected parameter space of a possible eccentric SMBH binary in the center of M87 for $e=0.9$. Solid, dashed, dot-dashed, dot lines represent the boundary of $h_0=h_{\rm lim}$ for $l_0=0^\circ,60^\circ,120^\circ,180^\circ$, respectively. The value of h_0 is greater than $h_{\rm lim}$ in the region below each curve and, therefore, the corresponding parameter sets are rejected. The limit becomes stronger as l_0 decreases. This is because small l_0 corresponds to a binary which starts near the pericenter and consequently the GW amplitude becomes stronger. The constraint curves do not vary significantly with the value of (ι,γ), although a smaller inclination angle leads to slightly stronger constraint. These parameters affect the relative power of two polarizations $(+,\times)$, but do not the total energy of emitted GWs. Thus, hereafter, we fix (ι,γ) to $(0,0)$.

In the case of $l_0=0^\circ$, the mass ratio is strongly constrained especially for $a\lesssim 0.3$ pc: typically $m_2/m_1\lesssim 3\times10^{-3}$. On the other hand, the lower limit on the semi-major axis is a function of the mass ratio for $m_2/m_1\gtrsim 3\times10^{-3}$ and roughly given as $a\gtrsim 2(m_2/m_1)^{0.3}$ pc. The constraints on the semi-major axis is weaker by about one order in the case of $l_0=60^\circ$ and even slightly weaker for $l_0=120^\circ$ and 180°.

Next, in Fig. 10, we show the rejected parameter space for different values of eccentricity fixing $(\iota,\gamma)=(0,0)$. The constraints drastically change with eccentricity in the case with $l_0=0^\circ$, while the change is not significant for other values of l_0. This is because the binary separation changes relatively rapidly for $l_0=0^\circ$ (pericenter). In fact, in the case with $l_0=0^\circ$, the constraints on semi-major axis at $m_2/m_1=0.1$ improve by a factor of 5 and 2 for the change of eccentricity from 0.5 to 0.9 and from 0.9 to 0.95, respectively.

Here it should be noted that the change of the constraint curve is not monotonic with the change of eccentricity for $l_0=180^\circ$ (apocenter). This is because there are two competing factors that affect the GW amplitude from a binary at apocenter. The first is that higher eccentricity leads to a larger separation between two SMBHs, which weakens the GW amplitude. The second is that the shape of the binary orbit near the apocenter becomes sharper for large eccentricity, which enhances the GW amplitude. Therefore, we consider that the former effect is more effective than the latter for $e=0.5$ and, conversely the latter effect becomes relatively more effective for $e=0.1$ and $e=0.9$.

For a high eccentricity binary at pericenter $l_0=0^\circ$, we can see a turnover in the curve as a function of a. This turnover can be interpreted as follows. From Eqs. (7), (13) and (42) in low-frequency cases ($2f\ll 8\,{\rm nHz}$), i.e. $a\gtrsim 1\,{\rm pc}$, $h_0/h_{\rm lim}$ behave as

$$\frac{h_0}{h_{\rm lim}}\propto\frac{m_2 f^2}{a}\propto\frac{(q+1)q}{a^4}, \tag{46}$$

where $q=m_2/m_1$ is mass ratio. Because limit curves correspond to $h_0/h_{\rm lim}=1$, the relation between a and q is as follows:

$$\log(1+q)+\log q-4\log a+C=0, \tag{47}$$

where C is the coefficient of the right hand side in Eq. (46). For large and smalls values of q, the relation is

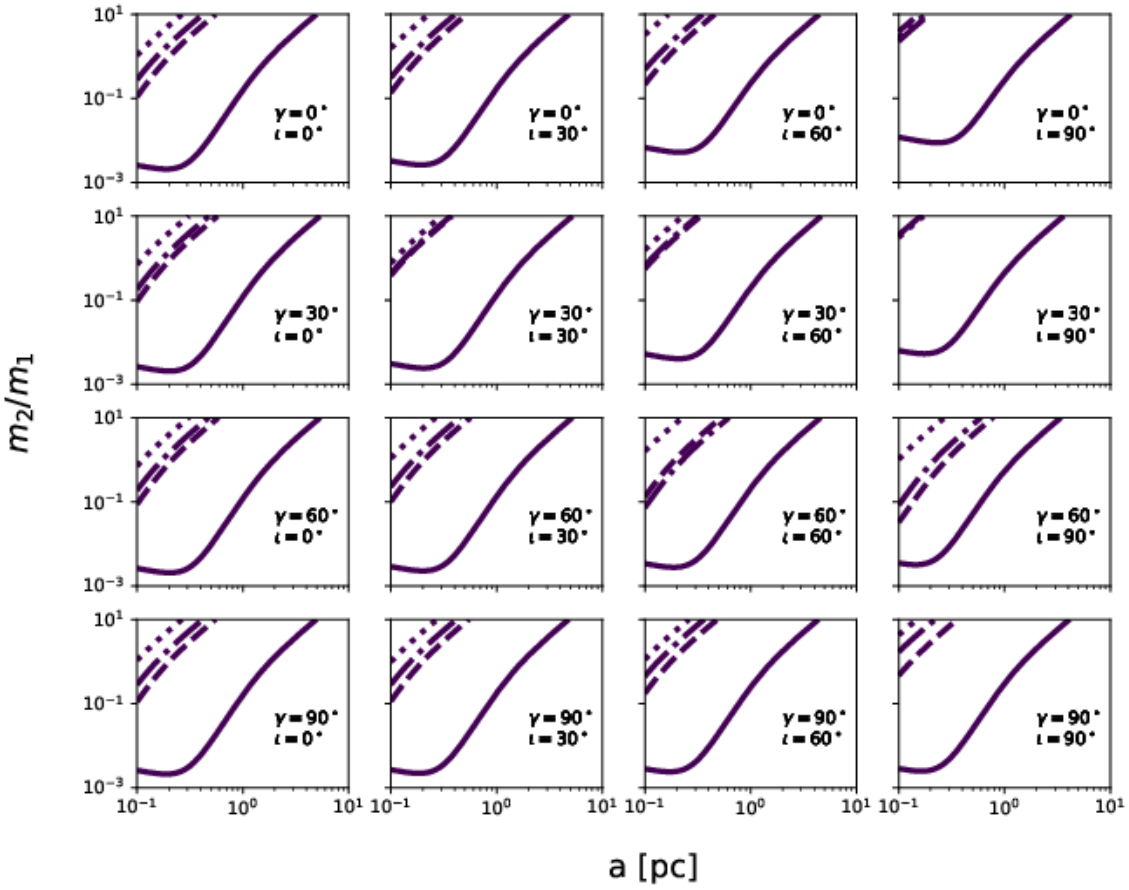

Figure 9: The rejected parameter space of an eccentric SMBH binary in the center of M87 for $e = 0.9$. Solid, dashed, dot-dashed, dot lines means points of $h_0 = h_{\rm lim}$ for $l_0 = 0°, 60°, 120°, 180°$, respectively. Regions above each curve is rejected.

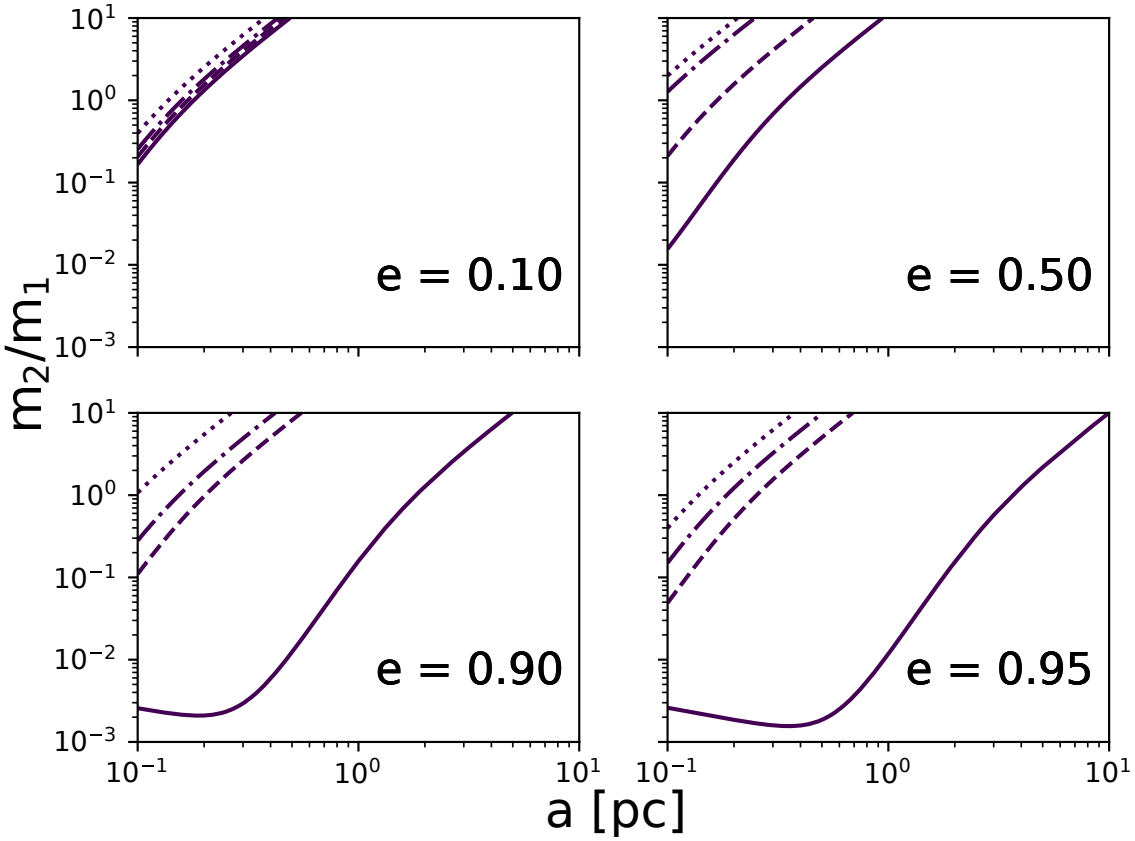

Figure 10: The rejected parameter space for $e = 0.1, 0.5, 0.9$ and 0.95 fixing $(\iota, \gamma) = (0, 0)$. The line types are the same as Fig. 9.

Table 1: The SMBH mass, the distance from earth and NANOGrav's 95% upper limtis of five galaxies considered here (Arzoumanian et al., 2021).

2MASS Name	Mass $[\log(m_1/M_\odot)]$	Dist [Mpc]	$h_{\rm lim}^{\rm NANOGrav}$
J13000809+2758372	10.32	112.2	3.17×10^{-15}
J12304942+1223279	9.82	16.8	3.66×10^{-15}
J04313985-0505099	10.23	63.8	1.04×10^{-14}
J12434000+1133093	9.67	18.6	3.77×10^{-15}
J13182362-3527311	9.89	53.4	2.94×10^{-15}

Table 2: The mass-ratio upper limits as a function of l_0 with $a = 1\,$pc and $e = 0.5$.

2MASS Name	Mass ratio m_2/m_1			
	$l_0 = 0^\circ$	$l_0 = 60^\circ$	$l_0 = 120^\circ$	$l_0 = 180^\circ$
J13000809+2758372	4.79	22.9	75.9	110
J12304942+1223279	12.0	52.5	174	251
J04313985-0505099	9.12	39.8	145	209
J12434000+1133093	20.9	91.2	331	479
J13182363-3527311	14.5	63.1	229	331

simplified to,

$$\log q = \begin{cases} 2\log a - C/2 & (q \gg 1) \\ 4\log a - C & (q \ll 1). \end{cases} \tag{48}$$

For this reason, the slope of the curves slightly vary in $q \sim 1$. On the other hand, in high frequency cases ($2f \gg 8\,$nHz), i.e. $a \lesssim 0.1\,$pc, we have,

$$\frac{h_0}{h_{\rm lim}} \propto \frac{m_2}{af} \propto \sqrt{\frac{qa}{1+q}}. \tag{49}$$

For $q \ll 1$, the relation reduces to,

$$\log q = -\log a - 2C'. \tag{50}$$

Considering Eqs. (48) and (50), we can understand that there is a turnover at $a \sim 0.3$ pc.

We also apply our formalism to other galaxies. In Arzoumanian et al. (2021), NANOGrav applied their 95% upper limits on GW amplitudes from single sources in galaxies listed in 2MASS Redshift Survey (Huchra et al., 2012). They calculated signal-to-noise ratio of GWs from these galaxies assuming they have an equal-mass SMBH binary in the center. These galaxies were sorted in descending order with respect to signal-to-noise ratio. We derive constraints for five galaxies with largest signal-to-noise ratios. Table 1 is a list of five galaxies considered here: the SMBH mass, the distance from earth and NANOGrav's 95% upper limtis $h_{\rm lim}^{\rm NANOGrav}(f_{\rm gw} = 8\,{\rm nHz})$. In Table 2 to 4, we list upper limits on mass ratio of hypothetical SMBH binaries in these galaxies for $e = 0.5$, 0.9 and 0.95, and $l_0 = 0^\circ$, 60°, 120° and 180°, fixing $a = 1$ pc.

Table 3: The mass-ratio upper limits as a function of l_0 with $a = 1\,\mathrm{pc}$ and $e = 0.9$.

2MASS Name	Mass ratio m_2/m_1			
	$l_0 = 0^\circ$	$l_0 = 60^\circ$	$l_0 = 120^\circ$	$l_0 = 180^\circ$
J13000809+2758372	0.033	14.5	25.1	63.1
J12304942+1223279	0.158	36.3	63.1	158
J04313985-0505099	0.110	27.5	47.9	120
J12434000+1133093	0.437	63.1	110	275
J13182363-3527311	0.251	43.7	75.9	191

Table 4: The mass-ratio upper limits as a function of l_0 with $a = 1\,\mathrm{pc}$ and $e = 0.95$.

2MASS Name	Mass ratio m_2/m_1			
	$l_0 = 0^\circ$	$l_0 = 60^\circ$	$l_0 = 120^\circ$	$l_0 = 180^\circ$
J13000809+2758372	0.00302	9.12	17.4	33.1
J12304942+1223279	0.0120	22.9	43.7	75.9
J04313985-0505099	0.0100	17.3	33.1	63.1
J12434000+1133093	0.0363	39.8	75.9	145
J13182363-3527311	0.0191	27.5	52.5	100

2.4 Summary and discussion

In this paper, we developed a formalism for constraining ultra-low frequency GWs from a SMBH binary with eccentric orbit. Following Moore et al. (2015), we calculated signal-to-noise ratio of GWs by Taylor expanding the waveform and using the third-order term that is not absorbed by fitting pulsar parameters. Furthermore, using upper limits on GWs from single sources at 8 nHz obtained by NANOGrav's 11-year data set, we derived constraints on binary parameters of a hypothetical SMBH binary in the center of M87. We found that the constraints depend strongly on the orbital eccentricity and initial phase while they do not depend significantly on the inclination and the azimuthal angle of pericenter. The obtained upper limits on mass ratio are typically $(m_2/m_1) < 0.16$ for $e = 0.9$, $a = 1\,\mathrm{pc}$ for pericenter ($l_0 = 0^\circ$). We also applied our formalism to several other SMBHs in nearby massive galaxies probed by NANOGrav.

In our calculation, we assumed a uniform distribution of MSPs in the sky. In fact, MSPs used in PTA experiments have a non-uniform distribution and many of them are located within the Galactic plane. Although the anisotropy of MSP distribution will not change the frequency dependence of GW constraints, it will affect the normalization. As we can see in Aggarwal et al. (2019), the NANOGrav limit is actually stronger for a region around the Galactic Center where many MSPs are located, while it is weaker at anti-Galactic Center region. Thus, GW constraints obtained here become stronger (weaker) for a sky region with more (less) MSPs accordingly. Quantitative discussion with numerical integration of the factor in Eq. (29) is beyond the scope of the current paper and will be presented elsewhere. Nevertheless, because the NANOGrav's upper limits, which we used for normalization, are obtained considering the pulsar non-uniformity, our approach would give a reasonable estimate.

We also assumed the binary orbit does not change in the observing time span, which is typically ~ 10 years, because we mainly consider the ultra-low frequency range. However, when a binary orbit is close

to coalescence, we cannot neglect the orbital evolution. The orbital evolution caused by GWs is given by Eq. (5.6) and (5.7) in Peters (1964) and we can estimate the order of the orbital evolution averaged over the orbital period. For the initial eccentricity $e_0 = 0.95$, taking typical parameters, the orbital evolution is as follows:

$$\left.\frac{1}{a}\frac{da}{dt}\right|_{t=t_0} \times 10\,\mathrm{years} = -6.7\times10^{-5} \times\left(\frac{a}{0.1\,\mathrm{pc}}\right)^{-4}\left(\frac{q(1+q)}{0.11}\right)\left(\frac{m_1}{10^9 M_\odot}\right)^{3}\left(\frac{1-e^2}{1-0.95^2}\right)^{-7/2} \tag{51}$$

$$\left.\frac{1}{e}\frac{de}{dt}\right|_{t=t_0} \times 10\,\mathrm{years} = -3.4\times10^{-6} \times\left(\frac{a}{0.1\,\mathrm{pc}}\right)^{-4}\left(\frac{q(1+q)}{0.11}\right)\left(\frac{m_1}{10^9 M_\odot}\right)^{3}\left(\frac{1-e^2}{1-0.95^2}\right)^{-5/2} \tag{52}$$

Thus, for M87 with $a = 0.1\,\mathrm{pc}$, $q = 0.1$ and $e = 0.95$, the amount of orbital evolution is $\sim 2\%$ and $\sim 0.1\%$, respectively, and the effect of orbital evolution can be neglected. However, if the semimajor axis is as small as $a = 0.05\,\mathrm{pc}$, the orbital evolution reaches $\sim 30\%$ and $\sim 1.6\%$, respectively. For such an orbit where the semimajor axis changes rapidly, the GW waveform and frequency also change and our formalism may not be valid.

Appendix

High Frequency Integral

In Moore et al. (2015), the integration of the $\sin^4$ term at high frequencies ($ft \gg 1$) is

$$\int_0^T dt \sin^4(2\pi f t + \phi) = \frac{3}{8}T - \frac{1}{4}\sin(2T + 2\phi) + \frac{1}{32}\sin(4T + 4\phi). \tag{53}$$

The first term of the right hand side is $O(T)$ and the second and third terms are $O(1)$. Then the second and third term could be neglected. In our work, we need to calculate the integral of Eq. (37):

$$\begin{aligned}&\int_0^T dt \left(\sum_n \frac{1}{n}\sqrt{A_{M,n}^2 + B_{M,n}^2}\sin(2\pi n f t + n l_0 + \alpha_{M,n})\right)^4 \\ &= \sum_{i,j,k,l} A_{M,ijkl}\int_0^T \sin(2\pi i f t + \phi_{M,i})\sin(2\pi j f t + \phi_{M,j})\sin(2\pi k f t + \phi_{M,k})\sin(2\pi l f t + \phi_{M,l})\,dt,\end{aligned} \tag{54}$$

where $A_{M,ijkl}$ is a unified term of coefficients of each sin and $\phi_{M,n} = n l_0 + \alpha_{M,n}$. Using formula of trigonometric function, we transform the integrand:

$$\begin{aligned}&\sin(2\pi i f t + \phi_{M,i})\sin(2\pi j f t + \phi_{M,j})\sin(2\pi k f t + \phi_{M,k})\sin(2\pi l f t + \phi_{M,l}) \\ &= \frac{1}{4}\left[\cos\{2\pi(i-j)ft + \phi_{M,i} - \phi_{M,j}\} - \cos\{2\pi(i+j)ft + \phi_{M,i} + \phi_{M,j}\}\right] \\ &\times\left[\cos\{2\pi(k-l)ft + \phi_{M,k} - \phi_{M,l}\} - \cos\{2\pi(k+l)ft + \phi_{M,k} + \phi_{M,l}\}\right]\end{aligned} \tag{55}$$

By expanding the right hand side, we obtain four cos × cos terms. One of them can be transformed as follows:

$$\begin{aligned}&\cos\{2\pi(i-j)ft+\phi_{M,i}-\phi_{M,j}\}\cos\{2\pi(k-l)ft+\phi_{M,k}-\phi_{M,l}\}\\&=\frac{1}{2}\left[\cos\{2\pi(i-j+k-l)ft+\phi_{M,i}-\phi_{M,j}+\phi_{M,k}-\phi_{M,l}\}+\cos\{2\pi(i-j-k+l)ft+\phi_{M,i}-\phi_{M,j}-\phi_{M,k}+\phi_{M,l}\}\right].\end{aligned} \tag{56}$$

If $i-j+k-l=0$, the time dependence of the first term of the right hand side is vanished. Then, this term contributes to the signal-to-noise ratio at $O(T)$ as a consequence of time integration. On the other hand, if $i-j+k-l\neq 0$, the time dependence of this term remains and this term behave $O(1)$ after time integration. Therefore, among the terms expressed by expanding the Eq. (55) and transforming it like Eq. (56), only the terms whose the time dependence is vanished for a certain combination of (i,j,k,l) has a non-negligible value after the time integration. The conditions of (i,j,k,l) are the following equations:

$$i-j+k+l=0, \tag{57}$$
$$i-j-k+l=0, \tag{58}$$
$$i-j-k-l=0, \tag{59}$$
$$i-j+k-l=0, \tag{60}$$
$$i+j+k-l=0, \tag{61}$$
$$i+j-k-l=0, \tag{62}$$
$$i+j-k+l=0. \tag{63}$$

Writing these conditions with $f_m(i,j,k,l)=0\,(m=1,\cdots,7)$ from the top to the bottom, sets of (i,j,k,l) satisfying $f_m=0$ can be written as follows:

$$\Lambda_m=\{(i,j,k,l)\in\mathbb{N}_+^4\,|\,f_m(i,j,k,l)=0\}, \tag{64}$$

where $\mathbb{N}_+$ is the set of positive integer. We write the sum of $\phi_{M,i},\phi_{M,j},\phi_{M,k},\phi_{M,l}$ added with the sign same as (i,j,k,l) appered in f_m (for example, $\Phi^1_{M,ijkl}=\phi_{M,i}-\phi_{M,j}+\phi_{M,k}+\phi_{M,l}$). Then the integration of Eq. (37) approximate as:

$$\int_0^T dt\left(\sum_n\frac{1}{n}\sqrt{A_{M,n}^2+B_{M,n}^2}\sin(2\pi nft+nl_0+\alpha_{M,n})\right)^4\approx\frac{T}{8}\sum_{m=1}^{7}\sum_{(i,j,k,l)\in\Lambda_m}(-1)^m A_{M,ijkl}\cos\Phi^m_{M,ijkl}. \tag{65}$$

Therefore, we obtain upper limits in Eq. (42) defining η_M as follows:

$$\eta_M=\sum_{m=1}^{7}\sum_{(i,j,k,l)\in\Lambda_m}(-1)^m A_{M,ijkl}\cos\Phi^m_{M,ijkl}. \tag{66}$$

In this work, the contribution of η_M in Eq (42) is small because we consider ultra-low frequency GWs ($\leq$ nHz).

3 Low-frequency Pulse-Jitter measurement with the uGMRT I.: PSR J0437−4715

3.1 Introduction

Pulsars are rapidly rotating neutron stars that emit beamed emission, which is observed as a pulsed signal. Among the different types of pulsars, millisecond pulsars (MSPs) have the most stable periods, making them the most precise clocks in the universe. The precise timing of MSPs has been used to search for nanohertz gravitational waves (GWs) by multiple consortia, known as Pulsar Timing Arrays (PTAs) (Foster and Backer, 1990a), such as the North American Nanohertz Observatory for Gravitational Waves (McLaughlin, 2013a, NANOGrav), the European Pulsar Timing Array (Kramer and Champion, 2013b, EPTA), the Parkes Pulsar Timing Array (Hobbs, 2013; Manchester et al., 2013, PPTA), the Indian Pulsar Timing Array (Joshi et al., 2018b, 2022, InPTA), the Chinese Pulsar Timing Array (Lee, 2016b, CPTA) and the MeerTime Pulsar Timing Array (Bailes et al., 2020; Spiewak et al., 2022, MPTA). Recently, NANOGrav, EPTA+InPTA, PPTA, and CPTA announced evidence for nanohertz stochastic gravitational wave background (SGWB) with statistical significance ranging between $2-4\sigma$ (Agazie et al., 2023a; EPTA Collaboration et al., 2023a; Reardon et al., 2023b; Xu et al., 2023). With the next generation, high sensitivity telescopes, such as the Square Kilometre Array (SKA) it will be possible to obtain sufficient signal-to-noise ratio (S/N) within short observation duration to measure the pulse times of arrival (TOA). In the future, a large number of high cadence timing observations on a much larger pulsar sample will be made during the SKA era, which will lead to significant improvements in the detection sensitivity of nanohertz GWs from the PTAs. This will not only facilitate the detection of SGWB at high confidence level, but will also open our horizon towards continuous GWs from individual supermassive black hole binaries, thereby ushering in the era of multi-wavelength GW astronomy. In order to maximise the PTA sensitivity to GWs, a detailed characterisation of the different noise sources is of crucial importance. There are many noise sources that contribute to the uncertainty in the TOAs. Noise can be classified according to several characteristics, one of which is the temporal correlation. A noise with long-term correlation is called red noise. Some examples of red noise include rotational irregularities in the pulsar's spin period, also known as spin noise or timing noise (Boynton et al., 1972; Cordes, 1980; Shannon and Cordes, 2010), temporal variation in the Dispersion Measures (DM) caused by the interstellar plasma (Keith et al., 2013; Tarafdar et al., 2022), and errors in the Solar System ephemeris (Champion et al., 2010). On the other hand, noise without temporal correlation is called white noise. Another feature to classify the different sources of noise is their dependence on the observation frequency. While dispersive delays depend on the frequency, errors in the Solar System ephemeris are achromatic. Furthermore, whether a noise source is common to multiple pulsars or unique to each pulsar is vitally important for distinguishing the GW signal from noise. The PTA experiments attempt to extract the GW signals by modeling these kinds of noise and incorporating them into their data analysis pipelines (Chalumeau et al., 2022; Srivastava et al., 2023; Agazie et al., 2023b; EPTA Collaboration et al., 2023b; Reardon et al., 2023a). Although, many sources of noise are well understood both statistically and physically, there is room for further improvement in noise modeling. Jitter noise refers to the stochastic fluctuations in the pulsar timing residuals without temporal correlations and is one of the noise sources that should be characterised precisely to improve pulsar timing analysis. Such time-uncorrelated noise also includes the radiometer noise originating from the instrument. It's amplitude

depends on the instrument and this noise can be reduced, thereby improving the S/N ratio. On the other hand, jitter noise does not decrease even if the S/N ratio improves and its amplitude is independent of the instrument (Shannon and Cordes, 2012; Shannon et al., 2014; Lam et al., 2016). Hence, this noise is considered intrinsic to each pulsar, and it occurs due to the pulse shape variations on pulse-to-pulse scale. Since it behaves like white noise, its amplitude decreases with an increase in the integration time. However, with the shorter duration of observations, which are likely to be planned for the next generation PTA experiments due to their higher sensitivity, these experiments may suffer from jitter noise, if its implications are not understood properly. Therefore, it is important to investigate the nature and amplitude of the jitter noise with current observational campaigns in order to develop efficient observation strategies for the future.

For this work, we study the jitter noise for the the pulsar PSR J0437−4715. PSR J0437−4715 was discovered in the Parkes 70 cm survey and is the brightest known MSP (Johnston et al., 1993). Due to its high brightness, it has been studied extensively especially for its single-pulse behaviour. (Ables et al., 1997; Jenet et al., 1998; Vivekanand et al., 1998; Vivekanand, 2000; Liu et al., 2012; Oslowski et al., 2014; De et al., 2016).

This pulsar has also been the focus of previous jitter studies, which measured its jitter amplitude at different frequencies (Shannon et al., 2014; Parthasarathy et al., 2021). Shannon et al. (2014) measured its jitter amplitude using 700, 1400, and 3100 MHz observations by the Parkes *Murriyang* telescope, whereas Parthasarathy et al. (2021) investigated the wideband feature of its jitter using the MeerKAT telescope (856 - 1712 MHz). Both studies found that the jitter amplitude of PSR J0437−4715 has a weak frequency dependence, and its amplitude is larger at lower frequencies. PSR J0437−4715 has been subsequently observed by PPTA, MPTA, and InPTA, since it is located in the southern sky. Among these three PTAs, only InPTA covers the low frequency range (300 - 500 MHz). Therefore, we are the only PTA which can investigate whether the jitter amplitude of PSR J0437−4715 is actually getting larger in the lower frequency bands and this investigation has important ramifications for developing a future strategy for low-frequency timing observations.

In this paper, we report the pulse jitter measurements of PSR J0437−4715 for low (300 - 500 MHz) and mid (1260 - 1460 MHz) radio frequency observations using the uGMRT. The rest of this paper is structured as follows: In Section 3.2, we briefly describe the observations used in this work and the data processing methods used for analysis. In Section 3.3, we describe the methodology used for estimating jitter noise and the results of these measurements. In Section 3.4, we discuss the inferences and conclusions made from our analysis. Finally, we summarize our findings and conclude in Section 3.5.

3.2 Observations and Data processing

3.2.1 Observations

In this work, we have used the observations of PSR J0437−4715 conducted using uGMRT (Gupta et al., 2017) as a part of the InPTA experiment from the observation Cycle 41 to 44 (October 2021 to September 2023). The InPTA observations were carried out either using two sub-arrays of 10 to 15 antennae at Band 3 (300 - 500 MHz) and Band 5 (1260 - 1460 MHz), respectively or using the complete array set at Band 3. Band 3 data were coherently dedispersed to the known DM of the pulsar using a real-time pipeline (De and Gupta, 2016). The Julian dates and S/N ratio for each epoch used for our analysis can be found in Table 5

Table 5: Band 3 observations used in this work and their estimated jitter amplitudes. The first column lists the uGMRT observation cycle. The second column shows the date of the observations. The third column gives the integrated S/N ratios for this band obtained from the `pdmp` command of `PSRCHIVE` software package. The fourth column is the observation duration in seconds. The last column shows the ECORR value scaled to one hour and these values are plotted in Figure 14. The bottom six epochs were selected to see the difference between Band 3 and 5 for the same epochs (see Section 3.2.2).

Cycle	MJD	S/N	Duration (s)	ECORR (ns)
41	59545	16401	1198	$63.36^{+4.53}_{-4.23}$
41	59587	8667	1799	$64.84^{+4.64}_{-4.33}$
41	59627	7571	1018	$53.06^{+3.38}_{-3.12}$
41	59656	6602	1020	$64.32^{+5.04}_{-4.49}$
41	59665	4772	1320	$47.79^{+4.25}_{-3.93}$
42	59692	5196	719	$68.48^{+6.51}_{-5.64}$
42	59701	14708	720	$52.70^{+5.08}_{-4.64}$
42	59730	10452	718	$52.04^{+4.90}_{-4.35}$
42	59789	13307	718	$59.32^{+5.78}_{-4.95}$
42	59800	11717	718	$64.58^{+5.85}_{-5.16}$
43	59908	12651	598	$52.70^{+3.77}_{-3.52}$
43	59918	10150	720	$31.76^{+3.06}_{-2.79}$
43	59928	13041	597	$47.86^{+5.20}_{-4.51}$
43	59989	11379	660	$53.05^{+5.26}_{-4.57}$
43	60021	18320	1496	$52.98^{+3.43}_{-3.09}$
44	60063	5487	600	$52.07^{+6.08}_{-5.29}$
44	60121	12228	598	$56.33^{+5.85}_{-5.04}$
44	60139	6250	600	$49.49^{+5.56}_{-4.78}$
44	60160	13017	598	$68.70^{+7.01}_{-6.04}$
44	60178	23971	600	$50.24^{+5.18}_{-4.38}$
41	59575	2596	1318	$63.19^{+6.20}_{-5.86}$
42	59818	2627	719	$53.93^{+6.58}_{-5.87}$
43	59982	5265	900	$49.72^{+4.81}_{-4.25}$
43	60002	6942	720	$61.90^{+6.40}_{-5.73}$
44	60055	4930	900	$55.58^{+5.37}_{-4.87}$
44	60149	5211	720	$53.54^{+5.45}_{-4.77}$

Table 6: Band 5 observations used in this work. The different columns refer to same parameters as in Table 5.

Cycle	MJD	S/N	Duration (s)	ECORR (ns)
41	59545	1253	1215	$61.92^{+4.43}_{-4.13}$
41	59565	1126	1034	$56.47^{+6.89}_{-7.29}$
41	59575	1647	1334	$61.92^{+5.97}_{-5.45}$
41	59627	1465	1033	$57.15^{+7.24}_{-6.91}$
41	59665	1332	1345	$66.51^{+6.94}_{-6.40}$
42	59692	1431	734	$58.28^{+7.01}_{-6.22}$
42	59782	938	733	$46.57^{+9.43}_{-9.86}$
42	59810	1044	733	$49.33^{+8.60}_{-8.36}$
42	59818	1696	734	$43.84^{+5.35}_{-4.77}$
42	59838	2115	734	$56.47^{+5.45}_{-4.97}$
43	59898	1237	720	$61.92^{+7.56}_{-6.73}$
43	59918	1328	720	$64.90^{+10.15}_{-9.65}$
43	59959	730	901	$54.66^{+10.68}_{-11.01}$
43	59982	851	901	$61.92^{+7.56}_{-6.73}$
43	60002	812	721	$42.02^{+12.08}_{-20.46}$
44	60055	954	901	$60.28^{+8.91}_{-8.23}$
44	60149	1470	722	$50.93^{+6.76}_{-6.14}$
44	60191	1450	720	$52.17^{+6.43}_{-5.77}$

and 6 for Band 3 and Band 5, respectively. More details about the InPTA observations and the associated observing strategy can be found in Tarafdar et al. (2022) and Joshi et al. (2022).

3.2.2 Data processing

The processing of uGMRT pulsar observations was done using the `pinta`[1] (Susobhanan et al., 2021) pipeline. Here, we briefly summarize the data processing steps involved. More details can be found in (Susobhanan et al., 2021) (and references therein):

1. Convert the raw data to filterbank format while automatically removing RFI using `RFIClean`[2] (Maan et al., 2021).

2. Convert the RFI-mitigated filterbank file to a partially folded file in PSRFITS format using `DSPSR`[3] (van Straten and Bailes, 2011).

[1] https://github.com/inpta/pinta
[2] https://github.com/ymaan4/RFIClean
[3] https://dspsr.sourceforge.net

Table 7: Parameters used in `pinta` reduction. The first column is the local oscillator frequency of the observing band. The second column is the number of phase bins. The third column is the number of frequency channels. The fourth columns denotes the observation bandwidth. The fifth column is the sampling time used for observation. The sixth column is the sideband. The seventh column is number of polarizations. The eighth column is the duration of individual sub-integrations. The last column is whether the data has been coherently dedispersed (1) or not (0). More details on the description of these parameters can be found in (Susobhanan et al., 2021).

Parameters	Frequency [MHz]	$N_{\rm bins}$	$N_{\rm chan}$	Band width [MHz]	$T_{\rm smpl}$ [μs]	Sideband	$N_{\rm pol}$	$T_{\rm subint}$ [s]	Coheded
Band 3	500	1024	128	200	5.12	LSB	1	10	1
Band 5	1460	128	1024	200	40.96	LSB	1	10	0

3. Find an optimal period and DM, and calculate the integrated S/N using the `pdmp` command provided by `PSRCHIVE`[4] software package (Hotan et al., 2004; van Straten et al., 2012).

The resulting S/N values were used for selecting the optimal observations analyzed in this paper. We selected five epochs from each cycle for both Band 3 and Band 5, except for Band 5 in Cycle 44, since we did not have enough high S/N epochs. We also analysed six additional epochs, which have moderate S/N ratio in Band 3, and which were already selected for Band 5, to check the difference between Band 3 and 5 in the same epoch. In total, we analysed 26 epochs for Band 3 and 18 epochs for Band 5 as listed in Table 5 and 6, respectively. The pipeline parameters used are listed in Table 7.

To measure the timing residuals, we used the `PSRCHIVE` and `TEMPO2`[5] software packages (Hobbs et al., 2006). Using the `pam` command of `PSRCHIVE`, we first collapsed all the frequency channels into eight sub-bands after de-dispersing them. Then, we created a noise-free and frequency resolved profile template using the `psrsmooth` command. Thereafter, we measured the TOAs for each sub-integration and each sub-band by calculating the cross-correlation between the observed profile and the template, using the `pat` command. Using these TOAs and the corresponding par file, we calculated the timing residuals using `tempo2` and removed the TOAs with large uncertainties from a visual check. Finally, we carried out parameter fitting using only the spin frequency and DM since the observations typically span 10 minutes in duration.

3.3 Jitter measurements

In this section, we first describe the noise models and the methods used to measure the jitter amplitudes. Thereafter, we present the results of jitter measurements.

Traditionally, the jitter amplitudes have been estimated by computing the quadrature difference of the root-mean-square (rms) of frequency averaged residuals, $\sigma_{\rm obs}$ and the rms expected from the radiometer noise, ($\sigma_{\rm rad}$):

$$\sigma_{\rm J}^2(T) = \sigma_{\rm obs}^2(T) - \sigma_{\rm rad}^2(T), \tag{67}$$

where T is the length of a sub-integration. We can estimate $\sigma_{\rm rad}$ by considering the Gaussian noise expected from the observed TOA uncertainties. The simulated TOAs can be obtained using the `fakepulsar` method

[4] https://psrchive.sourceforge.net/index.shtml
[5] https://bitbucket.org/psrsoft/tempo2/src/master/

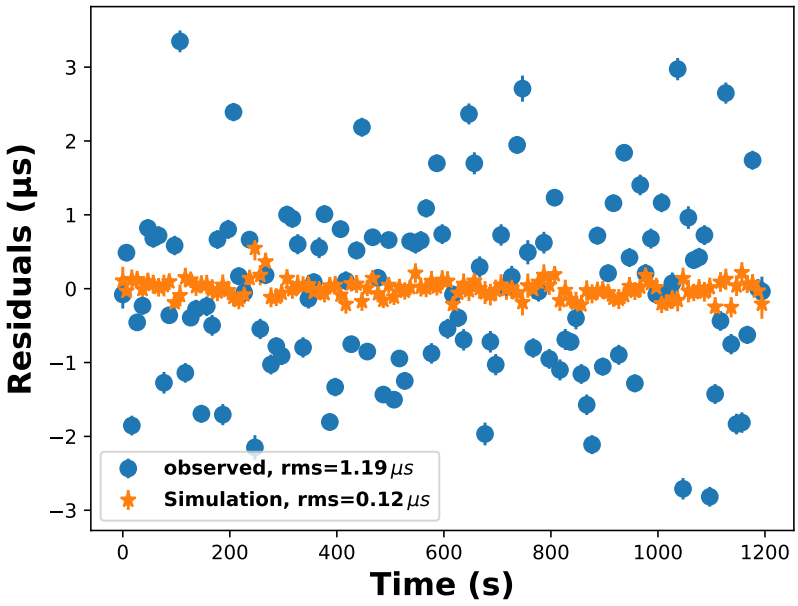

Figure 11: An example of the frequency-averaged timing residuals. The blue circles and orange stars denote the observed residuals obtained from 10 s sub-integrated profiles and residuals obtained with `libstempo` simulation, respectively (see the beginning of Section 3.3). The TOAs are obtained from Cycle 41 Band 3 observations for MJD 59545.

of the `libstempo`[6] package, with the frequency averaged TOAs and errors as input. The simulated timing residuals are encoded in an array with the same length as the total number of ToAs, which is filled with zeros. Then we can obtain the timing residuals containing radiometer noise by adding Gaussian noise using `add_efac` option. The rms of the timing residuals is denoted by $\sigma_{\rm rad}$. We obtain $\sigma_{\rm rad}$ with 1000 realisations and then calculated the jitter amplitude $\sigma_{\rm J}$ using equation 67. One example of the frequency averaged timing residuals and the simulated residuals is shown in Figure 11. We can see that the frequency averaged timing residuals have large fluctuations compared to the simulated timing residuals, suggesting that the remaining TOA fluctuation is due to pulse jitter. Jitter noise behaves like a white noise source and hence its amplitude scales inversely with the square root of the integration time, as shown below

$$\sigma_{\rm J}(T_1) = \sigma_{\rm J}(T_2)\sqrt{T_2/T_1}. \tag{68}$$

For the rest of the paper, we report the jitter amplitudes as derived from our analysis here, after rescaling them to one hour for ease of comparison with previous studies.

3.3.1 Noise model

For the purpose of this study, we use Bayesian inference to estimate the jitter amplitude and use the traditional method described in the beginning of this section for crosscheck. In this subsection, we briefly describe the

[6] https://github.com/vallis/libstempo/

noise model used to estimate the jitter amplitude in this work. The following description is based on previous works, (Lentati et al., 2014; van Haasteren and Vallisneri, 2014; Arzoumanian et al., 2015; Srivastava et al., 2023), where more details can be found.

The observed timing residuals can be defined in terms of an $N_{\rm TOA}$ length vector, where $N_{\rm TOA} = N_{\rm subint} \times N_{\rm subband}$ for the given observation, and can be modelled as a sum of various deterministic and stochastic noise sources. Since we are interested in the stochastic noise within a single epoch, we assume that the timing residual vector $\delta\mathbf{t}$ can be fully described by the white noise term after removing the deterministic term. Therefore, the likelihood function can be written as follows:

$$L(\delta\mathbf{t}|\theta) = \frac{1}{\sqrt{(2\pi)^{N_{\rm TOA}}\det(\mathbf{C}(\theta))}} \exp\left(-\frac{1}{2}\delta\mathbf{t}^T\mathbf{C}(\theta)^{-1}\delta\mathbf{t}\right), \tag{69}$$

where $\mathbf{C}(\theta)$ is the covariance matrix and θ is a set of parameters.

In pulsar timing analysis, there are three parameters that are used to characterize white noise: EFAC, EQUAD, and ECORR. EFAC is a multiplicative scale factor that corrects for the underestimation of the TOA uncertainty that may be due to errors in calibration. EQUAD is a term that adds white noise in quadrature to represent the range of fluctuations beyond the TOA uncertainty. ECORR is similar to EQUAD, where white noise is again added in quadrature, but ECORR is uncorrelated in different time bins, but perfectly correlated at different frequencies. It represents the fluctuation of the TOA due to pulse profile variation. Therefore, ECORR corresponds to the jitter. EQUAD also corresponds to jitter as far as a single sub-band TOA is concerned. In this work, we use EFAC and EQUAD, when we estimate the jitter amplitude for each sub-banded TOA, and use EFAC and ECORR from the whole set of TOAs. We used the following three models to estimate the jitter amplitude:

Model I common EFAC and ECORR throughout the band.

Model II common EFAC throughout the band and different EQUAD for each sub-band.

Model III different EQUAD for each sub-band without EFAC.

In Model I, ECORR corresponds to the jitter amplitude for the given band. In Model II and III, we estimate the jitter for each sub-band. The aim of the Model III is to eliminate any correlation between the sub-bands since we use common EFAC in the Model II. The covariance matrix for each model is written as follows: [7]

$$\text{Model I} \quad \mathbf{C}_{ij} = F^2\sigma^2_{{\rm TOA},i}\delta_{ij} + J^2\delta_{t_i,t_j} \tag{70}$$

$$\text{Model II} \quad \mathbf{C}_{ij} = \left(F^2\sigma^2_{{\rm TOA},i} + Q^2_{{\rm v}_i}\right)\delta_{ij} \tag{71}$$

$$\text{Model III} \quad \mathbf{C}_{ij} = \left(\sigma^2_{{\rm TOA},i} + Q^2_{{\rm v}_i}\right)\delta_{ij} \tag{72}$$

where $\sigma_{{\rm TOA},i}$ is the uncertainty of the ith TOA. F, J refer to EFAC and ECORR, respectively. $Q_{{\rm v}_i}$ denotes EQUAD for the ith sub-band. The index t_i represents the sub-integration of the ith TOA to incorporate

[7] In the modern definition of EQUAD, EQUAD is defined with EFAC multiplied, but since we are interested in measuring the jitter amplitude in Eq 67 with Bayesian framework, we adopt the definition of `temponest` without EFAC applied.

ECORR in the same sub-integration. We used uniform prior distribution in [0.5, 5.0] for EFAC and log-uniform prior distribution in [-10.0, -5.0] for EQUAD and ECORR.

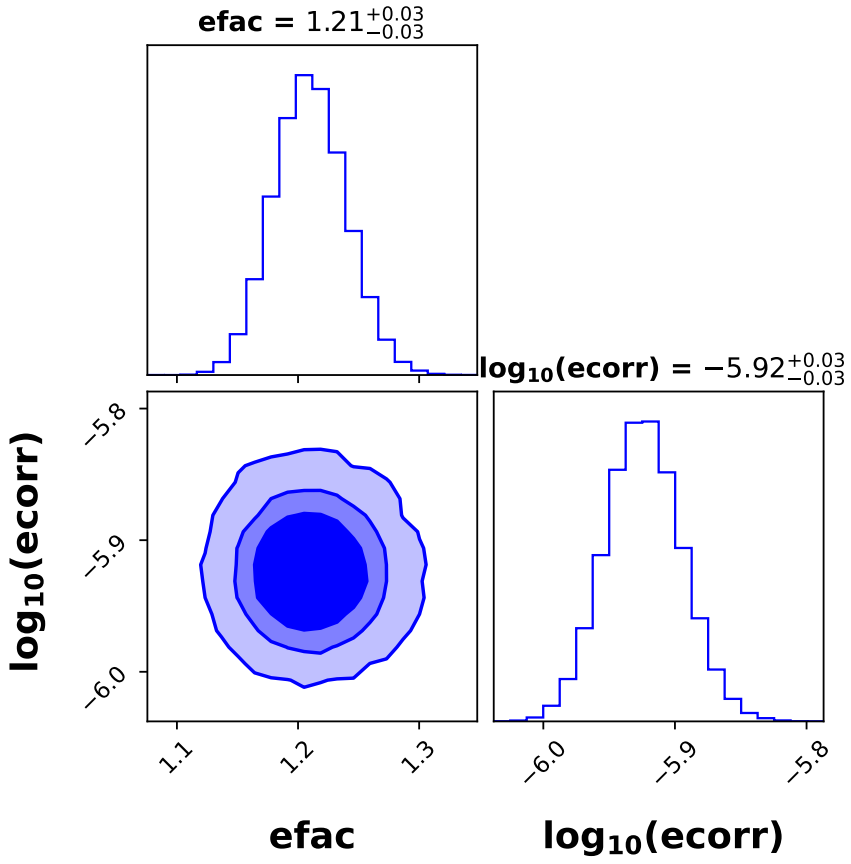

Figure 12: An example of the posterior distribution with 68%, 90%, 99% credible intervals of the Model I parameter estimation. The point estimates shown above the plots represent the median values and marginalized 68% credible intervals. The TOAs are obtained from Cycle 41 Band 3 observations on MJD 59545.

3.3.2 Data Analysis

To measure the jitter amplitude using Bayesian inference, we used the `libstempo` and the `ENTERPRISE` python packages (Ellis et al., 2020). We used the sub-banded TOAs and the corresponding `par` file as input. We then define the likelihood function depending on the Model I-III, from which the noise parameters are then estimated. We used the Markov Chain Monte-Carlo (MCMC) sampler implemented in the `PTMCMCSampler` package (Ellis and van Haasteren, 2017) to sample the posterior and estimate the EFAC and ECORR or EQUAD. One example of such a posterior plot along with the marginalized posteriors for EFAC and ECORR is shown in Figure 12.

As mentioned at the beginning of Section 3.3, we rescale the estimated values of EQUAD and ECORR to one hour duration, using the same scaling relation as in equation (68). However, in order to reaffirm they would follow the same relation as equation (68), we recalculate ECORR for Model I by changing the sub-

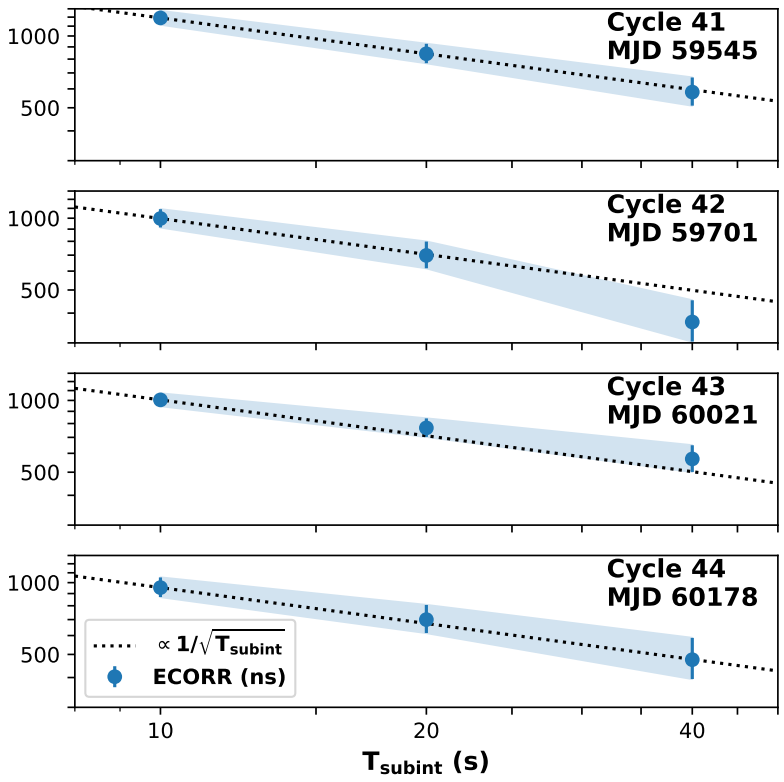

Figure 13: ECORR obtained with different sub-integration. Blue circles denote the ECORR values obtained from different sub-integration times. The black dotted lines shows the fit, which is proportional to the inverse square root of the sub-integration times.

integration time to 20 and 40 seconds. The result is shown in Figure 13, and we confirm that ECORR also follows the correct scaling law in accord with equation (68). Although we do not have data for observation durations longer than 1 hour, we assume that the scaling law holds even if the integration time is extended to one hour. Therefore, we scaled the jitter amplitude obtained by Bayesian analysis to one hour.

As a consistency check, we also verify whether the ECORR values obtained with `ENTERPRISE` are consistent with the jitter amplitude obtained with the traditional method described in the beginning of this section. We see that all the σ_J agree with the ECORR values to within 1σ, thereby showing that our results are self-consistent.

3.3.3 Jitter amplitude within the band

Using the TOAs obtained by the method described in Section 3.2.2, we obtained ECORR values for all the selected epochs listed in Tables 5 and 6, for Model I of Section 3.3.1, which considers ECORR as a proxy for the jitter amplitude throughout the band. The resulting values of ECORR are rescaled to one hour and are listed in column 5 of Tables 5 and 6.

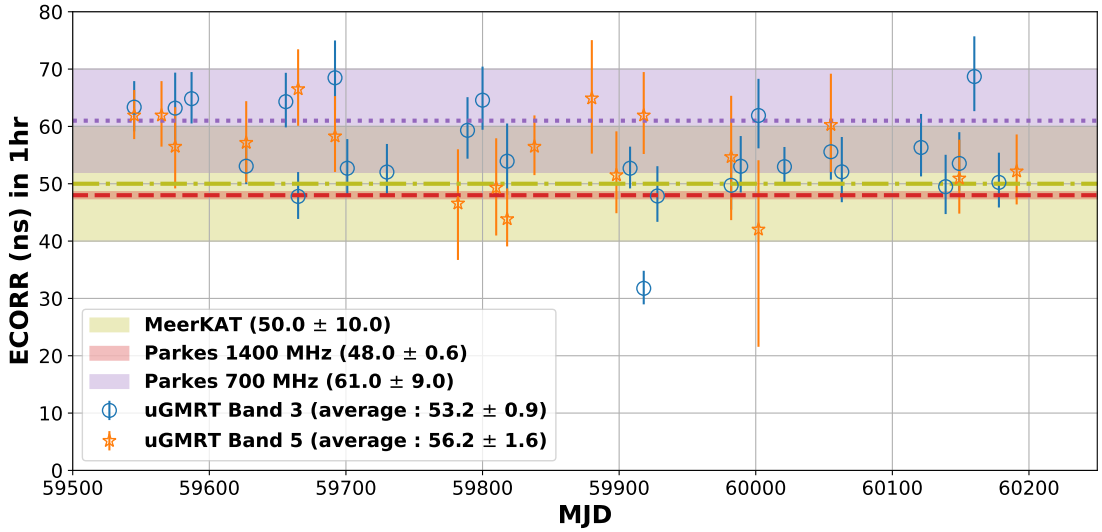

Figure 14: ECORR time series scaled to one hour obtained from Model I estimation. The blue circles and orange stars denote the ECORR values obtained from Band 3 and Band 5 observations, respectively. The purple shaded region and the dotted line show the results of MeerKAT observations (Parthasarathy et al., 2021). The red shaded region and the dashed line and the yellow shaded region and dot-dashed line show the corresponding results for the Parkes observations (Shannon et al., 2014). Note that the values shown in the previous studies are not ECORR, but σ_J defined by the equation (67), which is measured by the traditional method described in the beginning of Section 3.3.

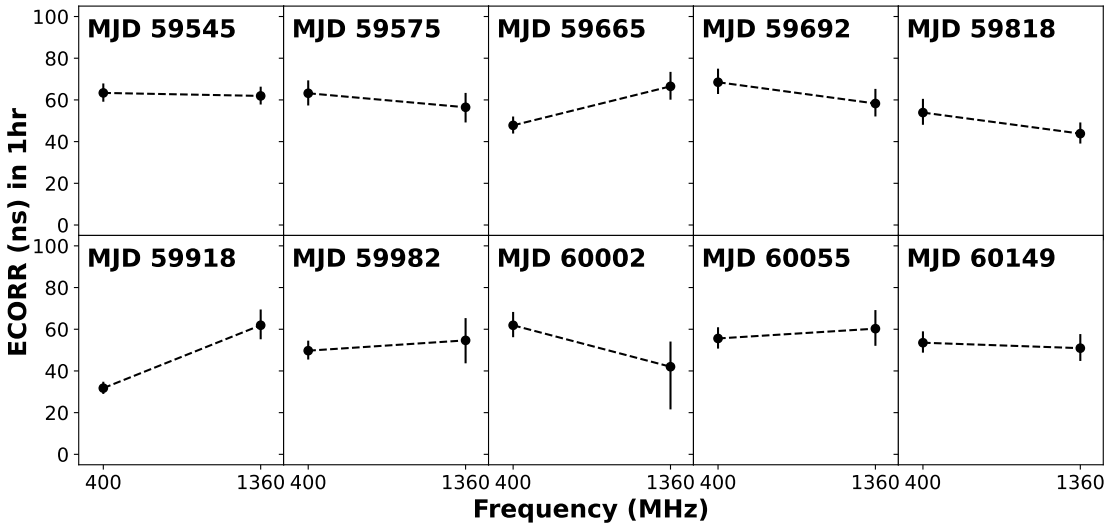

Figure 15: Comparison plots of ECORR for Band 3 and Band 5 for the same epoch obtained from Model I estimation.

The rescaled ECORR values are plotted in Figure 14 for each epoch. We estimate the weighted average of ECORR to be 53.2 ± 0.9 ns in Band 3 and 56.2 ± 1.6 ns in Band 5 from our observations. We see that our Band 5 result is consistent with Parthasarathy et al. (2021). The jitter amplitude in Shannon et al. (2014) was reported for a single observation only. Though our weighted average value for Band 5 differs from that quoted in Shannon et al. (2014), the spread in our overall results ensures that we are in good agreement with Shannon et al. (2014) as well.

Our results for ECORR at Band 3 are the first jitter measurements calculated for PSR J0437−4715 below 700 MHz. Therefore, we do not have previous studies to directly compare our results. The frequency dependence suggested by Shannon et al. (2014) and Parthasarathy et al. (2021) point to a higher jitter at lower frequencies. The results we derive are, however, not in agreement with this conclusion, since we find ECORR at Band 3 is consistent with that seen in Band 5. We see that the weighted average of the jitter amplitude at Band 3 is lower than that of Band 5. We calculated the weighted average again after excluding the epoch corresponding to MJD 59918, since it is likely to be an outlier and strongly affected by scintillation. This gave a new weighted average value, $= 55.47 \pm 0.94$ ns, of jitter at Band 3. Therefore, even after removing the outlier, the jitter in Band 3 is consistent with that in Band 5 within 1σ. One possible reason that the jitter in Band 3 is not so large could be due to epoch to epoch variations, since we are comparing different epochs. In Figure 15, we plot the ECORR values for Band 3 and Band 5 from a single epoch, for comparing their behaviour. We see that while there are some epochs where the jitter in Band 3 is larger, there are also epochs where the jitter values at Band 3 are the same or smaller. From our whole band jitter (ECORR) estimates, we conclude that it is not possible to say with certainty whether the jitter is larger or smaller at lower frequencies than at higher frequencies.

We see that there is a large scatter in the Band 3 jitter estimates. On investigating the Band 3 pulsar profiles in the frequency domain, we find that this scatter in the jitter values might be caused by the scintillation present in many profiles. Further, we notice that in this band, the S/N varies significantly with frequency and from epoch to epoch which, again, can possibly be explained by the presence of interstellar scintillation in the data. This may have caused the failure in measuring the fluctuations of the timing residuals for some of the sub-bands which have low-S/N, thereby resulting in higher jitter estimates. As a result, we further scrutinize the Band 3 data for further insights on the nature of jitter.

3.3.4 Intra-Band Frequency dependence of Jitter

In Section 3.3.3, we have demonstrated that the jitter estimates at low frequency may be affected by scintillation. This prompted us to look at the sub-banded data to get additional insight into the nature of jitter in the different frequency channels of Band 3. In this analysis, we attempted to measure EQUAD for each sub-band using Model II and III from the 20 highest S/N epochs listed in Table 5. EQUAD is used to account for the unaccounted (besides telescope noise) noise in the TOA uncertainty, and it corresponds to the jitter amplitude estimated using the traditional method described in the beginning of Section 3.3 (Shannon et al., 2014; Parthasarathy et al., 2021).

Learning from our experience in Section 3.3.3, where low S/N hindered us from getting accurate jitter estimates at Band 3, we obtain credible EQUAD values by first calculating the sub-banded S/N and then adopting

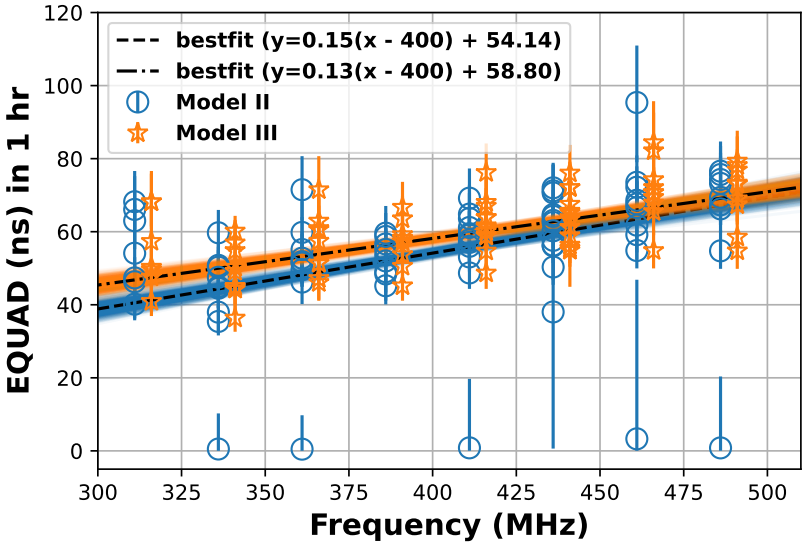

Figure 16: Sub-banded EQUAD scaled to one hour obtained from Model II and III estimation for the sub-bands which had the S/N_{sub} above the threshold value. The blue circles and orange stars represent the sub-banded EQUAD value of Model II (with EFAC) and III (without EFAC), respectively. The orange stars have been offset by 5 MHz to the right for clarity. The blue and orange shaded lines are from 500 random lines obtained from the posterior distribution of Bayesian regression. The reduced χ^2 of the best-fit lines are equal to 4.8 for Model II and 1.7 for Model III.

these EQUAD values only from the high S/N observations that lie above a given threshold. The sub-banded S/N is defined as follows:

$$S/N_{sub} = \frac{\sum_{i,j} I_{i,j}}{\sigma_I}, \tag{73}$$

where $I_{i,j}$ is the intensity of i^{th} phase bin and j^{th} sub-integration in a certain subband, $\sigma_I = \sqrt{\sum_i \sigma_{I,i}^2}$ is the rms of the intensity in a certain subband, and $\sigma_{I,i}$ is the rms of the intensity in the i^{th} phase bin. We used the median value of the S/N_{sub} as our threshold, which is equal to $S/N_{sub} = 2606$.

The results from parameter estimation for Model II and III are shown in Figure 16, which clearly shows a tendency for an increase in EQUAD with frequency for both the models. To reaffirm this quantitatively, we performed a Bayesian regression and estimated the slope (a), and EQUAD at 400 MHz (Q_{400}) using the `emcee`[8] MCMC sampler (Foreman-Mackey et al., 2013). We used the following regression model:

$$y = a(f - 400) + Q_{400} \tag{74}$$

where f is frequency. After performing the regression, we randomly sampled 500 values from the posterior distribution of a and Q_{400}, and then the results using these values are depicted as the blue and orange regions in Figure 16. We see that the lines have a positive slope implying an increase in EQUAD with frequency, a trend that is opposite to that of Shannon et al. (2014) and Parthasarathy et al. (2021).

The posterior distributions of a and Q_{400} are shown in Figure 17 and 18, respectively. These plots show that

[8] https://github.com/dfm/emcee

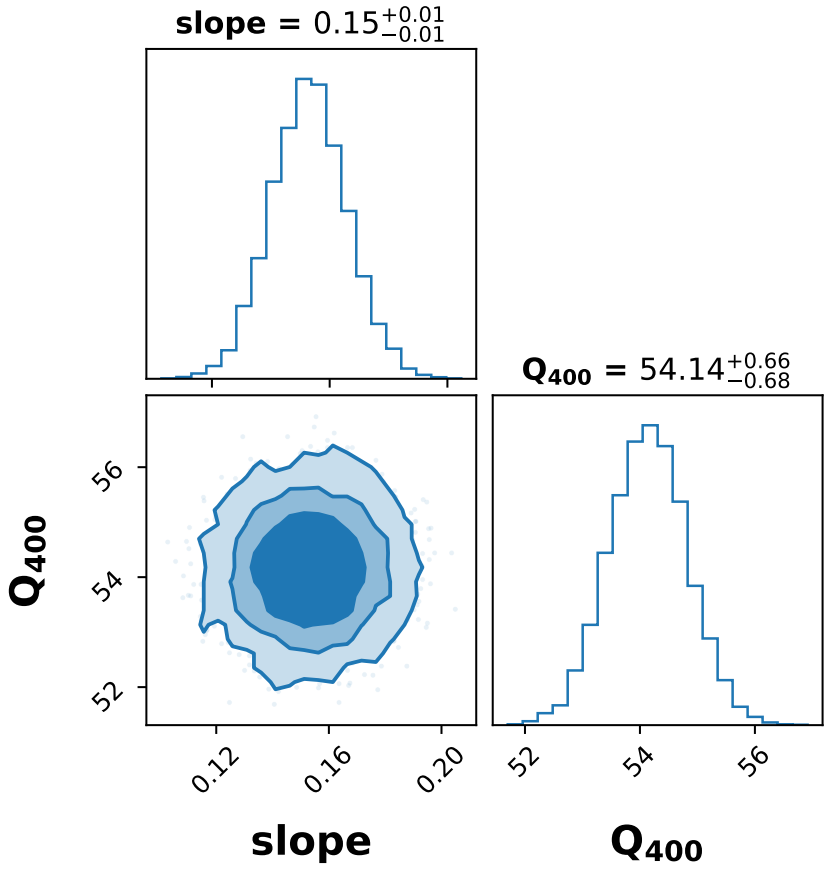

Figure 17: Posterior distributions with 68%, 90%, 99% credible intervals for the parameters fitted using Model II in Figure 16. The point estimates shown above the plots represent the median values and marginalized 68 % credible intervals.

the slopes have a positive value with significance of about 15σ. The plots also list the value of Q_{400}, or the jitter amplitude at 400 MHz, which is about $54.14^{+0.66}_{-0.68}$ ns, in the Model II and $58.83^{+0.63}_{-0.63}$ ns, in the Model III.

3.3.5 Jitter and the DM variations

The previous work (Parthasarathy et al., 2021) raised the concern of the jitter being the limiting factor in the DM precision measurements from shorter duration observations in all MSPs, and suggested that it can only be overcome by longer integrations, based on their analysis in the high frequency regime. We investigated the effect of jitter on the DM precision in the low frequency regime (300 MHz - 500 MHz) by studying the timing residuals and obtaining the DM uncertainties for 10 sec sub-integrations from a 20 minute observation done at the uGMRT.

We measured the timing residuals from each of its 10 second sub-integrations, where each sub-integration is divided into eight frequency channels. We plot in Figure 19, a small subset of the post-fit timing residuals derived from the TOAs. These are plotted serially in time, with each TOA observation being 10 seconds long.

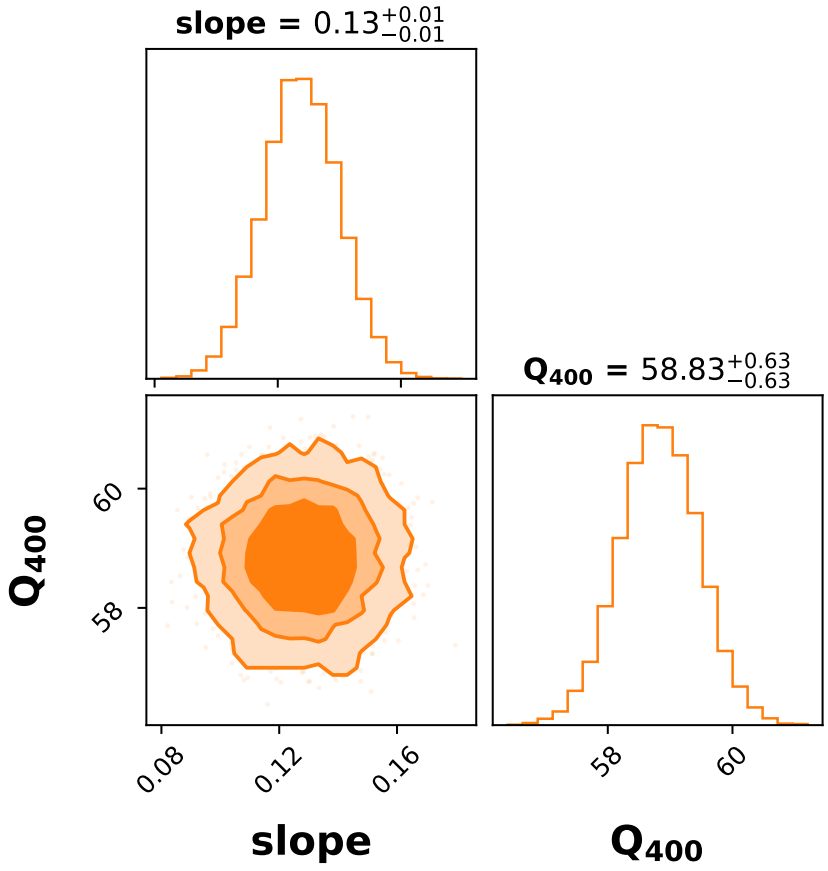

Figure 18: Posterior distributions with 68%, 90%, 99% credible intervals for the parameters fitted using Model III in Figure 16. The point estimates shown above the plots represent the median values and marginalized 68 % credible intervals.

The residuals are colour coded for a given frequency sub-band (as mentioned in Figure 19). There seems to be a dependence of the TOAs on frequency on a 10 second timescale, which may be due to the frequency dependence of DM. The dependence of the TOA on frequency at Band 3 is, however, not as strong as that shown for the high frequency regime in Parthasarathy et al. (2021). This probably implies a smaller spread in DM at Band 3 compared to that in higher frequency band reported in Parthasarathy et al. (2021).

To explore this, we measured the DM values independently from the TOAs of each 10 second sub-integration of the observation. From this, we estimated the median DM to be 2.64386 $\mathrm{cm}^{-3}\,\mathrm{pc}$ and a standard deviation of $8.4 \times 10^{-5}\mathrm{cm}^{-3}\,\mathrm{pc}$. This is shown graphically in Figure 20. We conclude that the scatter in DM is less at Band 3 compared to higher frequency bands (see figure 4 of Parthasarathy et al. (2021)).

Further, to understand the effect of jitter on the DM precision measurements and to get one more independent check on the DM estimation from observations alone, we use the following equation to derive the resultant error in the DM estimation:

$$\Delta t = 4.15 \times 10^{6} (\mathrm{ms}) \left(\frac{1}{f_1{}^2} - \frac{1}{f_2{}^2} \right) \mathrm{DM}, \tag{75}$$

where Δt is the delay in TOAs at the two observing frequencies, f_1 and f_2.

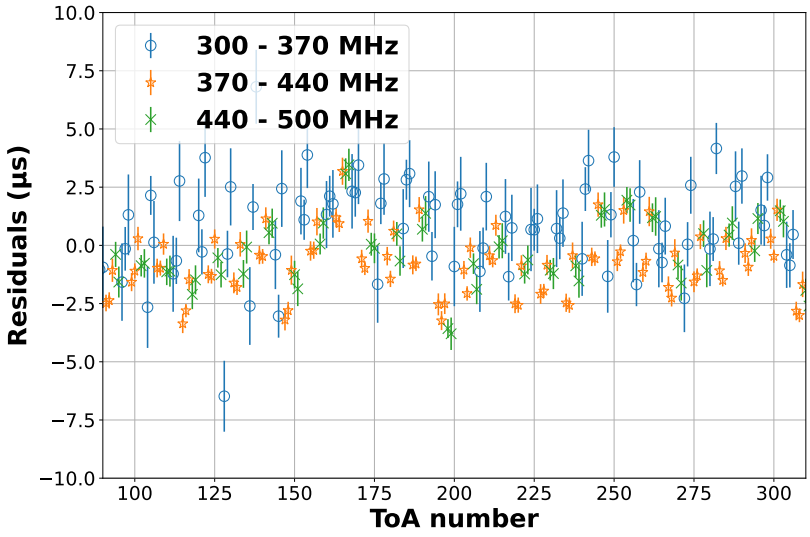

Figure 19: A subset of the 'Post-fit timing residuals' of PSR J0437−4715 estimated using 10 second sub-integrated profiles with each having eight frequency channels. The TOAs are subdivided and colour coded as three sets based on the frequency sub-band as shown in the figure. These residuals are plotted serially against the TOA numbers, to check for any potential frequency dependence and its variation for each TOA set in the plotted subset. The complete observation spanned 20 minutes, and only a subset is plotted in this figure for clarity.

As shown in Sections 3.3.3 and 3.3.4, the pulse jitter is frequency dependent. In Band 3, it has a larger value at higher frequencies, as can be seen from figure 16. To estimate the contribution of pulse jitter in the DM precision, we calculate jitter for a 10 second sub-integration at the two extreme frequencies of our observation, namely 311 MHz and 486 MHz, using equation (68). We find the jitter estimate for a 10 second observation to be 1121.69 ns and 1287.87 ns for 311 and 486 MHz, respectively. Assuming the error in TOAs to be due to jitter alone, we infer the DM error to be $\sim 6.7 \times 10^{-5}\mathrm{cm}^{-3}\,\mathrm{pc}$ which is marginally less than our observationally derived error of $\sim 8.4 \times 10^{-5}\mathrm{cm}^{-3}\,\mathrm{pc}$. However, the error in the TOAs is not due to jitter alone and the other major factor which contributes to this error is the telescope noise. This observation on which the analysis is done is a high S/N observation, with a S/N of at least 1000 for each 10 second sub-integration. Hence in this case, the telescope noise is about $\sim 10^{-6}$, which is slightly less than the jitter noise of $\sim 1.71 \times 10^{-6}$, and therefore, we can assert that the error in TOAs is dominated by the jitter noise in high S/N *but* lower integration time observations. Including the contribution of telescope noise in the aforementioned analysis increases the DM error marginally, $\sim 7.8 \times 10^{-5}\mathrm{cm}^{-3}\,\mathrm{pc}$. Thus, our two independent analyses for the DM uncertainties are in good agreement with each other, thereby providing confidence in our inferences for the jitter measurement and its effect on the DM precision.

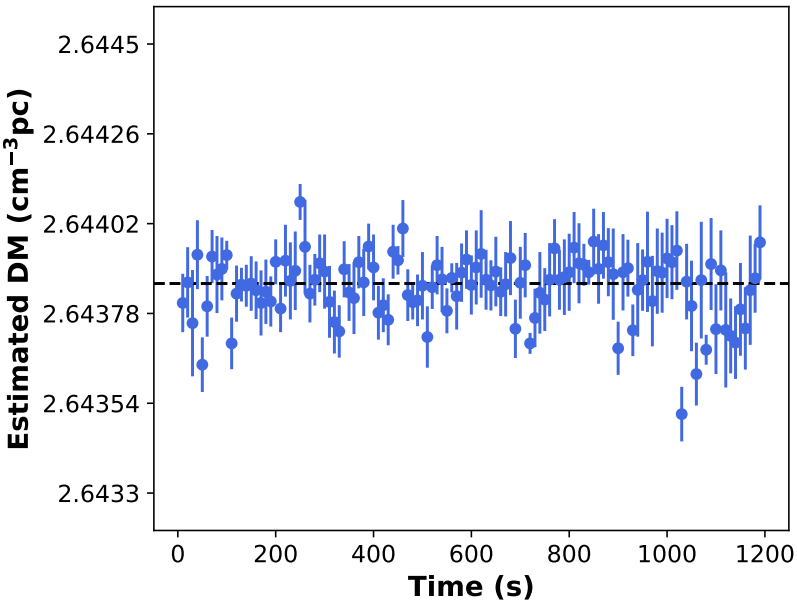

Figure 20: The estimated DM values for each 10 second sub-integration from `psrfits` to the timing residuals shown in Figure 19. The horizontal dotted line represents the median estimated DM value of 2.64386 cm^{-3} pc

3.4 Discussion

3.4.1 Origin of the frequency dependence in jitter

Our analysis of the high S/N Band 3 observations of PSR J0437−4715 reveals a positive correlation of jitter with frequency, as shown in Section 3.3.4. Therefore, we find an opposite trend than that suggested by Shannon et al. (2014) and Parthasarathy et al. (2021) for their higher frequency observations. It could be due to two possible reasons. One is due to the possibility that the pulse profile is more stable at lower frequencies than at higher frequencies in Band 3. This is because jitter is caused by pulse profile variation in the pulse-to-pulse scale. And secondly, there seems to exist a *turnover* frequency region at which the jitter trend reverses. This region seems to exist between 500 MHz and 900 MHz, probably around 700 MHz.

The existence of a turnover frequency region at which jitter behavior changes, can possibly have two interpretations, which we outline below. The first speculation comes from the self-absorption effect in the pulsar magnetosphere. It has been shown that the high frequency radio emission from the pulsar comes from regions closer to its surface, while the low frequency emission comes from regions farther from the surface (Komesaroff, 1970; Cordes, 1978). This is called the radius-to-frequency mapping (RFM). Of the many pulsars studied, most show this trend but there are a few some exceptions (Posselt et al., 2021). Based on the RFM studies, we can say that since the distance of propagation through the emission region is shorter for lower frequencies, these are less sensitive to the self-absorption effects, thereby resulting in more stable profiles than those at higher frequencies. If this is true, the *turnover* frequency of the jitter amplitude could be related to the spectral *turnover* of the pulsar flux density. However, Lee et al. (2022) reported two *turnover* frequencies of the flux density for PSR J0437−4715, which are ~ 285 MHz and ~ 1900 MHz. This

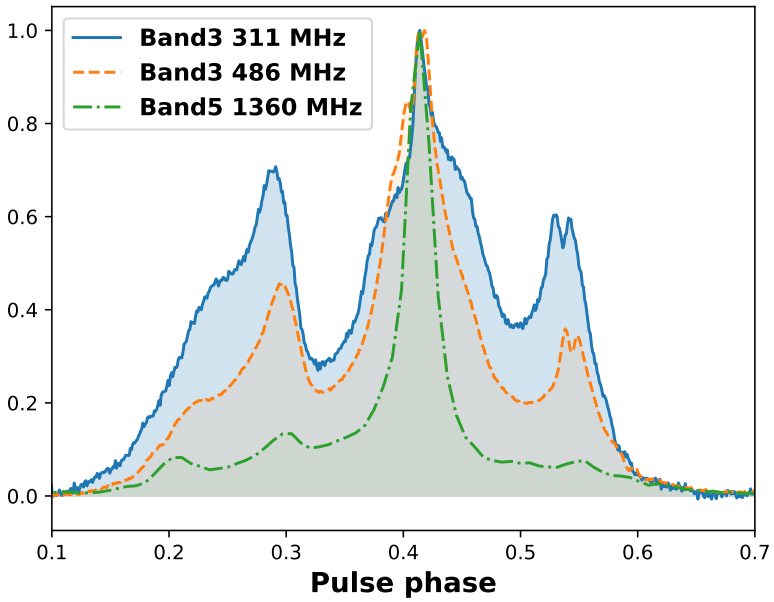

Figure 21: The integrated pulse profile of PSR J0437−4715 at different frequencies. Intensities are normalized. The data used for this plot were obtained from Cycle 41 observation on MJD 59545.

is therefore, not supporting our *ansatz* for the change in the jitter trend. In any case, it remains to be seen how jitter behaves around these two frequencies. A holistic mapping of the jitter trend over the full span of frequency bands will probably provide a clearer picture.

The second possibility comes from the profile evolution studies. The analysis in Shannon et al. (2014) and Parthasarathy et al. (2021) suggested that the possible reason for the smaller jitter at higher frequencies is due to narrower pulses and the larger modulation of the main pulse component at those frequencies. However, our jitter trend is opposite to their results. PSR J0437−4715 seems to have a narrow central component in its profile above 700 MHz (Dai et al., 2015). Comparing 1400 MHz observations with 327 MHz observations for this pulsar, we find relatively more stable precursor and postcursor components at lower frequency (Oslowski et al., 2014; Vivekanand et al., 1998). We notice that the pulse profiles show more significant precursor and postcursor components in our Band 3 observations as well (see Figure 21). This leads us to posit that the reason for the smaller jitter at lower frequencies at Band 3 is due to the fact that these precursor and postcursor components are more stable, and hence they moderate the fluctuations in the TOAs by the central (main) component. To investigate this further we need to study the phase-resolved modulation index of single pulses, which may help to resolve this issue. Hence, it will be worth revisiting single pulse studies of PSR J0437−4715 with our high-sensitivity, wideband observations, which will be defered to a future paper.

3.4.2 Effect of jitter on the DM precision measurements

From our analysis, in Section 3.3.5, we see that the DM precision is limited by jitter noise for high S/N observations on short timescales. Further, if we extrapolate the results from Parthasarathy et al. (2021), it would indicate that we cannot get high precision DM just by going to lower frequencies. However, our analysis suggests otherwise, and it might be possible to get even better precision DMs by going to lower frequencies ($\sim$100 MHz). Though the possibility of low frequency giving better DM precision is supported by our analysis at Band 3, it remains to be seen observationally what trend is followed by pulse jitter at that frequency regime .

Further, our analysis in tandem with Parthasarathy et al. (2021) suggests that it is not possible to get DM precision measurements using observations at *two* (high and low) frequencies only. This is because the DM will depend on the jitter coming from both the observed frequencies; and it is entirely possible that those two frequencies may show entirely opposite trends in jitter (e.g., at Band 3 and Band 5). For precise estimates of jitter, we need to be able to extrapolate over multiple bands in a frequency resolved manner, since different frequency bands are likely to give different estimate for order of precision.

A comprehensive understanding of the pulse jitter behaviour over different frequency bands and its effect on DM is warranted for better precision pulsar timing. It also remains to be seen what trend in jitter is followed by different pulsars at different frequency bands. Our data show lower jitter and hence more precise DMs at lower frequencies (than higher frequencies). However, low frequency studies of other pulsars are required to see if this trend is universal. It is very well possible that the trend is opposite for other pulsars and this is a subject of a subsequent analysis.

3.5 Conclusions

In this work, we present the first ever jitter measurements of PSR J0437$-$4715 in the low frequency region (300 MHz - 500 MHz), using Band 3 wideband observations obtained as a part of the InPTA experiment. We were able to estimate the jitter values in both Band 3 and 5 using Bayesian inference. For Band 5, our jitter measurements are in agreement with the previous studies; (Shannon et al. (2014) and Parthasarathy et al. (2021)). In this band, we estimate the weighted average of jitter to be 56.2 ± 1.6 ns. Our Band 3 weighted average value for the jitter is 53.2 ± 0.9 ns, which is lower than that in Band 5. We, thus, see the opposite trend (positive correlation) in the frequency dependence of jitter than that seen in Shannon et al. (2014) and Parthasarathy et al. (2021) (negative correlation). To explore the reason for this, we measured the jitter amplitude in each frequency sub-band also, using sub-banded TOAs from Band 3 observations. The results from the sub-banded data reaffirmed the positive correlation of the jitter amplitude with frequency. Therefore, positive correlation of the jitter with frequency in our low frequency (Band 3) analysis in tandem with the negative correlation of jitter with frequency in high frequency analysis by Shannon et al. (2014) and Parthasarathy et al. (2021) suggests the existence of a *turnover* frequency region for the jitter amplitude. This *turnover* region probably lies somewhere between 500 and 700 MHz and this explains why our jitter amplitude of Band 3 is not as large as expected from previous high frequency studies alone. It would be interesting to explore this *turnover* region further and this *turnover* frequency could possibly be determined by the uGMRT Band 4 (550 - 750 MHz) observations, or the next generation, high sensitivity telescopes,

such as the SKA.

We have also explored the DM measurements for short duration observations and the effect of jitter on its precision. Using two independent approaches, we analysed 10 second sub-integrations of a high S/N epoch to estimate the error in DM measurements. We found that the values inferred from the observational data alone are in good agreement with the analysis done using quasi-theoretical approach, using the estimated jitter values for this pulsar. We conclude that for high S/N *but* short duration observations, jitter is the dominant source of noise and limits the DM precision which for this pulsar is 10^{-5}.

Our interesting results were achieved thanks to the high sensitivity of the uGMRT Band 3 observations. Previous studies have shown that lower frequencies suffer more from jitter noise, but our results suggest otherwise. This may, however, not always be the case. For J0437−4715, the jitter amplitude in Band 3 is about the same as in 1400 MHz, which shows that observations at low frequency are not severely affected by the jitter noise, and we may be able obtain more stable TOAs from observations at frequencies below 300 MHz. Also, low frequency jitter studies of other pulsars are needed for making any conclusive statements on the generic jitter behaviour for pulsars on the whole. Further, for a detailed look into the reason for this opposite trend in jitter, single pulse analysis would be of immense help. Our future studies will provide single pulse analysis of PSR J0437−4715 and other bright pulsars, as well as comprehensive jitter measurements of the whole InPTA pulsar set, which is important for future timing observation strategies for all PTAs.

4 Spectropolarimetry of the bright radio emission from PSR J1107−5907 with the Parkes UWL

4.1 Introduction

Origins of the radio emission from pulsars is poorly understood. For most pulsars the pulse shape averaged over the observation time (the integrated profile), is stable. However, their individual pulses display enormous variations in the shape and intensity. This also include phenomena such as giant pulse emission (Heiles and Campbell, 1970), sub-pulse drifting (Drake and Craft, 1968), mode changing, which has multiple averaged pulse shapes (Backer, 1970), and nulling, in which the pulses suddenly disappear (Rankin, 1986). It is important to investigate these phenomena to understand what causes the radio emission from pulsars.

In this paper we study the emission properties of a particularly unusual pulsar, PSR J1107−5907. PSR J1107−5907 is an isolated, non-recycled pulsar discovered in the Parkes Multibeam Pulsar Survey (Manchester et al., 2001; Lorimer et al., 2006). Its rotational period and derivative are $P \sim 0.25$s and $\dot{P} \sim 9 \times 10^{-18}$.

PSR J1107−5907 is known to exhibit several emission states. O'Brien et al. (2006) reported it has a null state, a weak state with a narrow profile, and a bright state with a broad profile . The bright state has a brightness that is comparable with the Vela pulsar. Young et al. (2014) analyzed the emission behavior of PSR J1107−5907 using observations obtained over 10 years and found that $\sim 6\%$ of the observations were detected the bright state and $\sim 50\%$ in the weak state. They also argued the null state is included in the weak state. On the other hand, Wang et al. (2020) analyzed data that detected the bright state and reported that PSR J1107−5907 (i) never turned off during the weak state, (ii) always turned off after the bright emission. From this they concluded that PSR J1107−5907 indeed does have a null state, which is distinct from the weak state. Hobbs et al. (2016) observed PSR J1107−5907 as part of an ASKAP pilot survey and confirmed that bright emission can last up to 40 minutes. They also estimated that the burst state typically lasts about 3 hours although the transition is not periodic. These properties suggest a similarity to Rotating Radio Transients (RRATs; McLaughlin et al. (2006)).

Wideband observation have opened new windows into understanding the pulsar emission mechanism. The frequency evolution of the pulse profile is important for estimating the structure of the emission region of the beam, since it is believed that pulses are emitted from different emission heights at different frequencies (Komesaroff, 1970; Cordes, 1978; Oswald et al., 2020). The phase variation of the polarisation angle (PA) can be combined with the rotating vector model (RVM; Radhakrishnan and Cooke (1969)) to estimate the angle between the magnetic poles and the rotation axis, leading to an understanding of the magnetospheric structure. Furthermore, pulses propagating in interstellar space are subject to propagation effects, such as dispersion delay and faraday rotation. The dispersion measure (DM) and rotation measure (RM) are the integral of the average electron density and the magnetic field in the line-of-sight direction, respectively, and play an important role in the study of the structure of our Galaxy (Han et al., 1999, 2006; Vallée, 2005; Yao et al., 2017) .

Since its discovery, PSR J1107−5907 has been observed at a wide range of observing frequencies and with various telescopes. Young et al. (2014) and Wang et al. (2020) analyzed observations obtained around 730, 1400, and 3100 MHz using *Murriyang*, the Parkes 64-m radio telescope. The catalogued value of the DM

Table 8: Observations that contain the bright emission state for PSR J1107−5907. The fourth column is duration of the bright state. The fifth column is observation mode. Columns seven to nine list RMs obtained from the `rmfit`, ionospheric RM obtained from `ionFR`, and RM after subtracting the ionospheric contribution from the observed RM, respectively.

MJD	Duration (s)	$T_{\rm bright}$ (s)	Obs. Mode	DM (pc cm^{-3})	RM$_{\rm obs}$ (rad m^{-2})	RM$_{\rm ion}$ (rad m^{-2})	RM (rad m^{-2})
59425	624	624	fold	40.869±0.178	21.96 ± 0.03	1.61±0.10	20.35 ± 0.10
59457	247	247	fold	41.125±0.178	23.80 ± 0.02	1.47±0.08	22.33 ± 0.08
59821	6587	375	search, fold	40.987±0.178	23.71 ± 0.02	2.52±0.09	21.19 ± 0.09

$= 40.75 \pm 0.02$ pc cm^{-3} and the RM $= 25.95 \pm 0.28$ rad m^{-2} were obtained from simultaneous observations with Murchison Widefield Array (150 MHz) and Molonglo Observatory Synthesis Telescope (830 MHz) (Meyers et al., 2018). These multi-frequency, simultaneous observations revealed the pulse profile of the bright state evolves significantly with frequency.

The Parkes radio telescope receive suite includes an ultra wideband low-frequency receiver (UWL), which operates between 704 and 4032 MHz (Hobbs et al., 2020). The UWL receiver allows a detailed study of the frequency evolution of pulse profiles (both for individual pulses and for the integrated pulse profile). As part of an outreach project, PULSE@Parkes (Hobbs et al., 2009), we have made a large number of observations of PSR J1107−5907 using this receiver. In the majority of these observations the pulsar was its weak state and those results will be presented elsewhere (and are publicly available online). However, in three occasions it was observed in its bright state. We therefore here present our wide-bandwidth observations of the bright emission state for PSR J1107−5907. In most PULSE@Parkes observations the observation is folded online at the known period of the pulsar. Therefore we are unable to study individual pulses with those observations. However, on the 30th August 2022 we were successful in obtaining simultaneous fold-mode and search-mode that allows for studies of individual pulses of the pulsar in its bright state.

While we were preparing this manuscript, Sun et al. (2023) also reported wide bandwidth observations from the Parkes telescope for this pulsar. The observations are independent from those reported here and they discussed both the weak and bright emission states. Where there is overlap in the analysis our results are consistent, however here we provide more details on the emission properties of the bright state.

In this paper we describe our observation and data processing in Section 4.2. In Section 4.3, we show results of the wideband analysis. In Section 4.4, we discuss what can we learn from our wideband observations and conclude the paper.

4.2 Observations and data processing

All of the observational data used in this study were obtained with the Parkes *Murriyang* radio telescope (see Figure 22). The data are publicly available from the CSIRO data archive[9] (Hobbs et al., 2011) under the project code P595, PULSE@Parkes, which is an outreach project to high school students. We visually inspected all the P595 observations of PSR J1107−5907 and identified the observations in which it was

[9] https://data.csiro.au

Figure 22: The Parkes radio telescope, *Murriyang*. Image taken by the author.

detected in the bright emission state and recorded using the UWL receiver. Details of these observations are given in Table 8, which lists the date of the observation, the total duration of the observation, the time the pulsar was in the bright state and the observation mode.

In both fold and search modes the data were coherently dedispersed online using the catalogued value of the DM obtained from the ATNF pulsar catalogue (Manchester et al., 2005)[10]. The data were recorded across the entire 3328 MHz bandwidth (from 704 to 4032 MHz) with 1 MHz frequency resolution and four polarisation products. A sub-integration time of 15 seconds with 1024 phase bins was used when producing the fold mode output data products. In search mode we recorded with 256μs sampling and 8-bit quantisation.

Prior to each observation of PSR J1107−5907, an observation was taken at a nearby reference position and injected with the signal from an artificial noise source. These calibration observations were used to calibrate the data sets in both polarisation and flux density.

The fold-mode data were processed with the `PFITS`[11] (Hobbs, 2021) and `PSRCHIVE` [12] software packages (van Straten et al., 2012). We removed radio frequency interference (RFI) by automatically and manually using `pfits_zapProfile` command. Previous observations of PKS 1934−638 along with the reference observation were used for flux calibration. The flux and polarisation calibration was carried out using `pac`, which is part of the `PSRCHIVE` software suite.

For each fold-mode observation we obtained an updated DM value using the `pdmp` software to determine the DM that maximises the S/N of the profile. These DM values are listed in Table 8. The RM values presented in column 7 of Table 8 were measured using the RMFIT package over the entire observed frequency band. The RMFIT identifies the RM that maximises the linear polarisation fraction. Column 8 in Table 8 gives the

[10] https://www.atnf.csiro.au/research/pulsar/psrcat/
[11] https://bitbucket.csiro.au/projects/PSRSOFT/repos/pfits/browse
[12] http://psrchive.sourceforge.net

predicted ionospheric contribution to the RM as determined using the `ionFR`[13] software package (Sotomayor-Beltran et al., 2013a,b). The final column provides our best estimate of the RM as measured over the entire band by subtracting the ionospheric contribution from the observed RM. We also obtained RM measurements as a function of pulse phase. We first extract the polarisation information as a function of frequency and phase bin using the PDV software package. The RM values as a function of phase bin were determined using RM-synthesis (Burn, 1966; Brentjens and de Bruyn, 2005) as implemented in the RMTOOLKIT[14] with the RM CLEAN deconvolution procedure (Heald et al., 2009).

For search mode, the data were first processed with `DSPSR`[15] software package in order to extract each individual pulse (using the -b, -K, -A and -scloffs options). The output single pulses had 512 phase bins. The resulting single pulses data were then processed in the same manner as the fold mode observations.

4.3 Results

4.3.1 Wideband averaged profile of the bright state

In Figure 23, we show the bright-state time-averaged profile for PSR J1107−5907 as a function of different observing frequencies. Each row in the figure corresponds to a different band (equally spaced into eight 416 MHz-wide frequency bands across the entire bandwidth). In the second column of Figure 23, it is clear that there is emission before and after the main pulse component. Hereafter, we refer to those components as the precursor and postcursor components respectively.

The total intensity pulse profile varies significantly as a function of observing frequency. Columns 2 and 3 in Table 9 lists the pulse width as a function of frequency and the averaged flux density respectively. These values were obtained using the `pdv` command with `-f, -x` option of the `PSRCHIVE`. For each phase bin we have determined the spectral index using a simple power-law of the form (this assumes no phase shifts as a function of observing frequency for the pulse components):

$$P(f) = A\left(\frac{f}{f_c}\right)^{\alpha}, \tag{76}$$

where P is the flux density, f is the observing frequency, f_c is the centre of our observing band ($f_c =$ 2368 MHz), and α is the spectral index. In the left-panel of Figure 24 we show the pulse profile (top panel) with the precursor, main and postcursor regions highlighted. In the middle panel we show the spectral index as measured using the 16 sub-bands for each phase bin. The spectral index was measured using the `curve_fit`[16] method of `scipy.optimize`, a python package which determine parameters using non-linear least squares to fit a function. The top of the right-hand panel shows the average flux density (and hence the averaged spectral indices) for the various components of the profile. The spectral index for each of the main profile components are -1.41 ± 0.01 for the main component, -2.00 ± 0.01 for the precursor, -1.66 ± 0.01 for the postcursor, and -1.49 ± 0.01 for the entire profile. These results differ slightly from the results of

[13] https://github.com/csobey/ionFR
[14] https://github.com/gheald/RMtoolkit
[15] https://dspsr.sourceforge.net
[16] https://docs.scipy.org/doc/scipy/reference/generated/scipy.optimize.curve_fit.html

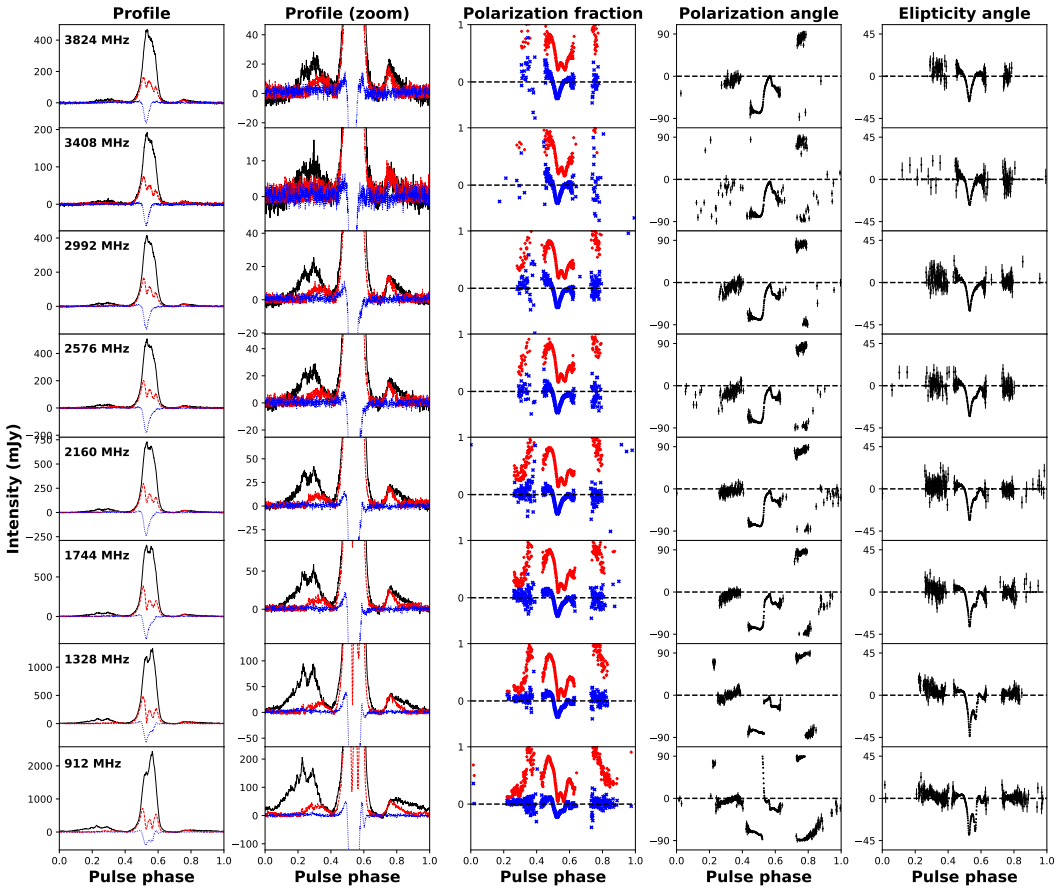

Figure 23: Wideband, time-averaged, polarisation profile of PSR J1107−5907. 3328 channels are divided into 8 sub-bands. The first column: pulse profile corresponding to each frequency band. In each panel, the center frequency is displayed at upper left of the profile plot. The black, red and blue lines are the total intensity, linear polarisation, and circular polarisation, respectively. The second column: pulse profile, but now zoomed in to around baseline. The third column: polarisation fraction where the red plus and blue cross points are linear L/I and circular polarisation V/I. The fourth column: polarisation angle $\mathrm{PA} = \tan^{-1}(U/Q)$. The last column: ellipticity angle $\mathrm{EA} = 0.5\tan^{-1}(V/\sqrt{Q^2+U^2})$.

Table 9: Wideband emission properties of PSR J1107−5907. The columns are as follows: (1) Pulse profile width at 50% of the peak amplitude (2) Center frequency of the sub-band. (3) Mean flux density. (4) Lenear polarisation fraction. (5) Circular polarisation fraction. (6) Absolute value of circular polarisation fraction..

frequency (MHz)	W_{50} (ms)	S (mJy)	L/I %	V/I %	$\|V\|/I$ %
808	85.6	298	17.4	−0.421	7.02
1016	89.9	216	16.3	−1.31	7.41
1224	87.1	197	16.2	0.054	7.85
1432	89.4	117	17.0	−0.23	8.06
1640	90.7	108	19.8	−1.12	8.43
1848	90.1	86.7	21.0	−0.641	9.78
2056	88.7	62.5	22.3	−1.07	9.96
2264	88.5	89.9	23.0	−0.454	9.30
2472	85.9	50.5	25.2	−1.78	12.2
2680	86.0	51.4	23.6	−2.01	12.4
2888	85.8	41.4	23.8	0.400	10.8
3096	85.4	43.2	24.4	0.362	9.13
3304	85.2	24.6	26.4	3.18	10.2
3512	83.0	11.8	30.9	−5.55	15.9
3720	84.9	48.9	28.2	3.46	9.85
3928	84.0	48.3	28.6	3.48	9.82

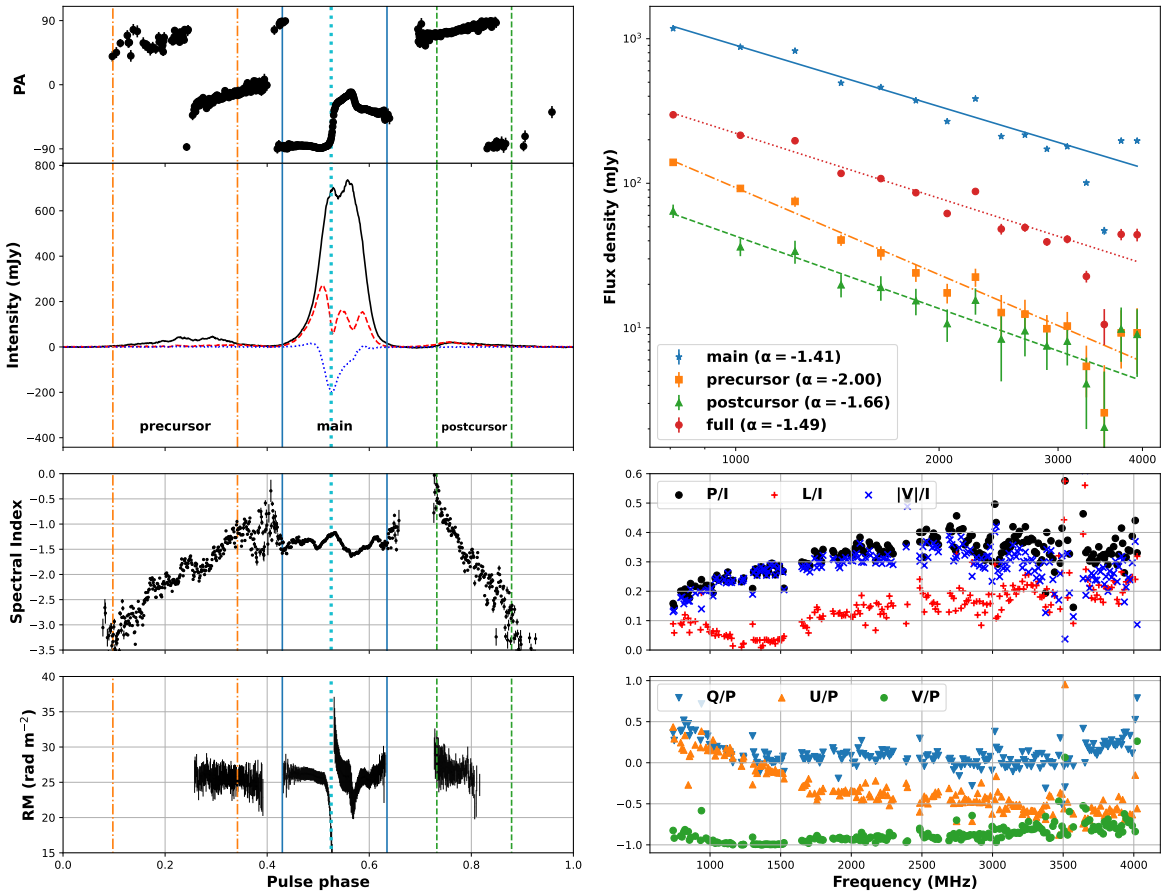

Figure 24: Phase-resolved emission properties of PSR J1107-5907. Left top: time and frequency averaged polarisation profile and polarisation angle. The meaning of line colors are the same as in Figure 23. Left middle: phase-resolved spectral indices. Left bottom: phase-resolved RM. Right top: mean flux densities for each pulse components as a function of frequency. The solid, dot dashed, dashed, and dots line are the best fit line of the main, precursor, postcursor components, and full pulse window, respectively. Right middle: polarisation fraction of the phase that has highest circular polarisation intensity (expressed as the cyan-dotted line on the left plot). Black circle, red plus, blue cross points are the total polarisation fraction $P/I = \sqrt{Q^2+U^2+V^2}/I$, linear polarisation fraction L/I, and circular polarisation fraction V/I, respectively. Right bottom : polarisation spectra of the same pulse phase. Blue down triangles, orange up triangles, and green circles are Q/P, U/P, and V/P, respectively. Faraday rotation effect is corrected using $\mathrm{RM} = 21.29\,\mathrm{rad/m^{-2}}$

(Meyers et al., 2018), but are consistent with (Wang et al., 2020).

The phased-averaged polarisation fractions as a function of observing frequency are listed in columns 4, 5 and 6 of Table 9 and the phase-averaged RMs in Table 8. In the top-left panel of Figure 24 we show the polarisation angle of the linear polarisation as a function of pulse phase for the averaged pulse profile and averaged over the entire observing band. The panel below shows the averaged pulse profile total intensity (black), linear polarisation (red) and circular polarisation (blue). The bottom-left panel shows the RM as a function of pulse phase. The RM was measured by applying RM-synthesis as implemented in the RM-TOOLKIT to polarization spectra for each phase bins. We can see that RM significantly dependent of pulse phase. There are several studies measuring phase-resolved RM (Noutsos et al., 2009; Dai et al., 2015; Ilie et al., 2019). Noutsos et al. (2009) proposed that for those observed large RM changes, if the Stokes V fraction V/I has a frequency dependence, this is an effect of the pulsar magnetosphere. On the other hand, Ilie et al. (2019) argued that interstellar scattering also causes phase-resolved RM and V/I variation. They showed that a method to distinguish this is that in the case of scattering, the RM variation occurs at the phase where the Stokes V is changing most rapidly. The phase where the RM jump occurs (around 0.53) aligns with the phase where the polarisation-angle curve is steepest. and the circular polarisation intensity is highest. The polarisation fraction and spectra of the phase are shown in the right middle and bottom panel of Figure 24. We can see that both circular and linear polarization varies with frequency, implying that the RM variation is originate from the pulsar magnetosphere.

4.3.2 Wideband single pulse analysis

In the observation taken on August 30 2022, we were able to detect the bright emission of PSR J1107−5907 with high time resolution, which allows us to detect and study almost 500 individual pulses. The detection threshold was more than 5σ. Figure 25 shows the flux density and spectral indices measured using the power-law model from equation (76). Single pulses are clearly detected at each frequency. Figure 26 shows the spectral index distribution of single pulses. The mean spectral index is -1.45 with a standard deviation of 0.83.

Figure 27 shows waterfall plots for eight single pulses, many of which do not resemble the averaged profile. The 651st pulse is sharper and more polarised than the averaged profile and has a very high circular polarisation fraction. The 674th pulse also has a very high circular polarisation fraction, and the pulse appear to be broadened in width at lower frequencies. The 362 pulse also has high circular polarisation fraction but in opposite sign and its polarisation angle has complicated structure. The 279th pulse has a very large number of components, and the 775th pulse has a shape that could be called a twin pulse in its frequency averaged profile although spectral features are quit different. In addition, the main pulse shows almost 100% polarisation fraction. In the 279th and 775th pulses, the main component has emission at all frequencies, whereas the precursor component has a steep spectral index. The 306th pulse has brighter precursor component than the main component. The 307th pulse that follows shows several sub-pulses in the precursor, postcursor components as well as the main component.

Figure 28 presents the RM corrected polarisation angle and ellipticity angle distribution for each sub-bands. For each panel, the top, middle, bottom plots provides the averaged profile of single pulses, polarisation angle

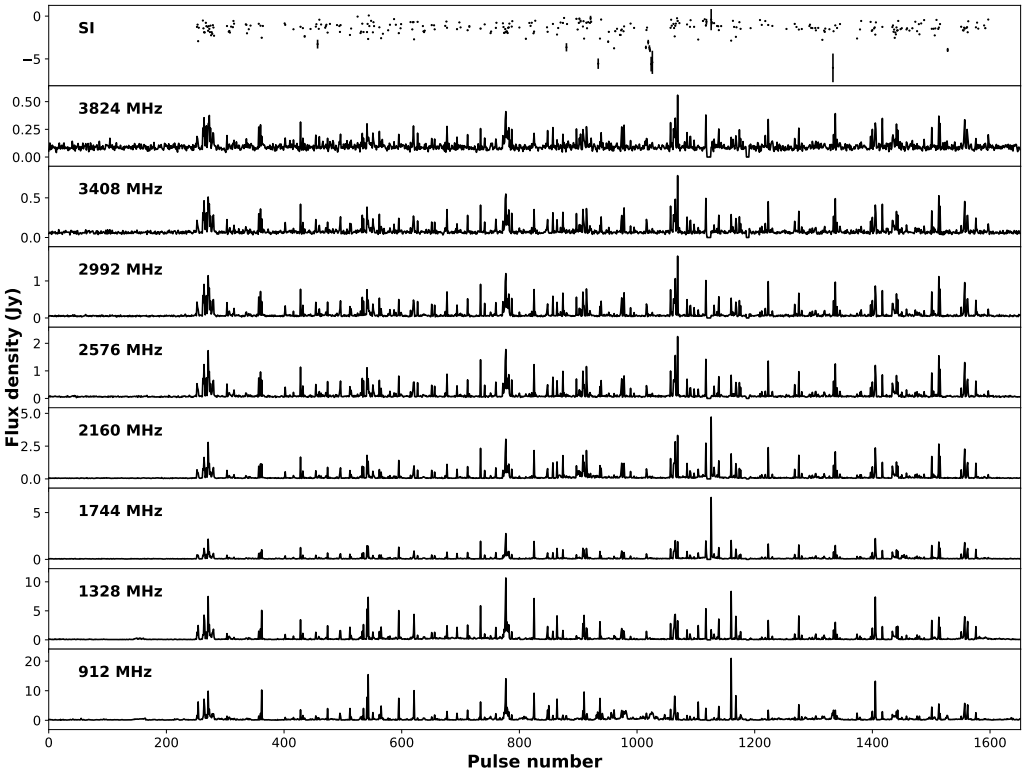

Figure 25: Mean flux density and spectral index of each single pulses. The spectral indices were calculated if there are more than three channels which is greater than 8σ.

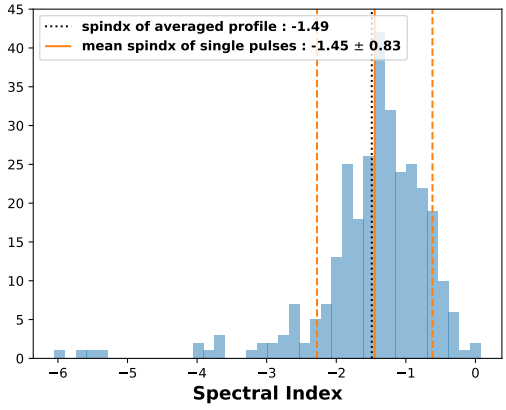

Figure 26: The spectral index distribution of single pulses. The distribution is expressed as blue histogram. The black dots and orange solid lines are the spectral index of the averaged profile (see the right panel of Figure 24) and the mean spectral index of single pulses, respectively. Orange dashed lines are represents 1σ region of the mean spectral index.

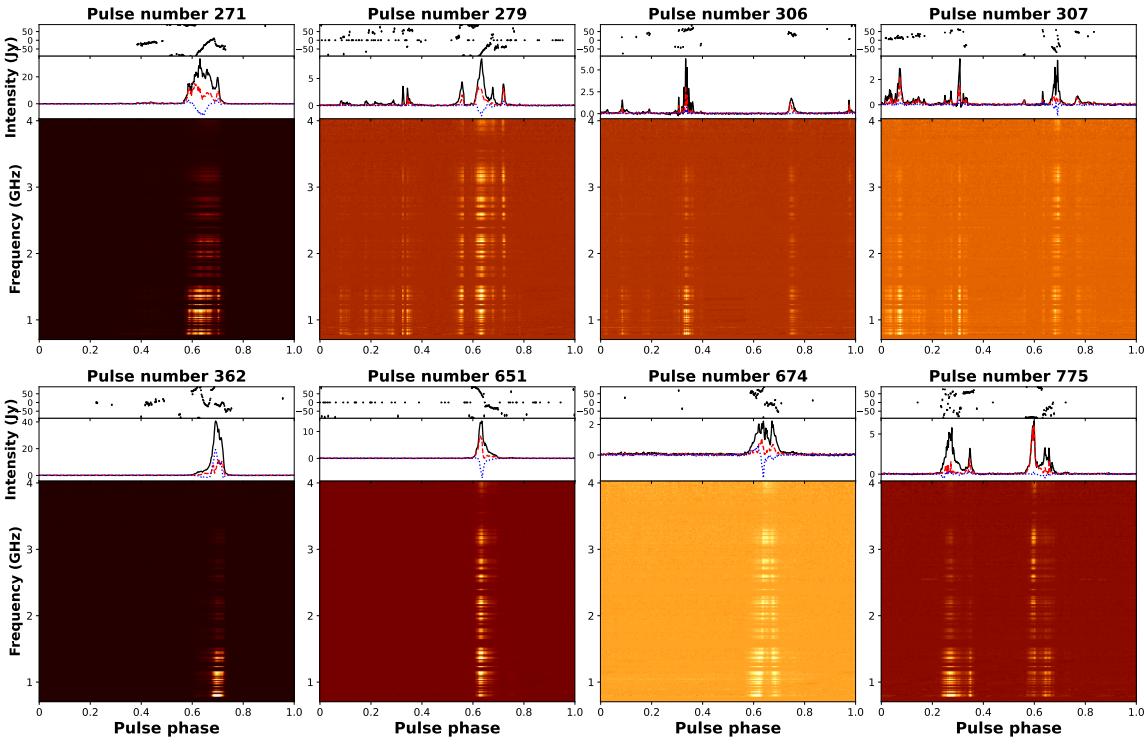

Figure 27: Some examples of single pulses. top: polarisation angle. middle: frequency averaged, single pulse profile (Jy). bottom: waterfall plot. Corresponding pulse numbers are listed on each figures.

distribution, and ellipticity angle distribution, respectively. As reported by Young et al. (2014) orthogonally polarised modes (OPM) are seen in precursor and postcursor region and non-OPM like structure are seen in the main component as well. Our observations confirm these modes exist across the entire wide bandwidth. In the main component, we see the elipticity angle tend to be negative as expected from the averaged profile. In Figure 29, we show phase-resolved modulation indices and peak position distribution for each observing frequencies. Modulation index is a measure of variability defined as the standard deviation of the flux densities divided by the mean. However, we calculated it using phase-resolved fluctuation spectra (often called as longitude-resolved fluctuation spectra, LRFS). The modulation indices were obtained using the `PSRSALSA`[17] software package (Weltevrede, 2016). The uncertainties on the modulation indices were determined using a bootstrap method with 100 realization. For each panel, blue circles represents modulation indices and black lines are peak position distribution. The modulation indices are plotted when the average intensity of the phase is more than 3σ.

4.4 Discussion and conclusion

In its bright state we can detect individual pulses from PSR J1107−5907 over the entire bandwidth of our UWL receiver. In many cases the individual pulses exhibit emission across a wide range of pulse phases (for examples pulse numbers 279 and 775 in Figure 27). As reported in Young et al. (2014), this pulsar is likely

[17] https://github.com/weltevrede/psrsalsa

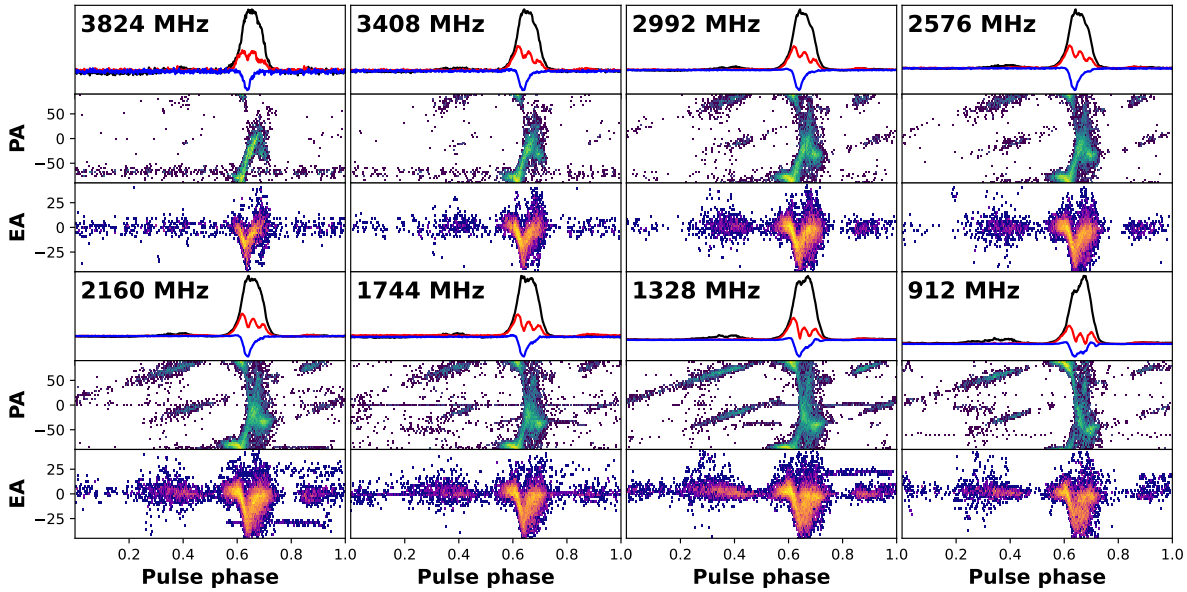

Figure 28: RM corrected polarisation angle and ellipticity angle distribution of single pulses. top: averaged profile of all single pulses. middle: polarisation angle distribution. bottom: ellipticity angle distribution. Colors of each point indicate number density. The polarization angle and elipticity angle are plotted if the linear polarization intensity is more than 5σ.

a nearly-aligned rotator, implying that we are seeing emission over a wide pulse phase from a single polar cap.

As noted by Wang et al. (2020) the scintillation bandwidth is ∼73 MHz around an observing frequency 1400 MHz and PSR J1107−5907 has relatively long scintillation timescales (modelled as ∼ 5 minutes by Young et al. (2014), and measured to be >24 minutes by Wang et al. (2020)). These frequency and time scales are different from those probed by our data and hence scintillation phenomena are unlikely to be dominating the results presented here.

The "bursty" pulse properties that we observe from PSR J1107−5907 are similar to that seen from single pulses in magnetars (Lower et al., 2021; Giri et al., 2023) and RRATs (Sun et al., 2023). A possible commonality is that PSR J1107−5907 is a nearly-aligned rotator (Young et al., 2014) . Figure 29 shows the modulation index for the single pulse intensities in different observing bands. The results are consistent with those shown in Young et al. (2014) in the 20 and 10 cm bands. There is no significant evolution of the modulation index as a function of frequency. However, the absolute value of the modulation index is decreasing as the observing frequency increases.

Can we make a link between the bright state of PSR J1107−5907 and fast radio burst (FRB) emission? There are similarities. For instance, pulse 674 in Figure 27 shows a frequency structure similar to that seen in some FRBs (Chime/Frb Collaboration et al., 2023; Giri et al., 2023) and we have noted links between the emission seen here and from magnetars, which may be the progenitor of some FRBs. One FRB model is that the progenitor source is an aligned rotator (see, e.g, Petroff et al. (2019)). However, the range of different pulse shapes seen in the single pulse data means that it is hard to make a definite statement on any potential

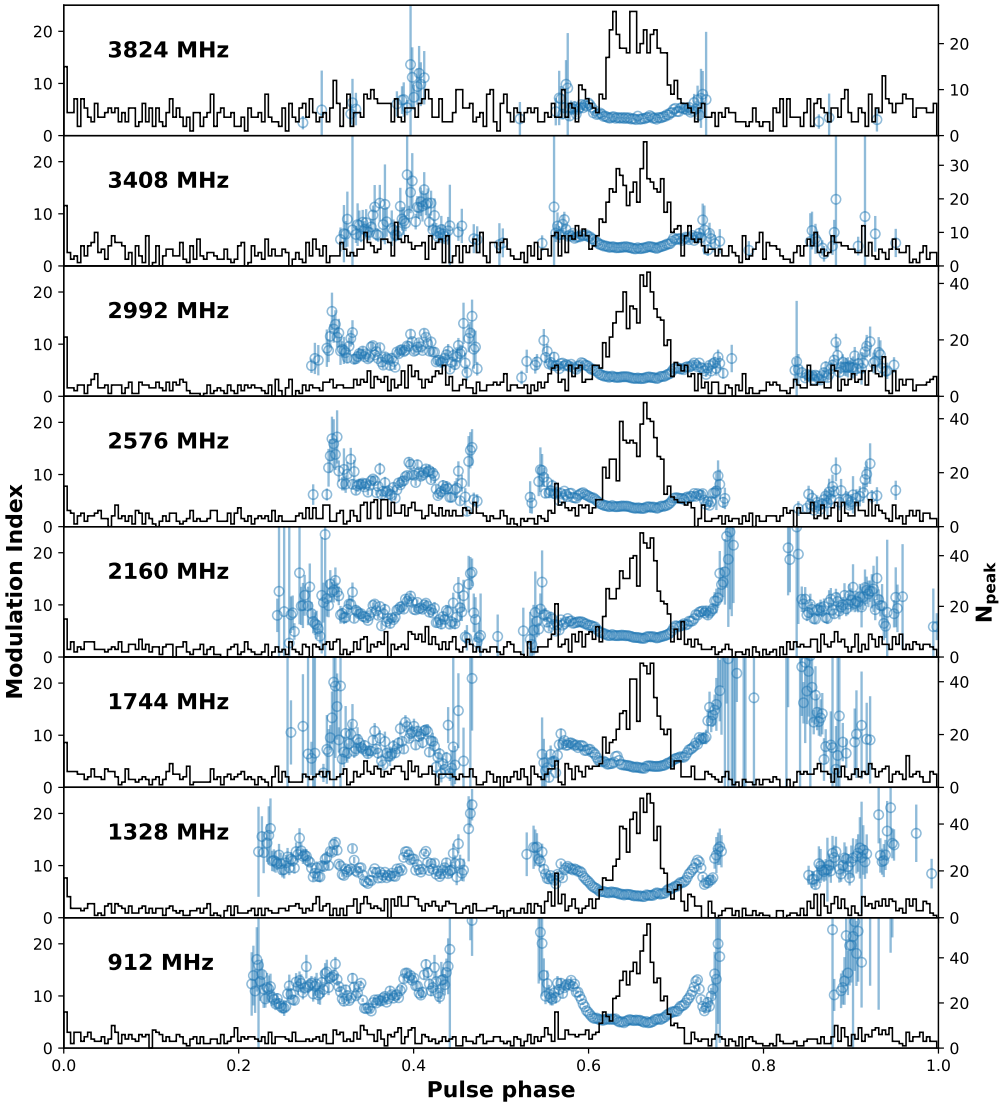

Figure 29: Phase-resolved modulation indices and peak distribution of single pulses. Blue circles represent phase-resolved modulation indices with the scale represented by the left y-axis. The black lines show the peak phase distribution of the single pulses scaled using the right y-axis.

links.

Figure 28 shows the distribution of the polarisation angle as a function of pulse phase for the individual pulses. Away from the main profile component we see two parallel lines indicating two orthogonal emission modes and hence the emission is switching between two orthogonal modes. The PA variation occurring in the main component is expected as suggests in Dyks (2020). This is unlikely to be caused by Faraday conversion as the total linear polarisation fraction as a fraction of frequency decreases at lower frequencies as shown in the bottom right panel of Figure 24 (Melrose and Stoneham, 1977; Petrova, 2001; Lower, 2021; Lower et al., 2023). Instead this is more likely caused by fully, or partial, mixing of linear polarisation modes (Dyks, 2019; Oswald et al., 2023).

Our third observation was recorded simultaneously in high time-resolution mode and by folding the pulsar signal online. This allows a consistency check on the calibration procedures. When we sum together our calibrated single pulses we do recover the flux density and polarisation properties of the folded profile as a function of observing frequency.

The single pulses that we have detected contain a wealth of information on the emission process. In order to develop this work we require further monitoring (with high time resolution) of this pulsar. This is a challenge because the time spent in the bright state is relatively short. Detecting higher energy emission (such as X-ray emission) during a bright state would also provide information on the surface properties of the neutron star during this emission state.

Acknowledgements

I have been greatly supported by lots of people to get a Ph.D. I have worked in a blessed environment. First, I would like to express my deepest appreciation to my supervisor, Professor Keitaro Takahashi. I couldn't have accomplished my studies without his greatly support and instruction. He has always been willing to guide and gave me numerous opportunities such as to attend conferences, study abroad and discuss with other professional in different countries.

I have been greatly supported by people working at Australia Telescope National Facility, CSIRO in Australia as well when I visited and stayed there. I have special thanks for my co-supervisor Dr. George Hobbs. He worked and discussed with me as much as possible even thought my ability in English is poor. I couldn't have finished to write the paper discribed in Section 4 without his tremendous help. I also have thanks for Dr. Marcus Lower, Dr. Shi Dai, Dr. Andrew Zic, Dr. Robert Hollow, Dr. Simon Johnston, Dr. Rui Luo, Mr. Saurav Mishra, Ms. Leanne Edwards, and all the staff worked at the Parkes observatory.

I have been also supported by the Indian Pulsar Timing Array collaboration. I have studied with them throughout my Ph.D. program and have learned about data analysis methods and Indian culture from them. The biweekly meetings with them have greatly helped to improve my English skill. They also entrusted me with a jitter analysis project in Section 3, which is a very interesting topic. Their cooperation was also essential for my doctoral thesis.

It was great that I have been attached to the cosmology group in Kumamoto University. I have had wonderful colleagues. Especially pulsar group members, Dr. Naoyuki Yonemaru, Dr. Hiroki Kumamoto, Dr. Ryo Kato, Dr. Shinnosuke Hisano, Takuro Hachiya, and Toki Ogi have help me a lot through fruitful discussion. In addition, Yuta Shiohira and Akira Kuchinomachi have been in the same grade and shared the joys and sorrows with me. They made my student life lively. Thanks to all of them. I could spend an enjoyable university life.

Finally and most importantly, thank you to my family and Kyomi Uchino for their understanding on my decision to go Ph.D. course and financial support.

Bibliography

B. P. Abbott, R. Abbott, T. D. Abbott, M. R. Abernathy, F. Acernese, K. Ackley, C. Adams, T. Adams, P. Addesso, R. X. Adhikari, V. B. Adya, C. Affeldt, M. Agathos, K. Agatsuma, N. Aggarwal, O. D. Aguiar, L. Aiello, A. Ain, P. Ajith, B. Allen, A. Allocca, P. A. Altin, S. B. Anderson, W. G. Anderson, K. Arai, M. A. Arain, M. C. Araya, C. C. Arceneaux, J. S. Areeda, N. Arnaud, K. G. Arun, S. Ascenzi, G. Ashton, M. Ast, S. M. Aston, P. Astone, P. Aufmuth, C. Aulbert, S. Babak, P. Bacon, M. K. M. Bader, P. T. Baker, F. Baldaccini, G. Ballardin, S. W. Ballmer, J. C. Barayoga, S. E. Barclay, B. C. Barish, D. Barker, F. Barone, B. Barr, L. Barsotti, M. Barsuglia, D. Barta, J. Bartlett, M. A. Barton, I. Bartos, R. Bassiri, A. Basti, J. C. Batch, C. Baune, V. Bavigadda, M. Bazzan, B. Behnke, M. Bejger, C. Belczynski, A. S. Bell, C. J. Bell, B. K. Berger, J. Bergman, G. Bergmann, C. P. L. Berry, D. Bersanetti, A. Bertolini, J. Betzwieser, S. Bhagwat, R. Bhandare, I. A. Bilenko, G. Billingsley, J. Birch, R. Birney, O. Birnholtz, S. Biscans, A. Bisht, M. Bitossi, C. Biwer, M. A. Bizouard, J. K. Blackburn, C. D. Blair, D. G. Blair, R. M. Blair, S. Bloemen, O. Bock, T. P. Bodiya, M. Boer, G. Bogaert, C. Bogan, A. Bohe, P. Bojtos, C. Bond, F. Bondu, R. Bonnand, B. A. Boom, R. Bork, V. Boschi, S. Bose, Y. Bouffanais, A. Bozzi, C. Bradaschia, P. R. Brady, V. B. Braginsky, M. Branchesi, J. E. Brau, T. Briant, A. Brillet, M. Brinkmann, V. Brisson, P. Brockill, A. F. Brooks, D. A. Brown, D. D. Brown, N. M. Brown, C. C. Buchanan, A. Buikema, T. Bulik, H. J. Bulten, A. Buonanno, D. Buskulic, C. Buy, R. L. Byer, M. Cabero, L. Cadonati, G. Cagnoli, C. Cahillane, J. C. Bustillo, T. Callister, E. Calloni, J. B. Camp, K. C. Cannon, J. Cao, C. D. Capano, E. Capocasa, F. Carbognani, S. Caride, J. C. Diaz, C. Casentini, S. Caudill, M. Cavaglià, F. Cavalier, R. Cavalieri, G. Cella, C. B. Cepeda, L. C. Baiardi, G. Cerretani, E. Cesarini, R. Chakraborty, T. Chalermsongsak, S. J. Chamberlin, M. Chan, S. Chao, P. Charlton, E. Chassande-Mottin, H. Y. Chen, Y. Chen, C. Cheng, A. Chincarini, A. Chiummo, H. S. Cho, M. Cho, J. H. Chow, N. Christensen, Q. Chu, S. Chua, S. Chung, G. Ciani, F. Clara, J. A. Clark, F. Cleva, E. Coccia, P.-F. Cohadon, A. Colla, C. G. Collette, L. Cominsky, M. Constancio, A. Conte, L. Conti, D. Cook, T. R. Corbitt, N. Cornish, A. Corsi, S. Cortese, C. A. Costa, M. W. Coughlin, S. B. Coughlin, J.-P. Coulon, S. T. Countryman, P. Couvares, E. E. Cowan, D. M. Coward, M. J. Cowart, D. C. Coyne, R. Coyne, K. Craig, J. D. E. Creighton, T. D. Creighton, J. Cripe, S. G. Crowder, A. M. Cruise, A. Cumming, L. Cunningham, E. Cuoco, T. D. Canton, S. L. Danilishin, S. D'Antonio, K. Danzmann, N. S. Darman, C. F. Da Silva Costa, V. Dattilo, I. Dave, H. P. Daveloza, M. Davier, G. S. Davies, E. J. Daw, R. Day, S. De, D. DeBra, G. Debreczeni, J. Degallaix, M. De Laurentis, S. Deléglise, W. Del Pozzo, T. Denker, T. Dent, H. Dereli, V. Dergachev, R. T. DeRosa, R. De Rosa, R. DeSalvo, S. Dhurandhar, M. C. D´iaz, L. Di Fiore, M. Di Giovanni, A. Di Lieto, S. Di Pace, I. Di Palma, A. Di Virgilio, G. Dojcinoski, V. Dolique, F. Donovan, K. L. Dooley, S. Doravari, R. Douglas, T. P. Downes, M. Drago, R. W. P. Drever, J. C. Driggers, Z. Du, M. Ducrot, S. E. Dwyer, T. B. Edo, M. C. Edwards, A. Effler, H.-B. Eggenstein, P. Ehrens, J. Eichholz, S. S. Eikenberry, W. Engels, R. C. Essick, T. Etzel, M. Evans, T. M. Evans, R. Everett, M. Factourovich, V. Fafone, H. Fair, S. Fairhurst, X. Fan, Q. Fang, S. Farinon, B. Farr, W. M. Farr, M. Favata, M. Fays, H. Fehrmann, M. M. Fejer, D. Feldbaum, I. Ferrante, E. C. Ferreira, F. Ferrini, F. Fidecaro, L. S. Finn, I. Fiori, D. Fiorucci, R. P. Fisher, R. Flaminio, M. Fletcher, H. Fong, J.-D. Fournier, S. Franco, S. Frasca, F. Frasconi, M. Frede, Z. Frei, A. Freise, R. Frey, V. Frey, T. T. Fricke, P. Fritschel, V. V. Frolov, P. Fulda, M. Fyffe, H. A. G. Gabbard, J. R. Gair, L. Gammaitoni,

S. G. Gaonkar, F. Garufi, A. Gatto, G. Gaur, N. Gehrels, G. Gemme, B. Gendre, E. Genin, A. Gennai, J. George, L. Gergely, V. Germain, A. Ghosh, A. Ghosh, S. Ghosh, J. A. Giaime, K. D. Giardina, A. Giazotto, K. Gill, A. Glaefke, J. R. Gleason, E. Goetz, R. Goetz, L. Gondan, G. González, J. M. G. Castro, A. Gopakumar, N. A. Gordon, M. L. Gorodetsky, S. E. Gossan, M. Gosselin, R. Gouaty, C. Graef, P. B. Graff, M. Granata, A. Grant, S. Gras, C. Gray, G. Greco, A. C. Green, R. J. S. Greenhalgh, P. Groot, H. Grote, S. Grunewald, G. M. Guidi, X. Guo, A. Gupta, M. K. Gupta, K. E. Gushwa, E. K. Gustafson, R. Gustafson, J. J. Hacker, B. R. Hall, E. D. Hall, G. Hammond, M. Haney, M. M. Hanke, J. Hanks, C. Hanna, M. D. Hannam, J. Hanson, T. Hardwick, J. Harms, G. M. Harry, I. W. Harry, M. J. Hart, M. T. Hartman, C.-J. Haster, K. Haughian, J. Healy, J. Heefner, A. Heidmann, M. C. Heintze, G. Heinzel, H. Heitmann, P. Hello, G. Hemming, M. Hendry, I. S. Heng, J. Hennig, A. W. Heptonstall, M. Heurs, S. Hild, D. Hoak, K. A. Hodge, D. Hofman, S. E. Hollitt, K. Holt, D. E. Holz, P. Hopkins, D. J. Hosken, J. Hough, E. A. Houston, E. J. Howell, Y. M. Hu, S. Huang, E. A. Huerta, D. Huet, B. Hughey, S. Husa, S. H. Huttner, T. Huynh-Dinh, A. Idrisy, N. Indik, D. R. Ingram, R. Inta, H. N. Isa, J.-M. Isac, M. Isi, G. Islas, T. Isogai, B. R. Iyer, K. Izumi, M. B. Jacobson, T. Jacqmin, H. Jang, K. Jani, P. Jaranowski, S. Jawahar, F. Jiménez-Forteza, W. W. Johnson, N. K. Johnson-McDaniel, D. I. Jones, R. Jones, R. J. G. Jonker, L. Ju, K. Haris, C. V. Kalaghatgi, V. Kalogera, S. Kandhasamy, G. Kang, J. B. Kanner, S. Karki, M. Kasprzack, E. Katsavounidis, W. Katzman, S. Kaufer, T. Kaur, K. Kawabe, F. Kawazoe, F. Kéfélian, M. S. Kehl, D. Keitel, D. B. Kelley, W. Kells, R. Kennedy, D. G. Keppel, J. S. Key, A. Khalaidovski, F. Y. Khalili, I. Khan, S. Khan, Z. Khan, E. A. Khazanov, N. Kijbunchoo, C. Kim, J. Kim, K. Kim, N.-G. Kim, N. Kim, Y.-M. Kim, E. J. King, P. J. King, D. L. Kinzel, J. S. Kissel, L. Kleybolte, S. Klimenko, S. M. Koehlenbeck, K. Kokeyama, S. Koley, V. Kondrashov, A. Kontos, S. Koranda, M. Korobko, W. Z. Korth, I. Kowalska, D. B. Kozak, V. Kringel, B. Krishnan, A. Królak, C. Krueger, G. Kuehn, P. Kumar, R. Kumar, L. Kuo, A. Kutynia, P. Kwee, B. D. Lackey, M. Landry, J. Lange, B. Lantz, P. D. Lasky, A. Lazzarini, C. Lazzaro, P. Leaci, S. Leavey, E. O. Lebigot, C. H. Lee, H. K. Lee, H. M. Lee, K. Lee, A. Lenon, M. Leonardi, J. R. Leong, N. Leroy, N. Letendre, Y. Levin, B. M. Levine, T. G. F. Li, A. Libson, T. B. Littenberg, N. A. Lockerbie, J. Logue, A. L. Lombardi, L. T. London, J. E. Lord, M. Lorenzini, V. Loriette, M. Lormand, G. Losurdo, J. D. Lough, C. O. Lousto, G. Lovelace, H. Lück, A. P. Lundgren, J. Luo, R. Lynch, Y. Ma, T. MacDonald, B. Machenschalk, M. MacInnis, D. M. Macleod, F. Magaña Sandoval, R. M. Magee, M. Mageswaran, E. Majorana, I. Maksimovic, V. Malvezzi, N. Man, I. Mandel, V. Mandic, V. Mangano, G. L. Mansell, M. Manske, M. Mantovani, F. Marchesoni, F. Marion, S. Márka, Z. Márka, A. S. Markosyan, E. Maros, F. Martelli, L. Martellini, I. W. Martin, R. M. Martin, D. V. Martynov, J. N. Marx, K. Mason, A. Masserot, T. J. Massinger, M. Masso-Reid, F. Matichard, L. Matone, N. Mavalvala, N. Mazumder, G. Mazzolo, R. McCarthy, D. E. McClelland, S. McCormick, S. C. McGuire, G. McIntyre, J. McIver, D. J. McManus, S. T. McWilliams, D. Meacher, G. D. Meadors, J. Meidam, A. Melatos, G. Mendell, D. Mendoza-Gandara, R. A. Mercer, E. Merilh, M. Merzougui, S. Meshkov, C. Messenger, C. Messick, P. M. Meyers, F. Mezzani, H. Miao, C. Michel, H. Middleton, E. E. Mikhailov, L. Milano, J. Miller, M. Millhouse, Y. Minenkov, J. Ming, S. Mirshekari, C. Mishra, S. Mitra, V. P. Mitrofanov, G. Mitselmakher, R. Mittleman, A. Moggi, M. Mohan, S. R. P. Mohapatra, M. Montani, B. C. Moore, C. J. Moore, D. Moraru, G. Moreno, S. R. Morriss, K. Mossavi, B. Mours, C. M. Mow-Lowry, C. L.

Mueller, G. Mueller, A. W. Muir, A. Mukherjee, D. Mukherjee, S. Mukherjee, N. Mukund, A. Mullavey, J. Munch, D. J. Murphy, P. G. Murray, A. Mytidis, I. Nardecchia, L. Naticchioni, R. K. Nayak, V. Necula, K. Nedkova, G. Nelemans, M. Neri, A. Neunzert, G. Newton, T. T. Nguyen, A. B. Nielsen, S. Nissanke, A. Nitz, F. Nocera, D. Nolting, M. E. N. Normandin, L. K. Nuttall, J. Oberling, E. Ochsner, J. O'Dell, E. Oelker, G. H. Ogin, J. J. Oh, S. H. Oh, F. Ohme, M. Oliver, P. Oppermann, R. J. Oram, B. O'Reilly, R. O'Shaughnessy, C. D. Ott, D. J. Ottaway, R. S. Ottens, H. Overmier, B. J. Owen, A. Pai, S. A. Pai, J. R. Palamos, O. Palashov, C. Palomba, A. Pal-Singh, H. Pan, Y. Pan, C. Pankow, F. Pannarale, B. C. Pant, F. Paoletti, A. Paoli, M. A. Papa, H. R. Paris, W. Parker, D. Pascucci, A. Pasqualetti, R. Passaquieti, D. Passuello, B. Patricelli, Z. Patrick, B. L. Pearlstone, M. Pedraza, R. Pedurand, L. Pekowsky, A. Pele, S. Penn, A. Perreca, H. P. Pfeiffer, M. Phelps, O. Piccinni, M. Pichot, M. Pickenpack, F. Piergiovanni, V. Pierro, G. Pillant, L. Pinard, I. M. Pinto, M. Pitkin, J. H. Poeld, R. Poggiani, P. Popolizio, A. Post, J. Powell, J. Prasad, V. Predoi, S. S. Premachandra, T. Prestegard, L. R. Price, M. Prijatelj, M. Principe, S. Privitera, R. Prix, G. A. Prodi, L. Prokhorov, O. Puncken, M. Punturo, P. Puppo, M. Pürrer, H. Qi, J. Qin, V. Quetschke, E. A. Quintero, R. Quitzow-James, F. J. Raab, D. S. Rabeling, H. Radkins, P. Raffai, S. Raja, M. Rakhmanov, C. R. Ramet, P. Rapagnani, V. Raymond, M. Razzano, V. Re, J. Read, C. M. Reed, T. Regimbau, L. Rei, S. Reid, D. H. Reitze, H. Rew, S. D. Reyes, F. Ricci, K. Riles, N. A. Robertson, R. Robie, F. Robinet, A. Rocchi, L. Rolland, J. G. Rollins, V. J. Roma, J. D. Romano, R. Romano, G. Romanov, J. H. Romie, D. Rosińska, S. Rowan, A. Rüdiger, P. Ruggi, K. Ryan, S. Sachdev, T. Sadecki, L. Sadeghian, L. Salconi, M. Saleem, F. Salemi, A. Samajdar, L. Sammut, L. M. Sampson, E. J. Sanchez, V. Sandberg, B. Sandeen, G. H. Sanders, J. R. Sanders, B. Sassolas, B. S. Sathyaprakash, P. R. Saulson, O. Sauter, R. L. Savage, A. Sawadsky, P. Schale, R. Schilling, J. Schmidt, P. Schmidt, R. Schnabel, R. M. S. Schofield, A. Schönbeck, E. Schreiber, D. Schuette, B. F. Schutz, J. Scott, S. M. Scott, D. Sellers, A. S. Sengupta, D. Sentenac, V. Sequino, A. Sergeev, G. Serna, Y. Setyawati, A. Sevigny, D. A. Shaddock, T. Shaffer, S. Shah, M. S. Shahriar, M. Shaltev, Z. Shao, B. Shapiro, P. Shawhan, A. Sheperd, D. H. Shoemaker, D. M. Shoemaker, K. Siellez, X. Siemens, D. Sigg, A. D. Silva, D. Simakov, A. Singer, L. P. Singer, A. Singh, R. Singh, A. Singhal, A. M. Sintes, B. J. J. Slagmolen, J. R. Smith, M. R. Smith, N. D. Smith, R. J. E. Smith, E. J. Son, B. Sorazu, F. Sorrentino, T. Souradeep, A. K. Srivastava, A. Staley, M. Steinke, J. Steinlechner, S. Steinlechner, D. Steinmeyer, B. C. Stephens, S. P. Stevenson, R. Stone, K. A. Strain, N. Straniero, G. Stratta, N. A. Strauss, S. Strigin, R. Sturani, A. L. Stuver, T. Z. Summerscales, L. Sun, P. J. Sutton, B. L. Swinkels, M. J. Szczepańczyk, M. Tacca, D. Talukder, D. B. Tanner, M. Tápai, S. P. Tarabrin, A. Taracchini, R. Taylor, T. Theeg, M. P. Thirugnanasambandam, E. G. Thomas, M. Thomas, P. Thomas, K. A. Thorne, K. S. Thorne, E. Thrane, S. Tiwari, V. Tiwari, K. V. Tokmakov, C. Tomlinson, M. Tonelli, C. V. Torres, C. I. Torrie, D. Töyrä, F. Travasso, G. Traylor, D. Trifirò, M. C. Tringali, L. Trozzo, M. Tse, M. Turconi, D. Tuyenbayev, D. Ugolini, C. S. Unnikrishnan, A. L. Urban, S. A. Usman, H. Vahlbruch, G. Vajente, G. Valdes, M. Vallisneri, N. van Bakel, M. van Beuzekom, J. F. J. van den Brand, C. Van Den Broeck, D. C. Vander-Hyde, L. van der Schaaf, J. V. van Heijningen, A. A. van Veggel, M. Vardaro, S. Vass, M. Vasúth, R. Vaulin, A. Vecchio, G. Vedovato, J. Veitch, P. J. Veitch, K. Venkateswara, D. Verkindt, F. Vetrano, A. Viceré, S. Vinciguerra, D. J. Vine, J.-Y. Vinet, S. Vitale, T. Vo, H. Vocca, C. Vorvick, D. Voss, W. D. Vousden, S. P. Vyatchanin, A. R. Wade,

L. E. Wade, M. Wade, S. J. Waldman, M. Walker, L. Wallace, S. Walsh, G. Wang, H. Wang, M. Wang, X. Wang, Y. Wang, H. Ward, R. L. Ward, J. Warner, M. Was, B. Weaver, L.-W. Wei, M. Weinert, A. J. Weinstein, R. Weiss, T. Welborn, L. Wen, P. Weßels, T. Westphal, K. Wette, J. T. Whelan, S. E. Whitcomb, D. J. White, B. F. Whiting, K. Wiesner, C. Wilkinson, P. A. Willems, L. Williams, R. D. Williams, A. R. Williamson, J. L. Willis, B. Willke, M. H. Wimmer, L. Winkelmann, W. Winkler, C. C. Wipf, A. G. Wiseman, H. Wittel, G. Woan, J. Worden, J. L. Wright, G. Wu, J. Yablon, I. Yakushin, W. Yam, H. Yamamoto, C. C. Yancey, M. J. Yap, H. Yu, M. Yvert, A. Zadrożny, L. Zangrando, M. Zanolin, J.-P. Zendri, M. Zevin, F. Zhang, L. Zhang, M. Zhang, Y. Zhang, C. Zhao, M. Zhou, Z. Zhou, X. J. Zhu, M. E. Zucker, S. E. Zuraw, and J. Zweizig. Observation of gravitational waves from a binary black hole merger. *Phys. Rev. Lett.*, 116:061102, Feb 2016. doi: 10.1103/PhysRevLett.116.061102. URL https://link.aps.org/doi/10.1103/PhysRevLett.116.061102.

J. G. Ables, D. McConnell, A. A. Deshpande, and M. Vivekanand. Coherent Radiation Patterns Suggested by Single-Pulse Observations of a Millisecond Pulsar. *ApJ*, 475(1):L33–L36, Jan. 1997. doi: 10.1086/310455.

G. Agazie, A. Anumarlapudi, A. M. Archibald, Z. Arzoumanian, P. T. Baker, B. Bécsy, L. Blecha, A. Brazier, P. R. Brook, S. Burke-Spolaor, R. Burnette, R. Case, M. Charisi, S. Chatterjee, K. Chatziioannou, B. D. Cheeseboro, S. Chen, T. Cohen, J. M. Cordes, N. J. Cornish, F. Crawford, H. T. Cromartie, K. Crowter, C. J. Cutler, M. E. Decesar, D. Degan, P. B. Demorest, H. Deng, T. Dolch, B. Drachler, J. A. Ellis, E. C. Ferrara, W. Fiore, E. Fonseca, G. E. Freedman, N. Garver-Daniels, P. A. Gentile, K. A. Gersbach, J. Glaser, D. C. Good, K. Gültekin, J. S. Hazboun, S. Hourihane, K. Islo, R. J. Jennings, A. D. Johnson, M. L. Jones, A. R. Kaiser, D. L. Kaplan, L. Z. Kelley, M. Kerr, J. S. Key, T. C. Klein, N. Laal, M. T. Lam, W. G. Lamb, T. J. W. Lazio, N. Lewandowska, T. B. Littenberg, T. Liu, A. Lommen, D. R. Lorimer, J. Luo, R. S. Lynch, C.-P. Ma, D. R. Madison, M. A. Mattson, A. McEwen, J. W. McKee, M. A. McLaughlin, N. McMann, B. W. Meyers, P. M. Meyers, C. M. F. Mingarelli, A. Mitridate, P. Natarajan, C. Ng, D. J. Nice, S. K. Ocker, K. D. Olum, T. T. Pennucci, B. B. P. Perera, P. Petrov, N. S. Pol, H. A. Radovan, S. M. Ransom, P. S. Ray, J. D. Romano, S. C. Sardesai, A. Schmiedekamp, C. Schmiedekamp, K. Schmitz, L. Schult, B. J. Shapiro-Albert, X. Siemens, J. Simon, M. S. Siwek, I. H. Stairs, D. R. Stinebring, K. Stovall, J. P. Sun, A. Susobhanan, J. K. Swiggum, J. Taylor, S. R. Taylor, J. E. Turner, C. Unal, M. Vallisneri, R. van Haasteren, S. J. Vigeland, H. M. Wahl, Q. Wang, C. A. Witt, O. Young, and Nanograv Collaboration. The NANOGrav 15 yr Data Set: Evidence for a Gravitational-wave Background. *ApJ*, 951(1):L8, July 2023a. doi: 10.3847/2041-8213/acdac6.

G. Agazie, A. Anumarlapudi, A. M. Archibald, Z. Arzoumanian, P. T. Baker, B. Bécsy, L. Blecha, A. Brazier, P. R. Brook, S. Burke-Spolaor, M. Charisi, S. Chatterjee, T. Cohen, J. M. Cordes, N. J. Cornish, F. Crawford, H. T. Cromartie, K. Crowter, M. E. Decesar, P. B. Demorest, T. Dolch, B. Drachler, E. C. Ferrara, W. Fiore, E. Fonseca, G. E. Freedman, N. Garver-Daniels, P. A. Gentile, J. Glaser, D. C. Good, L. Guertin, K. Gültekin, J. S. Hazboun, R. J. Jennings, A. D. Johnson, M. L. Jones, A. R. Kaiser, D. L. Kaplan, L. Z. Kelley, M. Kerr, J. S. Key, N. Laal, M. T. Lam, W. G. Lamb, T. J. W. Lazio, N. Lewandowska, T. Liu, D. R. Lorimer, J. Luo, R. S. Lynch, C.-P. Ma, D. R. Madison, A. McEwen, J. W. McKee, M. A. McLaughlin,

N. McMann, B. W. Meyers, C. M. F. Mingarelli, A. Mitridate, C. Ng, D. J. Nice, S. K. Ocker, K. D. Olum, T. T. Pennucci, B. B. P. Perera, N. S. Pol, H. A. Radovan, S. M. Ransom, P. S. Ray, J. D. Romano, S. C. Sardesai, A. Schmiedekamp, C. Schmiedekamp, K. Schmitz, B. J. Shapiro-Albert, X. Siemens, J. Simon, M. S. Siwek, I. H. Stairs, D. R. Stinebring, K. Stovall, A. Susobhanan, J. K. Swiggum, S. R. Taylor, J. E. Turner, C. Unal, M. Vallisneri, S. J. Vigeland, H. M. Wahl, C. A. Witt, O. Young, and Nanograv Collaboration. The NANOGrav 15 yr Data Set: Detector Characterization and Noise Budget. *ApJ*, 951(1):L10, July 2023b. doi: 10.3847/2041-8213/acda88.

K. Aggarwal, Z. Arzoumanian, P. T. Baker, A. Brazier, M. R. Brinson, P. R. Brook, S. Burke-Spolaor, S. Chatterjee, J. M. Cordes, N. J. Cornish, F. Crawford, K. Crowter, H. T. Cromartie, M. DeCesar, P. B. Demorest, T. Dolch, J. A. Ellis, R. D. Ferdman, E. Ferrara, E. Fonseca, N. Garver-Daniels, P. Gentile, J. S. Hazboun, A. M. Holgado, E. A. Huerta, K. Islo, R. Jennings, G. Jones, M. L. Jones, A. R. Kaiser, D. L. Kaplan, L. Z. Kelley, J. S. Key, M. T. Lam, T. J. W. Lazio, L. Levin, D. R. Lorimer, J. Luo, R. S. Lynch, D. R. Madison, M. A. McLaughlin, S. T. McWilliams, C. M. F. Mingarelli, C. Ng, D. J. Nice, T. T. Pennucci, N. S. Pol, S. M. Ransom, P. S. Ray, X. Siemens, J. Simon, R. Spiewak, I. H. Stairs, D. R. Stinebring, K. Stovall, J. Swiggum, S. R. Taylor, J. E. Turner, M. Vallisneri, R. van Haasteren, S. J. Vigeland , C. A. Witt, W. W. Zhu, and NANOGrav Collaboration. The NANOGrav 11 yr Data Set: Limits on Gravitational Waves from Individual Supermassive Black Hole Binaries. *ApJ*, 880(2):116, Aug. 2019. doi: 10.3847/1538-4357/ab2236.

M. Anholm, S. Ballmer, J. D. E. Creighton, L. R. Price, and X. Siemens. Optimal strategies for gravitational wave stochastic background searches in pulsar timing data. *Phys. Rev. D*, 79(8):084030, Apr. 2009. doi: 10.1103/PhysRevD.79.084030.

Z. Arzoumanian, A. Brazier, S. Burke-Spolaor, S. Chamberlin, S. Chatterjee, B. Christy, J. M. Cordes, N. Cornish, K. Crowter, P. B. Demorest, T. Dolch, J. A. Ellis, R. D. Ferdman, E. Fonseca, N. Garver-Daniels, M. E. Gonzalez, F. A. Jenet, G. Jones, M. L. Jones, V. M. Kaspi, M. Koop, M. T. Lam, T. J. W. Lazio, L. Levin, A. N. Lommen, D. R. Lorimer, J. Luo, R. S. Lynch, D. Madison, M. A. McLaughlin, S. T. McWilliams, D. J. Nice, N. Palliyaguru, T. T. Pennucci, S. M. Ransom, X. Siemens, I. H. Stairs, D. R. Stinebring, K. Stovall, J. K. Swiggum, M. Vallisneri, R. van Haasteren, Y. Wang, and W. Zhu. The NANOGrav Nine-year Data Set: Observations, Arrival Time Measurements, and Analysis of 37 Millisecond Pulsars. *ApJ*, 813(1):65, Nov. 2015. doi: 10.1088/0004-637X/813/1/65.

Z. Arzoumanian, A. Brazier, S. Burke-Spolaor, S. Chamberlin, S. Chatterjee, B. Christy, J. M. Cordes, N. J. Cornish, F. Crawford, H. Thankful Cromartie, K. Crowter, M. E. DeCesar, P. B. Demorest, T. Dolch, J. A. Ellis, R. D. Ferdman, E. C. Ferrara, E. Fonseca, N. Garver-Daniels, P. A. Gentile, D. Halmrast, E. A. Huerta, F. A. Jenet, C. Jessup, G. Jones, M. L. Jones, D. L. Kaplan, M. T. Lam, T. J. W. Lazio, L. Levin, A. Lommen, D. R. Lorimer, J. Luo, R. S. Lynch, D. Madison, A. M. Matthews, M. A. McLaughlin, S. T. McWilliams, C. Mingarelli, C. Ng, D. J. Nice, T. T. Pennucci, S. M. Ransom, P. S. Ray, X. Siemens, J. Simon, R. Spiewak, I. H. Stairs, D. R. Stinebring, K. Stovall, J. K. Swiggum, S. R. Taylor, M. Vallisneri, R. van Haasteren, S. J. Vigeland, W. Zhu, and NANOGrav Collaboration. The NANOGrav 11-

year Data Set: High-precision Timing of 45 Millisecond Pulsars. *ApJS*, 235(2):37, Apr. 2018. doi: 10.3847/1538-4365/aab5b0.

Z. Arzoumanian, P. T. Baker, A. Brazier, P. R. Brook, S. Burke-Spolaor, B. Becsy, M. Charisi, S. Chatterjee, J. M. Cordes, N. J. Cornish, F. Crawford, H. T. Cromartie, M. E. DeCesar, P. B. Demorest, T. Dolch, R. D. Elliott, J. A. Ellis, E. C. Ferrara, E. Fonseca, N. Garver-Daniels, P. A. Gentile, D. C. Good, J. S. Hazboun, K. Islo, R. J. Jennings, M. L. Jones, A. R. Kaiser, D. L. Kaplan, L. Z. Kelley, J. Shapiro Key, M. T. Lam, T. J. W. Lazio, J. Luo, R. S. Lynch, C.-P. Ma, D. R. Madison, M. A. McLaughlin, C. M. F. Mingarelli, C. Ng, D. J. Nice, T. T. Pennucci, N. S. Pol, S. M. Ransom, P. S. Ray, B. J. Shapiro-Albert, X. Siemens, J. Simon, R. Spiewak, I. H. Stairs, D. R. Stinebring, K. Stovall, J. K. Swiggum, S. R. Taylor, M. Vallisneri, S. J. Vigeland, C. A. Witt, and The NANOGrav Collaboration. The NANOGrav 11yr Data Set: Limits on Supermassive Black Hole Binaries in Galaxies within 500Mpc. *arXiv e-prints*, art. arXiv:2101.02716, Jan. 2021.

D. C. Backer. Peculiar Pulse Burst in PSR 1237 + 25. *Nature*, 228(5278):1297–1298, Dec. 1970. doi: 10.1038/2281297a0.

M. Bailes, A. Jameson, F. Abbate, E. D. Barr, N. D. R. Bhat, L. Bondonneau, M. Burgay, S. J. Buchner, F. Camilo, D. J. Champion, and et al. The meerkat telescope as a pulsar facility: System verification and early science results from meertime. *Publications of the Astronomical Society of Australia*, 37:e028, 2020. doi: 10.1017/pasa.2020.19.

L. Barack and C. Cutler. Lisa capture sources: Approximate waveforms, signal-to-noise ratios, and parameter estimation accuracy. *Phys. Rev. D*, 69:082005, Apr 2004. doi: 10.1103/PhysRevD.69.082005. URL https://link.aps.org/doi/10.1103/PhysRevD.69.082005.

P. E. Boynton, E. J. Groth, D. P. Hutchinson, J. Nanos, G. P., R. B. Partridge, and D. T. Wilkinson. Optical Timing of the Crab Pulsar, NP 0532. *ApJ*, 175:217, July 1972. doi: 10.1086/151550.

M. A. Brentjens and A. G. de Bruyn. Faraday rotation measure synthesis. *A&A*, 441(3):1217–1228, Oct. 2005. doi: 10.1051/0004-6361:20052990.

S. Burke-Spolaor, S. R. Taylor, M. Charisi, T. Dolch, J. S. Hazboun, A. M. Holgado, L. Z. Kelley, T. J. W. Lazio, D. R. Madison, N. McMann, C. M. F. Mingarelli, A. Rasskazov, X. Siemens, J. J. Simon, and T. L. Smith. The astrophysics of nanohertz gravitational waves. *A&A*, 27(1):5, June 2019. doi: 10.1007/s00159-019-0115-7.

B. J. Burn. On the depolarization of discrete radio sources by Faraday dispersion. *MNRAS*, 133:67, Jan. 1966. doi: 10.1093/mnras/133.1.67.

A. Chalumeau, S. Babak, A. Petiteau, S. Chen, A. Samajdar, R. N. Caballero, G. Theureau, L. Guillemot, G. Desvignes, A. Parthasarathy, K. Liu, G. Shaifullah, H. Hu, E. van der Wateren, J. Antoniadis, A. S. Bak Nielsen, C. G. Bassa, A. Berthereau, M. Burgay, D. J. Champion, I. Cognard, M. Falxa, R. D. Ferdman, P. C. C. Freire, J. R. Gair, E. Graikou, Y. J. Guo, J. Jang, G. H. Janssen, R. Karuppusamy, M. J. Keith,

M. Kramer, K. J. Lee, X. J. Liu, A. G. Lyne, R. A. Main, J. W. McKee, M. B. Mickaliger, B. B. P. Perera, D. Perrodin, N. K. Porayko, A. Possenti, S. A. Sanidas, A. Sesana, L. Speri, B. W. Stappers, C. Tiburzi, A. Vecchio, J. P. W. Verbiest, J. Wang, L. Wang, and H. Xu. Noise analysis in the European Pulsar Timing Array data release 2 and its implications on the gravitational-wave background search. *MNRAS*, 509(4): 5538–5558, Feb. 2022. doi: 10.1093/mnras/stab3283.

D. J. Champion, G. B. Hobbs, R. N. Manchester, R. T. Edwards, D. C. Backer, M. Bailes, N. D. R. Bhat, S. Burke-Spolaor, W. Coles, P. B. Demorest, R. D. Ferdman, W. M. Folkner, A. W. Hotan, M. Kramer, A. N. Lommen, D. J. Nice, M. B. Purver, J. M. Sarkissian, I. H. Stairs, W. van Straten, J. P. W. Verbiest, and D. R. B. Yardley. Measuring the Mass of Solar System Planets Using Pulsar Timing. *ApJ*, 720(2): L201–L205, Sept. 2010. doi: 10.1088/2041-8205/720/2/L201.

Chime/Frb Collaboration, B. C. Andersen, K. Bandura, M. Bhardwaj, P. J. Boyle, C. Brar, T. Cassanelli, S. Chatterjee, P. Chawla, A. M. Cook, A. P. Curtin, M. Dobbs, F. A. Dong, J. T. Faber, M. Fandino, E. Fonseca, B. M. Gaensler, U. Giri, A. Herrera-Martin, A. S. Hill, A. Ibik, A. Josephy, J. F. Kaczmarek, Z. Kader, V. Kaspi, T. L. Landecker, A. E. Lanman, M. Lazda, C. Leung, H.-H. Lin, K. W. Masui, R. McKinven, J. Mena-Parra, B. W. Meyers, D. Michilli, C. Ng, A. Pandhi, A. B. Pearlman, U.-L. Pen, E. Petroff, Z. Pleunis, M. Rafiei-Ravandi, M. Rahman, S. M. Ransom, A. Renard, K. R. Sand, P. Sanghavi, P. Scholz, V. Shah, K. Shin, S. Siegel, K. Smith, I. Stairs, J. Su, S. P. Tendulkar, K. Vanderlinde, H. Wang, D. Wulf, and A. Zwaniga. CHIME/FRB Discovery of 25 Repeating Fast Radio Burst Sources. *ApJ*, 947 (2):83, Apr. 2023. doi: 10.3847/1538-4357/acc6c1.

J. M. Cordes. Observational limits on the location of pulsar emission regions. *ApJ*, 222:1006–1011, June 1978. doi: 10.1086/156218.

J. M. Cordes. Pulsar timing. II. Analysis of random walk timing noise : application to the Crab pulsar. *ApJ*, 237:216–226, Apr. 1980. doi: 10.1086/157861.

S. Dai, G. Hobbs, R. N. Manchester, M. Kerr, R. M. Shannon, W. van Straten, A. Mata, M. Bailes, N. D. R. Bhat, S. Burke-Spolaor, W. A. Coles, S. Johnston, M. J. Keith, Y. Levin, S. Oslowski, D. Reardon, V. Ravi, J. M. Sarkissian, C. Tiburzi, L. Toomey, H. G. Wang, J. B. Wang, L. Wen, R. X. Xu, W. M. Yan, and X. J. Zhu. A study of multifrequency polarization pulse profiles of millisecond pulsars. *MNRAS*, 449(3):3223–3262, May 2015. doi: 10.1093/mnras/stv508.

K. De and Y. Gupta. A real-time coherent dedispersion pipeline for the giant metrewave radio telescope. *Experimental Astronomy*, 41(1-2):67–93, Feb. 2016. doi: 10.1007/s10686-015-9476-8.

K. De, Y. Gupta, and P. Sharma. Detection of Polarized Quasi-periodic Microstructure Emission in Millisecond Pulsars. *ApJ*, 833(1):L10, Dec. 2016. doi: 10.3847/2041-8213/833/1/L10.

M. Dotti, M. Colpi, F. Haardt, and L. Mayer. Supermassive black hole binaries in gaseous and stellar circumnuclear discs: orbital dynamics and gas accretion. *MNRAS*, 379(3):956–962, Aug. 2007. doi: 10.1111/j.1365-2966.2007.12010.x.

F. D. Drake and H. D. Craft. Second Periodic Pulsation in Pulsars. *Nature*, 220(5164):231–235, Oct. 1968. doi: 10.1038/220231a0.

J. Dyks. Radio pulsar polarization as a coherent sum of orthogonal proper mode waves. *MNRAS*, 488(2): 2018–2040, Sept. 2019. doi: 10.1093/mnras/stz1690.

J. Dyks. Artefacts of circumpolar cartography in radio pulsar polarization. *MNRAS*, 495(1):L118–L122, June 2020. doi: 10.1093/mnrasl/slaa073.

J. Ellis and R. van Haasteren. jellis18/ptmcmcsampler: Official release, Oct. 2017. URL https://doi.org/10.5281/zenodo.1037579.

J. A. Ellis, M. Vallisneri, S. R. Taylor, and P. T. Baker. Enterprise: Enhanced numerical toolbox enabling a robust pulsar inference suite. Zenodo, Sept. 2020. URL https://doi.org/10.5281/zenodo.4059815.

EPTA Collaboration, InPTA Collaboration, J. Antoniadis, P. Arumugam, S. Arumugam, S. Babak, M. Bagchi, A. S. Bak Nielsen, C. G. Bassa, A. Bathula, A. Berthereau, M. Bonetti, E. Bortolas, P. R. Brook, M. Burgay, R. N. Caballero, A. Chalumeau, D. J. Champion, S. Chanlaridis, S. Chen, I. Cognard, S. Dandapat, D. Deb, S. Desai, G. Desvignes, N. Dhanda-Batra, C. Dwivedi, M. Falxa, R. D. Ferdman, A. Franchini, J. R. Gair, B. Goncharov, A. Gopakumar, E. Graikou, J. M. Grießmeier, L. Guillemot, Y. J. Guo, Y. Gupta, S. Hisano, H. Hu, F. Iraci, D. Izquierdo-Villalba, J. Jang, J. Jawor, G. H. Janssen, A. Jessner, B. C. Joshi, F. Kareem, R. Karuppusamy, E. F. Keane, M. J. Keith, D. Kharbanda, T. Kikunaga, N. Kolhe, M. Kramer, M. A. Krishnakumar, K. Lackeos, K. J. Lee, K. Liu, Y. Liu, A. G. Lyne, J. W. McKee, Y. Maan, R. A. Main, M. B. Mickaliger, I. C. Nictu, K. Nobleson, A. K. Paladi, A. Parthasarathy, B. B. P. Perera, D. Perrodin, A. Petiteau, N. K. Porayko, A. Possenti, T. Prabu, H. Quelquejay Leclere, P. Rana, A. Samajdar, S. A. Sanidas, A. Sesana, G. Shaifullah, J. Singha, L. Speri, R. Spiewak, A. Srivastava, B. W. Stappers, M. Surnis, S. C. Susarla, A. Susobhanan, K. Takahashi, P. Tarafdar, G. Theureau, C. Tiburzi, E. van der Wateren, A. Vecchio, V. Venkatraman Krishnan, J. P. W. Verbiest, J. Wang, L. Wang, and Z. Wu. The second data release from the European Pulsar Timing Array. III. Search for gravitational wave signals. *A&A*, 678:A50, Oct. 2023a. doi: 10.1051/0004-6361/202346844.

EPTA Collaboration, InPTA Collaboration, J. Antoniadis, P. Arumugam, S. Arumugam, S. Babak, M. Bagchi, A. S. B. Nielsen, C. G. Bassa, A. Bathula, A. Berthereau, M. Bonetti, E. Bortolas, P. R. Brook, M. Burgay, R. N. Caballero, A. Chalumeau, D. J. Champion, S. Chanlaridis, S. Chen, I. Cognard, S. Dandapat, D. Deb, S. Desai, G. Desvignes, N. Dhanda-Batra, C. Dwivedi, M. Falxa, R. D. Ferdman, A. Franchini, J. R. Gair, B. Goncharov, A. Gopakumar, E. Graikou, J. M. Grießmeier, L. Guillemot, Y. J. Guo, Y. Gupta, S. Hisano, H. Hu, F. Iraci, D. Izquierdo-Villalba, J. Jang, J. Jawor, G. H. Janssen, A. Jessner, B. C. Joshi, F. Kareem, R. Karuppusamy, E. F. Keane, M. J. Keith, D. Kharbanda, T. Kikunaga, N. Kolhe, M. Kramer, M. A. Krishnakumar, K. Lackeos, K. J. Lee, K. Liu, Y. Liu, A. G. Lyne, J. W. McKee, Y. Maan, R. A. Main, M. B. Mickaliger, I. C. Nictu, K. Nobleson, A. K. Paladi, A. Parthasarathy, B. B. P. Perera, D. Perrodin, A. Petiteau, N. K. Porayko, A. Possenti, T. Prabu, H. Q. Leclere, P. Rana, A. Samajdar, S. A. Sanidas, A. Sesana, G. Shaifullah, J. Singha, L. Speri, R. Spiewak, A. Srivastava, B. W.

Stappers, M. Surnis, S. C. Susarla, A. Susobhanan, K. Takahashi, P. Tarafdar, G. Theureau, C. Tiburzi, E. van der Wateren, A. Vecchio, V. V. Krishnan, J. P. W. Verbiest, J. Wang, L. Wang, and Z. Wu. The second data release from the European Pulsar Timing Array. II. Customised pulsar noise models for spatially correlated gravitational waves. *A&A*, 678:A49, Oct. 2023b. doi: 10.1051/0004-6361/202346842.

A. Escala, R. B. Larson, P. S. Coppi, and D. Mardones. The role of gas in the merging of massive black holes in galactic nuclei. ii. black hole merging in a nuclear gas disk. *The Astrophysical Journal*, 630(1): 152, sep 2005. doi: 10.1086/431747. URL https://dx.doi.org/10.1086/431747.

Event Horizon Telescope Collaboration, K. Akiyama, A. Alberdi, W. Alef, K. Asada, R. Azulay, A.-K. Baczko, D. Ball, M. Baloković, J. Barrett, D. Bintley, L. Blackburn, W. Boland, K. L. Bouman, G. C. Bower, M. Bremer, C. D. Brinkerink, R. Brissenden, S. Britzen, A. E. Broderick, D. Broguiere, T. Bronzwaer, D.-Y. Byun, J. E. Carlstrom, A. Chael, C.-k. Chan, S. Chatterjee, K. Chatterjee, M.-T. Chen, Y. Chen, I. Cho, P. Christian, J. E. Conway, J. M. Cordes, G. B. Crew, Y. Cui, J. Davelaar, M. De Laurentis, R. Deane, J. Dempsey, G. Desvignes, J. Dexter, S. S. Doeleman, R. P. Eatough, H. Falcke, V. L. Fish, E. Fomalont, R. Fraga-Encinas, W. T. Freeman, P. Friberg, C. M. Fromm, J. L. Gómez, P. Galison, C. F. Gammie, R. Garc´ia, O. Gentaz, B. Georgiev, C. Goddi, R. Gold, M. Gu, M. Gurwell, K. Hada, M. H. Hecht, R. Hesper, L. C. Ho, P. Ho, M. Honma, C.-W. L. Huang, L. Huang, D. H. Hughes, S. Ikeda, M. Inoue, S. Issaoun, D. J. James, B. T. Jannuzi, M. Janssen, B. Jeter, W. Jiang, M. D. Johnson, S. Jorstad, T. Jung, M. Karami, R. Karuppusamy, T. Kawashima, G. K. Keating, M. Kettenis, J.-Y. Kim, J. Kim, J. Kim, M. Kino, J. Y. Koay, P. M. Koch, S. Koyama, M. Kramer, C. Kramer, T. P. Krichbaum, C.-Y. Kuo, T. R. Lauer, S.-S. Lee, Y.-R. Li, Z. Li, M. Lindqvist, K. Liu, E. Liuzzo, W.-P. Lo, A. P. Lobanov, L. Loinard, C. Lonsdale, R.-S. Lu, N. R. MacDonald, J. Mao, S. Markoff, D. P. Marrone, A. P. Marscher, I. Mart´i-Vidal, S. Matsushita, L. D. Matthews, L. Medeiros, K. M. Menten, Y. Mizuno, I. Mizuno, J. M. Moran, K. Moriyama, M. Moscibrodzka, C. Müller, H. Nagai, N. M. Nagar, M. Nakamura, R. Narayan, G. Narayanan, I. Natarajan, R. Neri, C. Ni, A. Noutsos, H. Okino, H. Olivares, G. N. Ortiz-León, T. Oyama, F. Özel, D. C. M. Palumbo, N. Patel, U.-L. Pen, D. W. Pesce, V. Piétu, R. Plambeck, A. PopStefanija, O. Porth, B. Prather, J. A. Preciado-López, D. Psaltis, H.-Y. Pu, V. Ramakrishnan, R. Rao, M. G. Rawlings, A. W. Raymond, L. Rezzolla, B. Ripperda, F. Roelofs, A. Rogers, E. Ros, M. Rose, A. Roshanineshat, H. Rottmann, A. L. Roy, C. Ruszczyk, B. R. Ryan, K. L. J. Rygl, S. Sánchez, D. Sánchez-Arguelles, M. Sasada, T. Savolainen, F. P. Schloerb, K.-F. Schuster, L. Shao, Z. Shen, D. Small, B. W. Sohn, J. SooHoo, F. Tazaki, P. Tiede, R. P. J. Tilanus, M. Titus, K. Toma, P. Torne, T. Trent, S. Trippe, S. Tsuda, I. van Bemmel, H. J. van Langevelde, D. R. van Rossum, J. Wagner, J. Wardle, J. Weintroub, N. Wex, R. Wharton, M. Wielgus, G. N. Wong, Q. Wu, K. Young, A. Young, Z. Younsi, F. Yuan, Y.-F. Yuan, J. A. Zensus, G. Zhao, S.-S. Zhao, Z. Zhu, J.-C. Algaba, A. Allardi, R. Amestica, J. Anczarski, U. Bach, F. K. Baganoff, C. Beaudoin, B. A. Benson, R. Berthold, J. M. Blanchard, R. Blundell, S. Bustamente, R. Cappallo, E. Castillo-Dom´inguez, C.-C. Chang, S.-H. Chang, S.-C. Chang, C.-C. Chen, R. Chilson, T. C. Chuter, R. Córdova Rosado, I. M. Coulson, T. M. Crawford, J. Crowley, J. David, M. Derome, M. Dexter, S. Dornbusch, K. A. Dudevoir, S. A. Dzib, A. Eckart, C. Eckert, N. R. Erickson, W. B. Everett, A. Faber, J. R. Farah, V. Fath, T. W. Folkers, D. C. Forbes, R. Freund, A. I. Gómez-Ruiz, D. M. Gale, F. Gao, G. Geertsema, D. A. Graham, C. H. Greer, R. Grosslein,

F. Gueth, D. Haggard, N. W. Halverson, C.-C. Han, K.-C. Han, J. Hao, Y. Hasegawa, J. W. Henning, A. Hernández-Gómez, R. Herrero-Illana, S. Heyminck, A. Hirota, J. Hoge, Y.-D. Huang, C. M. V. Impellizzeri, H. Jiang, A. Kamble, R. Keisler, K. Kimura, Y. Kono, D. Kubo, J. Kuroda, R. Lacasse, R. A. Laing, E. M. Leitch, C.-T. Li, L. C. C. Lin, C.-T. Liu, K.-Y. Liu, L.-M. Lu, R. G. Marson, P. L. Martin-Cocher, K. D. Massingill, C. Matulonis, M. P. McColl, S. R. McWhirter, H. Messias, Z. Meyer-Zhao, D. Michalik, A. Montaña, W. Montgomerie, M. Mora-Klein, D. Muders, A. Nadolski, S. Navarro, J. Neilsen, C. H. Nguyen, H. Nishioka, T. Norton, M. A. Nowak, G. Nystrom, H. Ogawa, P. Oshiro, T. Oyama, H. Parsons, S. N. Paine, J. Peñalver, N. M. Phillips, M. Poirier, N. Pradel, R. A. Primiani, P. A. Raffin, A. S. Rahlin, G. Reiland, C. Risacher, I. Ruiz, A. F. Sáez-Mada´in, R. Sassella, P. Schellart, P. Shaw, K. M. Silva, H. Shiokawa, D. R. Smith, W. Snow, K. Souccar, D. Sousa, T. K. Sridharan, R. Srinivasan, W. Stahm, A. A. Stark, K. Story, S. T. Timmer, L. Vertatschitsch, C. Walther, T.-S. Wei, N. Whitehorn, A. R. Whitney, D. P. Woody, J. G. A. Wouterloot, M. Wright, P. Yamaguchi, C.-Y. Yu, M. Zeballos, S. Zhang, and L. Ziurys. First M87 Event Horizon Telescope Results. I. The Shadow of the Supermassive Black Hole. *ApJ*, 875 (1):L1, Apr. 2019. doi: 10.3847/2041-8213/ab0ec7.

D. Foreman-Mackey, D. W. Hogg, D. Lang, and J. Goodman. emcee: The MCMC Hammer. *PASP*, 125 (925):306, Mar. 2013. doi: 10.1086/670067.

R. S. Foster and D. C. Backer. Constructing a Pulsar Timing Array. *ApJ*, 361:300, Sept. 1990a. doi: 10.1086/169195.

R. S. Foster and D. C. Backer. Constructing a Pulsar Timing Array. *ApJ*, 361:300, Sept. 1990b. doi: 10.1086/169195.

U. Giri, B. C. Andersen, P. Chawla, A. P. Curtin, E. Fonseca, V. M. Kaspi, H.-H. Lin, K. W. Masui, K. R. Sand, P. Scholz, T. C. Abbott, F. A. Dong, B. M. Gaensler, C. Leung, D. Michilli, M. Bhardwaj, M. Münchmeyer, A. Pandhi, A. B. Pearlman, Z. Pleunis, M. Rafiei-Ravandi, A. Reda, K. Shin, K. Smith, I. H. Stairs, D. C. Stenning, and S. P. Tendulkar. Comprehensive Bayesian analysis of FRB-like bursts from SGR 1935+2154 observed by CHIME/FRB. *arXiv e-prints*, art. arXiv:2310.16932, Oct. 2023. doi: 10.48550/arXiv.2310.16932.

Y. Gupta, B. Ajithkumar, H. S. Kale, S. Nayak, S. Sabhapathy, S. Sureshkumar, R. V. Swami, J. N. Chengalur, S. K. Ghosh, C. H. Ishwara-Chandra, B. C. Joshi, N. Kanekar, D. V. Lal, and S. Roy. The upgraded GMRT: opening new windows on the radio Universe. *Current Science*, 113(4):707–714, Aug. 2017. doi: 10.18520/cs/v113/i04/707-714.

J. L. Han, R. N. Manchester, and G. J. Qiao. Pulsar rotation measures and the magnetic structure of our Galaxy. *MNRAS*, 306(2):371–380, June 1999. doi: 10.1046/j.1365-8711.1999.02544.x.

J. L. Han, R. N. Manchester, A. G. Lyne, G. J. Qiao, and W. van Straten. Pulsar Rotation Measures and the Large-Scale Structure of the Galactic Magnetic Field. *ApJ*, 642(2):868–881, May 2006. doi: 10.1086/501444.

G. Heald, R. Braun, and R. Edmonds. The Westerbork SINGS survey. II Polarization, Faraday rotation, and magnetic fields. *A&A*, 503(2):409–435, Aug. 2009. doi: 10.1051/0004-6361/200912240.

C. Heiles and D. B. Campbell. Pulsar NP 0532: Properties and Systematic Polarization of Individual Strong Pulses at 430 MHz. *Nature*, 226(5245):529–531, May 1970. doi: 10.1038/226529a0.

S. Hisano, N. Yonemaru, H. Kumamoto, and K. Takahashi. Detailed study of detection method for ultralow frequency gravitational waves with pulsar spin-down rate statistics. *MNRAS*, 487(1):97–103, July 2019. doi: 10.1093/mnras/stz1285.

G. Hobbs. The Parkes Pulsar Timing Array. *Classical and Quantum Gravity*, 30(22):224007, Nov. 2013. doi: 10.1088/0264-9381/30/22/224007.

G. Hobbs. pfits: PSRFITS-format data file processor. Astrophysics Source Code Library, record ascl:2104.013, Apr. 2021.

G. Hobbs, R. Hollow, D. Champion, J. Khoo, D. Yardley, M. Carr, M. Keith, F. Jenet, S. Amy, M. Burgay, S. Burke-Spolaor, J. Chapman, L. Danaia, B. Homewood, A. Kovacevic, M. Mao, D. McKinnon, M. Mulcahy, S. Oslowski, and W. van Straten. The PULSE@Parkes Project: a New Observing Technique for Long-Term Pulsar Monitoring. *PASA*, 26(4):468–475, Nov. 2009. doi: 10.1071/AS09021.

G. Hobbs, A. Archibald, Z. Arzoumanian, D. Backer, M. Bailes, N. D. R. Bhat, M. Burgay, S. Burke-Spolaor, D. Champion, I. Cognard, W. Coles, J. Cordes, P. Demorest, G. Desvignes, R. D. Ferdman, L. Finn, P. Freire, M. Gonzalez, J. Hessels, A. Hotan, G. Janssen, F. Jenet, A. Jessner, C. Jordan, V. Kaspi, M. Kramer, V. Kondratiev, J. Lazio, K. Lazaridis, K. J. Lee, Y. Levin, A. Lommen, D. Lorimer, R. Lynch, A. Lyne, R. Manchester, M. McLaughlin, D. Nice, S. Oslowski, M. Pilia, A. Possenti, M. Purver, S. Ransom, J. Reynolds, S. Sanidas, J. Sarkissian, A. Sesana, R. Shannon, X. Siemens, I. Stairs, B. Stappers, D. Stinebring, G. Theureau, R. van Haasteren, W. van Straten, J. P. W. Verbiest, D. R. B. Yardley, and X. P. You. The International Pulsar Timing Array project: using pulsars as a gravitational wave detector. *Classical and Quantum Gravity*, 27(8):084013, Apr. 2010. doi: 10.1088/0264-9381/27/8/084013.

G. Hobbs, D. Miller, R. N. Manchester, J. Dempsey, J. M. Chapman, J. Khoo, J. Applegate, M. Bailes, N. D. R. Bhat, R. Bridle, A. Borg, A. Brown, C. Burnett, F. Camilo, C. Cattalini, A. Chaudhary, R. Chen, N. D'Amico, L. Kedziora-Chudczer, T. Cornwell, R. George, G. Hampson, M. Hepburn, A. Jameson, M. Keith, T. Kelly, A. Kosmynin, E. Lenc, D. Lorimer, C. Love, A. Lyne, V. McIntyre, J. Morrissey, M. Pienaar, J. Reynolds, G. Ryder, J. Sarkissian, A. Stevenson, A. Treloar, W. van Straten, M. Whiting, and G. Wilson. The Parkes Observatory Pulsar Data Archive. *PASA*, 28(3):202–214, Aug. 2011. doi: 10.1071/AS11016.

G. Hobbs, I. Heywood, M. E. Bell, M. Kerr, A. Rowlinson, S. Johnston, R. M. Shannon, M. A. Voronkov, C. Ward, J. Banyer, P. J. Hancock, T. Murphy, J. R. Allison, S. W. Amy, L. Ball, K. Bannister, D. C. J. Bock, D. Brodrick, M. Brothers, A. J. Brown, J. D. Bunton, J. Chapman, A. P. Chippendale, Y. Chung, D. DeBoer, P. Diamond, P. G. Edwards, R. Ekers, R. H. Ferris, R. Forsyth, R. Gough, A. Grancea,

N. Gupta, L. Harvey-Smith, S. Hay, D. B. Hayman, A. W. Hotan, S. Hoyle, B. Humphreys, B. Indermuehle, C. E. Jacka, C. A. Jackson, S. Jackson, K. Jeganathan, J. Joseph, R. Kendall, D. Kiraly, B. Koribalski, M. Leach, E. Lenc, A. MacLeod, S. Mader, M. Marquarding, J. Marvil, N. McClure-Griffiths, D. McConnell, P. Mirtschin, S. Neuhold, A. Ng, R. P. Norris, J. O'Sullivan, S. Pearce, C. J. Phillips, A. Popping, R. Y. Qiao, J. E. Reynolds, P. Roberts, R. J. Sault, A. E. T. Schinckel, P. Serra, R. Shaw, T. W. Shimwell, M. Storey, A. W. Sweetnam, A. Tzioumis, T. Westmeier, M. Whiting, and C. D. Wilson. A pilot ASKAP survey of radio transient events in the region around the intermittent pulsar PSR J1107-5907. *MNRAS*, 456(4):3948–3960, Mar. 2016. doi: 10.1093/mnras/stv2893.

G. Hobbs, R. N. Manchester, A. Dunning, A. Jameson, P. Roberts, D. George, J. A. Green, J. Tuthill, L. Toomey, J. F. Kaczmarek, S. Mader, M. Marquarding, A. Ahmed, S. W. Amy, M. Bailes, R. Beresford, N. D. R. Bhat, D. C. J. Bock, M. Bourne, M. Bowen, M. Brothers, A. D. Cameron, E. Carretti, N. Carter, S. Castillo, R. Chekkala, W. Cheng, Y. Chung, D. A. Craig, S. Dai, J. Dawson, J. Dempsey, P. Doherty, B. Dong, P. Edwards, T. Ergesh, X. Gao, J. Han, D. Hayman, B. Indermuehle, K. Jeganathan, S. Johnston, H. Kanoniuk, M. Kesteven, M. Kramer, M. Leach, V. Mcintyre, V. Moss, S. Oslowski, C. Phillips, N. Pope, B. Preisig, D. Price, K. Reeves, L. Reilly, J. Reynolds, T. Robishaw, P. Roush, T. Ruckley, E. Sadler, J. Sarkissian, S. Severs, R. Shannon, K. Smart, M. Smith, S. Smith, C. Sobey, L. Staveley-Smith, A. Tzioumis, W. van Straten, N. Wang, L. Wen, and M. Whiting. An ultra-wide bandwidth (704 to 4 032 MHz) receiver for the Parkes radio telescope. *PASA*, 37:e012, Apr. 2020. doi: 10.1017/pasa.2020.2.

G. B. Hobbs, R. T. Edwards, and R. N. Manchester. TEMPO2, a new pulsar-timing package - I. An overview. *MNRAS*, 369(2):655–672, June 2006. doi: 10.1111/j.1365-2966.2006.10302.x.

A. W. Hotan, W. van Straten, and R. N. Manchester. psrchive and psrfits: An open approach to radio pulsar data storage and analysis. *Publications of the Astronomical Society of Australia*, 21(3):302–309, 2004. doi: 10.1071/AS04022.

J. P. Huchra, L. M. Macri, K. L. Masters, T. H. Jarrett, P. Berlind, M. Calkins, A. C. Crook, R. Cutri, P. Erdovgdu, E. Falco, T. George, C. M. Hutcheson, O. Lahav, J. Mader, J. D. Mink, N. Martimbeau, S. Schneider, M. Skrutskie, S. Tokarz, and M. Westover. The 2MASS Redshift Survey—Description and Data Release. *ApJS*, 199(2):26, Apr. 2012. doi: 10.1088/0067-0049/199/2/26.

R. A. Hulse and J. H. Taylor. Discovery of a pulsar in a binary system. *ApJ*, 195:L51–L53, Jan. 1975. doi: 10.1086/181708.

C. D. Ilie, S. Johnston, and P. Weltevrede. Evidence for magnetospheric effects on the radiation of radio pulsars. *MNRAS*, 483(2):2778–2794, Feb. 2019. doi: 10.1093/mnras/sty3315.

F. A. Jenet, S. B. Anderson, V. M. Kaspi, T. A. Prince, and S. C. Unwin. Radio Pulse Properties of the Millisecond Pulsar PSR J0437-4715. I. Observations at 20 Centimeters. *ApJ*, 498(1):365–372, May 1998. doi: 10.1086/305529.

S. Johnston, D. R. Lorimer, P. A. Harrison, M. Bailes, A. G. Lynet, J. F. Bell, V. M. Kaspi, R. N. Manchester, N. D'Amico, L. Nleastrol, and J. Shengzhen. Discovery of a very bright, nearby binary millisecond pulsar. *Nature*, 361(6413):613–615, Feb. 1993. doi: 10.1038/361613a0.

B. C. Joshi, P. Arumugasamy, M. Bagchi, D. Bandyopadhyay, A. Basu, N. Dhanda Batra, S. Bethapudi, A. Choudhary, K. De, L. Dey, A. Gopakumar, Y. Gupta, M. A. Krishnakumar, Y. Maan, P. K. Manoharan, A. Naidu, R. Nandi, D. Pathak, M. Surnis, and A. Susobhanan. Precision pulsar timing with the ORT and the GMRT and its applications in pulsar astrophysics. *Journal of Astrophysics and Astronomy*, 39(4):51, Aug. 2018a. doi: 10.1007/s12036-018-9549-y.

B. C. Joshi, P. Arumugasamy, M. Bagchi, D. Bandyopadhyay, A. Basu, N. Dhanda Batra, S. Bethapudi, A. Choudhary, K. De, L. Dey, A. Gopakumar, Y. Gupta, M. A. Krishnakumar, Y. Maan, P. K. Manoharan, A. Naidu, R. Nandi, D. Pathak, M. Surnis, and A. Susobhanan. Precision pulsar timing with the ORT and the GMRT and its applications in pulsar astrophysics. *Journal of Astrophysics and Astronomy*, 39(4):51, Aug. 2018b. doi: 10.1007/s12036-018-9549-y.

B. C. Joshi, A. Gopakumar, A. Pandian, T. Prabu, L. Dey, M. Bagchi, S. Desai, P. Tarafdar, P. Rana, Y. Maan, N. D. Batra, R. Girgaonkar, N. Agarwal, P. Arumugam, A. Basu, A. Bathula, S. Dandapat, Y. Gupta, S. Hisano, R. Kato, D. Kharbanda, T. Kikunaga, N. Kolhe, M. A. Krishnakumar, P. K. Manoharan, P. Marmat, A. Naidu, S. Banik, K. Nobleson, A. K. Paladi, D. Pathak, J. Singha, A. Srivastava, M. Surnis, S. C. Susarla, A. Susobhanan, and K. Takahashi. Nanohertz gravitational wave astronomy during SKA era: An InPTA perspective. *Journal of Astrophysics and Astronomy*, 43(2):98, Dec. 2022. doi: 10.1007/s12036-022-09869-w.

M. J. Keith, W. Coles, R. M. Shannon, G. B. Hobbs, R. N. Manchester, M. Bailes, N. D. R. Bhat, S. Burke-Spolaor, D. J. Champion, A. Chaudhary, A. W. Hotan, J. Khoo, J. Kocz, S. Oslowski, V. Ravi, J. E. Reynolds, J. Sarkissian, W. van Straten, and D. R. B. Yardley. Measurement and correction of variations in interstellar dispersion in high-precision pulsar timing. *MNRAS*, 429(3):2161–2174, Mar. 2013. doi: 10.1093/mnras/sts486.

M. M. Komesaroff. Possible Mechanism for the Pulsar Radio Emission. *Nature*, 225(5233):612–614, Feb. 1970. doi: 10.1038/225612a0.

M. Kramer and D. J. Champion. The European Pulsar Timing Array and the Large European Array for Pulsars. *Classical and Quantum Gravity*, 30(22):224009, Nov. 2013a. doi: 10.1088/0264-9381/30/22/224009.

M. Kramer and D. J. Champion. The European Pulsar Timing Array and the Large European Array for Pulsars. *Classical and Quantum Gravity*, 30(22):224009, Nov. 2013b. doi: 10.1088/0264-9381/30/22/224009.

H. Kumamoto, Y. Imasato, N. Yonemaru, S. Kuroyanagi, and K. Takahashi. Constraints on ultra-low-frequency gravitational waves with statistics of pulsar spin-down rates. *MNRAS*, 489(3):3547–3552, Nov. 2019. doi: 10.1093/mnras/stz2321.

M. T. Lam, J. M. Cordes, S. Chatterjee, Z. Arzoumanian, K. Crowter, P. B. Demorest, T. Dolch, J. A. Ellis, R. D. Ferdman, E. F. Fonseca, M. E. Gonzalez, G. Jones, M. L. Jones, L. Levin, D. R. Madison, M. A. McLaughlin, D. J. Nice, T. T. Pennucci, S. M. Ransom, X. Siemens, I. H. Stairs, K. Stovall, J. K. Swiggum, and W. W. Zhu. The NANOGrav Nine-year Data Set: Noise Budget for Pulsar Arrival Times on Intraday Timescales. *ApJ*, 819(2):155, Mar. 2016. doi: 10.3847/0004-637X/819/2/155.

C. P. Lee, N. D. R. Bhat, M. Sokolowski, N. A. Swainston, D. Ung, A. Magro, and R. Chiello. Spectral analysis of 22 radio pulsars using ska-low precursor stations. *Publications of the Astronomical Society of Australia*, 39:e042, 2022. doi: 10.1017/pasa.2022.40.

K. J. Lee. Prospects of Gravitational Wave Detection Using Pulsar Timing Array for Chinese Future Telescopes. In L. Qain and D. Li, editors, *Frontiers in Radio Astronomy and FAST Early Sciences Symposium 2015*, volume 502 of *Astronomical Society of the Pacific Conference Series*, page 19, Feb. 2016a.

K. J. Lee. Prospects of Gravitational Wave Detection Using Pulsar Timing Array for Chinese Future Telescopes. In L. Qain and D. Li, editors, *Frontiers in Radio Astronomy and FAST Early Sciences Symposium 2015*, volume 502 of *Astronomical Society of the Pacific Conference Series*, page 19, Feb. 2016b.

D. Lena, A. Robinson, A. Marconi, D. J. Axon, A. Capetti, D. Merritt, and D. Batcheldor. Recoiling Supermassive Black Holes: A Search in the Nearby Universe. *ApJ*, 795(2):146, Nov. 2014. doi: 10.1088/0004-637X/795/2/146.

L. Lentati, P. Alexander, M. P. Hobson, F. Feroz, R. van Haasteren, K. J. Lee, and R. M. Shannon. TEMPONEST: a Bayesian approach to pulsar timing analysis. *MNRAS*, 437(3):3004–3023, Jan. 2014. doi: 10.1093/mnras/stt2122.

K. Liu, E. F. Keane, K. J. Lee, M. Kramer, J. M. Cordes, and M. B. Purver. Profile-shape stability and phase-jitter analyses of millisecond pulsars. *MNRAS*, 420(1):361–368, Feb. 2012. doi: 10.1111/j.1365-2966.2011.20041.x.

G. Lodato, S. Nayakshin, A. R. King, and J. E. Pringle. Black hole mergers: can gas discs solve the 'final parsec' problem? *MNRAS*, 398(3):1392–1402, Sept. 2009. doi: 10.1111/j.1365-2966.2009.15179.x.

D. R. Lorimer and M. Kramer. *Handbook of Pulsar Astronomy*, volume 4. 2004.

D. R. Lorimer, A. J. Faulkner, A. G. Lyne, R. N. Manchester, M. Kramer, M. A. McLaughlin, G. Hobbs, A. Possenti, I. H. Stairs, F. Camilo, M. Burgay, N. D'Amico, A. Corongiu, and F. Crawford. The Parkes Multibeam Pulsar Survey - VI. Discovery and timing of 142 pulsars and a Galactic population analysis. *MNRAS*, 372(2):777–800, Oct. 2006. doi: 10.1111/j.1365-2966.2006.10887.x.

M. E. Lower. A phenomenological model for measuring generalised Faraday rotation. *arXiv e-prints*, art. arXiv:2108.09429, Aug. 2021. doi: 10.48550/arXiv.2108.09429.

M. E. Lower, S. Johnston, R. M. Shannon, M. Bailes, and F. Camilo. The dynamic magnetosphere of Swift J1818.0-1607. *MNRAS*, 502(1):127–139, Mar. 2021. doi: 10.1093/mnras/staa3789.

M. E. Lower, S. Johnston, M. Lyutikov, D. B. Melrose, R. M. Shannon, P. Weltevrede, M. Caleb, F. Camilo, A. D. Cameron, S. Dai, G. Hobbs, D. Li, K. M. Rajwade, J. E. Reynolds, J. M. Sarkissian, and B. W. Stappers. Linear to circular conversion in the polarized radio emission of a magnetar. *arXiv e-prints*, art. arXiv:2311.04195, Nov. 2023. doi: 10.48550/arXiv.2311.04195.

Y. Maan, J. van Leeuwen, and D. Vohl. Fourier domain excision of periodic radio frequency interference. *A&A*, 650:A80, June 2021. doi: 10.1051/0004-6361/202040164.

R. N. Manchester, A. G. Lyne, F. Camilo, J. F. Bell, V. M. Kaspi, N. D'Amico, N. P. F. McKay, F. Crawford, I. H. Stairs, A. Possenti, M. Kramer, and D. C. Sheppard. The Parkes multi-beam pulsar survey - I. Observing and data analysis systems, discovery and timing of 100 pulsars. *MNRAS*, 328(1):17–35, Nov. 2001. doi: 10.1046/j.1365-8711.2001.04751.x.

R. N. Manchester, G. B. Hobbs, A. Teoh, and M. Hobbs. The Australia Telescope National Facility Pulsar Catalogue. *AJ*, 129(4):1993–2006, Apr. 2005. doi: 10.1086/428488.

R. N. Manchester, G. Hobbs, M. Bailes, W. A. Coles, W. van Straten, M. J. Keith, R. M. Shannon, N. D. R. Bhat, A. Brown, S. G. Burke-Spolaor, D. J. Champion, A. Chaudhary, R. T. Edwards, G. Hampson, A. W. Hotan, A. Jameson, F. A. Jenet, M. J. Kesteven, J. Khoo, J. Kocz, K. Maciesiak, S. Oslowski, V. Ravi, J. R. Reynolds, J. M. Sarkissian, J. P. W. Verbiest, Z. L. Wen, W. E. Wilson, D. Yardley, W. M. Yan, and X. P. You. The Parkes Pulsar Timing Array Project. *PASA*, 30:e017, Jan. 2013. doi: 10.1017/pasa.2012.017.

R. N. Manchester, G. Hobbs, M. Bailes, W. A. Coles, W. van Straten, M. J. Keith, R. M. Shannon, N. D. R. Bhat, A. Brown, S. G. Burke-Spolaor, and et al. The parkes pulsar timing array project. *Publications of the Astronomical Society of Australia*, 30:e017, 2013. doi: 10.1017/pasa.2012.017.

M. A. McLaughlin. The North American Nanohertz Observatory for Gravitational Waves. *Classical and Quantum Gravity*, 30(22):224008, Nov. 2013a. doi: 10.1088/0264-9381/30/22/224008.

M. A. McLaughlin. The North American Nanohertz Observatory for Gravitational Waves. *Classical and Quantum Gravity*, 30(22):224008, Nov. 2013b. doi: 10.1088/0264-9381/30/22/224008.

M. A. McLaughlin, A. G. Lyne, D. R. Lorimer, M. Kramer, A. J. Faulkner, R. N. Manchester, J. M. Cordes, F. Camilo, A. Possenti, I. H. Stairs, G. Hobbs, N. D'Amico, M. Burgay, and J. T. O'Brien. Transient radio bursts from rotating neutron stars. *Nature*, 439(7078):817–820, Feb. 2006. doi: 10.1038/nature04440.

D. B. Melrose and R. J. Stoneham. The natural wave modes in a pulsar magnetosphere. *PASA*, 3:120–122, Sept. 1977. doi: 10.1017/S1323358000015010.

B. W. Meyers, S. E. Tremblay, N. D. R. Bhat, C. Flynn, V. Gupta, R. M. Shannon, S. G. Murray, C. Sobey, S. M. Ord, S. Oslowski, B. Crosse, A. Williams, F. Jankowski, W. Farah, V. Venkatraman Krishnan, T. Bateman, M. Bailes, A. Beardsley, D. Emrich, T. M. O. Franzen, B. M. Gaensler, L. Horsley, M. Johnston-Hollitt, D. L. Kaplan, D. Kenney, M. F. Morales, D. Pallot, K. Steele, S. J. Tingay, C. M. Trott, M. Walker, R. B. Wayth, and C. Wu. Hunting for Radio Emission from the Intermittent Pulsar J1107-5907 at Low Frequencies. *ApJ*, 869(2):134, Dec. 2018. doi: 10.3847/1538-4357/aaee7b.

M. Milosavljević and D. Merritt. Formation of Galactic Nuclei. *ApJ*, 563(1):34–62, Dec. 2001. doi: 10.1086/323830.

C. J. Moore, S. R. Taylor, and J. R. Gair. Estimating the sensitivity of pulsar timing arrays. *Classical and Quantum Gravity*, 32(5):055004, Mar. 2015. doi: 10.1088/0264-9381/32/5/055004.

A. Noutsos, A. Karastergiou, M. Kramer, S. Johnston, and B. W. Stappers. Phase-resolved Faraday rotation in pulsars. *MNRAS*, 396(3):1559–1572, July 2009. doi: 10.1111/j.1365-2966.2009.14806.x.

J. T. O'Brien, M. Kramer, A. G. Lyne, D. R. Lorimer, and C. A. Jordan. Sometimes a Pulsar! *Chinese Journal of Astronomy and Astrophysics Supplement*, 6(S2):4–7, Dec. 2006.

L. Oswald, A. Karastergiou, and S. Johnston. Pulsar polarimetry with the Parkes ultra-wideband receiver. *MNRAS*, 496(2):1418–1429, Aug. 2020. doi: 10.1093/mnras/staa1597.

L. S. Oswald, A. Karastergiou, and S. Johnston. Pulsar polarization: a partial-coherence model. *MNRAS*, 525(1):840–853, Oct. 2023. doi: 10.1093/mnras/stad2271.

S. Oslowski, W. van Straten, M. Bailes, A. Jameson, and G. Hobbs. Timing, polarimetry and physics of the bright, nearby millisecond pulsar PSR J04374715 – a single-pulse perspective. *Monthly Notices of the Royal Astronomical Society*, 441(4):3148–3160, 05 2014. ISSN 0035-8711. doi: 10.1093/mnras/stu804. URL https://doi.org/10.1093/mnras/stu804.

A. Parthasarathy, M. Bailes, R. M. Shannon, W. van Straten, S. Oslowski, S. Johnston, R. Spiewak, D. J. Reardon, M. Kramer, V. Venkatraman Krishnan, T. T. Pennucci, F. Abbate, S. Buchner, F. Camilo, D. J. Champion, M. Geyer, B. Hugo, A. Jameson, A. Karastergiou, M. J. Keith, and M. Serylak. Measurements of pulse jitter and single-pulse variability in millisecond pulsars using MeerKAT. *MNRAS*, 502(1):407–422, Mar. 2021. doi: 10.1093/mnras/stab037.

P. C. Peters. Gravitational radiation and the motion of two point masses. *Phys. Rev.*, 136:B1224–B1232, Nov 1964. doi: 10.1103/PhysRev.136.B1224. URL https://link.aps.org/doi/10.1103/PhysRev.136.B1224.

P. C. Peters and J. Mathews. Gravitational Radiation from Point Masses in a Keplerian Orbit. *Physical Review*, 131(1):435–440, July 1963. doi: 10.1103/PhysRev.131.435.

E. Petroff, J. W. T. Hessels, and D. R. Lorimer. Fast radio bursts. *A&A*, 27(1):4, May 2019. doi: 10.1007/s00159-019-0116-6.

S. A. Petrova. On the origin of orthogonal polarization modes in pulsar radio emission. *A&A*, 378:883–897, Nov. 2001. doi: 10.1051/0004-6361:20011297.

B. Posselt, A. Karastergiou, S. Johnston, A. Parthasarathy, M. J. Keith, L. S. Oswald, X. Song, P. Weltevrede, E. D. Barr, S. Buchner, M. Geyer, M. Kramer, D. J. Reardon, M. Serylak, R. M. Shannon, R. Spiewak, and V. Venkatraman Krishnan. The Thousand-Pulsar-Array programme on MeerKAT - VI. Pulse widths

of a large and diverse sample of radio pulsars. *MNRAS*, 508(3):4249–4268, Dec. 2021. doi: 10.1093/mnras/stab2775.

V. Radhakrishnan and D. J. Cooke. Magnetic Poles and the Polarization Structure of Pulsar Radiation. *Astrophys. Lett.*, 3:225, Jan. 1969.

J. M. Rankin. Toward an Empirical Theory of Pulsar Emission. III. Mode Changing, Drifting Subpulses, and Pulse Nulling. *ApJ*, 301:901, Feb. 1986. doi: 10.1086/163955.

D. J. Reardon, A. Zic, R. M. Shannon, V. Di Marco, G. B. Hobbs, A. Kapur, M. E. Lower, R. Mandow, H. Middleton, M. T. Miles, A. F. Rogers, J. Askew, M. Bailes, N. D. R. Bhat, A. Cameron, M. Kerr, A. Kulkarni, R. N. Manchester, R. S. Nathan, C. J. Russell, S. Oslowski, and X.-J. Zhu. The Gravitational-wave Background Null Hypothesis: Characterizing Noise in Millisecond Pulsar Arrival Times with the Parkes Pulsar Timing Array. *ApJ*, 951(1):L7, July 2023a. doi: 10.3847/2041-8213/acdd03.

D. J. Reardon, A. Zic, R. M. Shannon, G. B. Hobbs, M. Bailes, V. Di Marco, A. Kapur, A. F. Rogers, E. Thrane, J. Askew, N. D. R. Bhat, A. Cameron, M. Curylo, W. A. Coles, S. Dai, B. Goncharov, M. Kerr, A. Kulkarni, Y. Levin, M. E. Lower, R. N. Manchester, R. Mandow, M. T. Miles, R. S. Nathan, S. Oslowski, C. J. Russell, R. Spiewak, S. Zhang, and X.-J. Zhu. Search for an Isotropic Gravitational-wave Background with the Parkes Pulsar Timing Array. *ApJ*, 951(1):L6, July 2023b. doi: 10.3847/2041-8213/acdd02.

A. Sesana. Self Consistent Model for the Evolution of Eccentric Massive Black Hole Binaries in Stellar Environments: Implications for Gravitational Wave Observations. *ApJ*, 719(1):851–864, Aug. 2010. doi: 10.1088/0004-637X/719/1/851.

A. Sesana, F. Haardt, and P. Madau. Interaction of massive black hole binaries with their stellar environment. iii. scattering of bound stars. *The Astrophysical Journal*, 686(1):432, oct 2008. doi: 10.1086/590651. URL https://dx.doi.org/10.1086/590651.

R. M. Shannon and J. M. Cordes. Assessing the Role of Spin Noise in the Precision Timing of Millisecond Pulsars. *ApJ*, 725(2):1607–1619, Dec. 2010. doi: 10.1088/0004-637X/725/2/1607.

R. M. Shannon and J. M. Cordes. Pulse Intensity Modulation and the Timing Stability of Millisecond Pulsars: A Case Study of PSR J1713+0747. *ApJ*, 761(1):64, Dec. 2012. doi: 10.1088/0004-637X/761/1/64.

R. M. Shannon, S. Oslowski, S. Dai, M. Bailes, G. Hobbs, R. N. Manchester, W. van Straten, C. A. Raithel, V. Ravi, L. Toomey, N. D. R. Bhat, S. Burke-Spolaor, W. A. Coles, M. J. Keith, M. Kerr, Y. Levin, J. M. Sarkissian, J. B. Wang, L. Wen, and X. J. Zhu. Limitations in timing precision due to single-pulse shape variability in millisecond pulsars. *MNRAS*, 443(2):1463–1481, Sept. 2014. doi: 10.1093/mnras/stu1213.

C. Sotomayor-Beltran, C. Sobey, J. W. T. Hessels, G. de Bruyn, A. Noutsos, A. Alexov, J. Anderson, A. Asgekar, I. M. Avruch, R. Beck, M. E. Bell, M. R. Bell, M. J. Bentum, G. Bernardi, P. Best, L. Birzan, A. Bonafede, F. Breitling, J. Broderick, W. N. Brouw, M. Brueggen, B. Ciardi, F. de Gasperin,

R. J. Dettmar, A. van Duin, S. Duscha, J. Eisloeffel, H. Falcke, R. A. Fallows, R. Fender, C. Ferrari, W. Frieswijk, M. A. Garrett, J. Griessmeier, T. Grit, A. W. Gunst, T. E. Hassall, G. Heald, M. Hoeft, A. Horneffer, M. Iacobelli, E. Juette, A. Karastergiou, E. Keane, J. Kohler, M. Kramer, V. I. Kondratiev, L. V. E. Koopmans, M. Kuniyoshi, G. Kuper, J. van Leeuwen, P. Maat, G. Macario, S. Markoff, J. P. McKean, D. D. Mulcahy, H. Munk, E. Orru, H. Paas, M. Pandey-Pommier, M. Pilia, R. Pizzo, A. G. Polatidis, W. Reich, H. Roettgering, M. Serylak, J. Sluman, B. W. Stappers, M. Tagger, Y. Tang, C. Tasse, S. ter Veen, R. Vermeulen, R. J. van Weeren, R. A. M. J. Wijers, S. J. Wijnholds, M. W. Wise, O. Wucknitz, S. Yatawatta, and P. Zarka. ionFR: Ionospheric Faraday rotation. Astrophysics Source Code Library, record ascl:1303.022, Mar. 2013a.

C. Sotomayor-Beltran, C. Sobey, J. W. T. Hessels, G. de Bruyn, A. Noutsos, A. Alexov, J. Anderson, A. Asgekar, I. M. Avruch, R. Beck, M. E. Bell, M. R. Bell, M. J. Bentum, G. Bernardi, P. Best, L. Birzan, A. Bonafede, F. Breitling, J. Broderick, W. N. Brouw, M. Brüggen, B. Ciardi, F. de Gasperin, R. J. Dettmar, A. van Duin, S. Duscha, J. Eislöffel, H. Falcke, R. A. Fallows, R. Fender, C. Ferrari, W. Frieswijk, M. A. Garrett, J. Grießmeier, T. Grit, A. W. Gunst, T. E. Hassall, G. Heald, M. Hoeft, A. Horneffer, M. Iacobelli, E. Juette, A. Karastergiou, E. Keane, J. Kohler, M. Kramer, V. I. Kondratiev, L. V. E. Koopmans, M. Kuniyoshi, G. Kuper, J. van Leeuwen, P. Maat, G. Macario, S. Markoff, J. P. McKean, D. D. Mulcahy, H. Munk, E. Orru, H. Paas, M. Pandey-Pommier, M. Pilia, R. Pizzo, A. G. Polatidis, W. Reich, H. Röttgering, M. Serylak, J. Sluman, B. W. Stappers, M. Tagger, Y. Tang, C. Tasse, S. ter Veen, R. Vermeulen, R. J. van Weeren, R. A. M. J. Wijers, S. J. Wijnholds, M. W. Wise, O. Wucknitz, S. Yatawatta, and P. Zarka. Calibrating high-precision Faraday rotation measurements for LOFAR and the next generation of low-frequency radio telescopes. *A&A*, 552:A58, Apr. 2013b. doi: 10.1051/0004-6361/201220728.

R. Spiewak, M. Bailes, M. T. Miles, A. Parthasarathy, D. J. Reardon, M. Shamohammadi, R. M. Shannon, N. D. R. Bhat, S. Buchner, A. D. Cameron, F. Camilo, M. Geyer, S. Johnston, A. Karastergiou, M. Keith, M. Kramer, M. Serylak, W. van Straten, G. Theureau, and V. Venkatraman Krishnan. The MeerTime Pulsar Timing Array: A census of emission properties and timing potential. *PASA*, 39:e027, July 2022. doi: 10.1017/pasa.2022.19.

A. Srivastava, S. Desai, N. Kolhe, M. Surnis, B. C. Joshi, A. Susobhanan, A. Chalumeau, S. Hisano, K. Nobleson, S. Arumugam, D. Kharbanda, J. Singha, P. Tarafdar, P. Arumugam, M. Bagchi, A. Bathula, S. Dandapat, L. Dey, C. Dwivedi, R. Girgaonkar, A. Gopakumar, Y. Gupta, T. Kikunaga, M. A. Krishnakumar, K. Liu, Y. Maan, P. K. Manoharan, A. K. Paladi, P. Rana, G. M. Shaifullah, and K. Takahashi. Noise analysis of the Indian Pulsar Timing Array data release I. *Phys. Rev. D*, 108(2):023008, July 2023. doi: 10.1103/PhysRevD.108.023008.

S. N. Sun, N. Wang, W. M. Yan, S. Q. Wang, and J. T. Xie. Wide Bandwidth Observations of PSR J0941−39 and PSR J1107−5907. *arXiv e-prints*, art. arXiv:2311.05183, Nov. 2023.

A. Susobhanan, Y. Maan, B. C. Joshi, T. Prabu, S. Desai, K. Nobleson, S. C. Susarla, R. Girgaonkar, L. Dey, N. D. Batra, Y. Gupta, A. Gopakumar, M. Bagchi, A. Basu, S. Bethapudi, A. Choudhary, K. De, M. A.

Krishnakumar, P. K. Manoharan, A. K. Naidu, D. Pathak, J. Singha, and M. P. Surnis. pinta: The uGMRT data processing pipeline for the Indian Pulsar Timing Array. *PASA*, 38:e017, Apr. 2021. doi: 10.1017/pasa.2021.12.

P. Tarafdar, K. Nobleson, P. Rana, J. Singha, M. A. Krishnakumar, B. C. Joshi, A. K. Paladi, N. Kolhe, N. D. Batra, N. Agarwal, A. Bathula, S. Dandapat, S. Desai, L. Dey, S. Hisano, P. Ingale, R. Kato, D. Kharbanda, T. Kikunaga, P. Marmat, B. A. Pandian, T. Prabu, A. Srivastava, M. Surnis, S. C. Susarla, A. Susobhanan, K. Takahashi, P. Arumugam, M. Bagchi, S. Banik, K. De, R. Girgaonkar, A. Gopakumar, Y. Gupta, Y. Maan, P. K. Manoharan, A. Naidu, and D. Pathak. The Indian Pulsar Timing Array: First data release. *PASA*, 39:e053, Oct. 2022. doi: 10.1017/pasa.2022.46.

S. R. Taylor, E. A. Huerta, J. R. Gair, and S. T. McWilliams. Detecting Eccentric Supermassive Black Hole Binaries with Pulsar Timing Arrays: Resolvable Source Strategies. *ApJ*, 817(1):70, Jan. 2016. doi: 10.3847/0004-637X/817/1/70.

J. P. Vallée. Pulsar-based Galactic Magnetic Map: A Large-Scale Clockwise Magnetic Field with an Anti-clockwise Annulus. *ApJ*, 619(1):297–305, Jan. 2005. doi: 10.1086/426182.

R. van Haasteren and M. Vallisneri. New advances in the Gaussian-process approach to pulsar-timing data analysis. *Phys. Rev. D*, 90(10):104012, Nov. 2014. doi: 10.1103/PhysRevD.90.104012.

W. van Straten and M. Bailes. DSPSR: Digital Signal Processing Software for Pulsar Astronomy. *PASA*, 28 (1):1–14, Jan. 2011. doi: 10.1071/AS10021.

W. van Straten, P. Demorest, and S. Oslowski. Pulsar Data Analysis with PSRCHIVE. *Astronomical Research and Technology*, 9(3):237–256, July 2012. doi: 10.48550/arXiv.1205.6276.

M. Vivekanand. Timescales of Radio Emission in Pulsar J0437-4715 at 327MHz. *ApJ*, 543(2):979–986, Nov. 2000. doi: 10.1086/317141.

M. Vivekanand, J. G. Ables, and D. McConnell. Radio Emission of PSR J0437-4715 at 327 MHz. *ApJ*, 501 (2):823–829, July 1998. doi: 10.1086/305847.

J. Wang, G. Hobbs, M. Kerr, R. Shannon, S. Dai, V. Ravi, A. Cameron, J. F. Kaczmarek, R. Hollow, D. Li, L. Zhang, C. Miao, M. Yuan, S. Wang, S. Zhang, H. Xu, and R. Xu. Probing the Emission States of PSR J1107-5907. *ApJ*, 889(1):6, Jan. 2020. doi: 10.3847/1538-4357/ab5d38.

J. M. Weisberg and J. H. Taylor. The Relativistic Binary Pulsar B1913+16: Thirty Years of Observations and Analysis. In F. A. Rasio and I. H. Stairs, editors, *Binary Radio Pulsars*, volume 328 of *Astronomical Society of the Pacific Conference Series*, page 25, July 2005. doi: 10.48550/arXiv.astro-ph/0407149.

P. Weltevrede. Investigation of the bi-drifting subpulses of radio pulsar B1839-04 utilising the open-source data-analysis project PSRSALSA. *A&A*, 590:A109, May 2016. doi: 10.1051/0004-6361/201527950.

H. Xu, S. Chen, Y. Guo, J. Jiang, B. Wang, J. Xu, Z. Xue, R. Nicolas Caballero, J. Yuan, Y. Xu, J. Wang, L. Hao, J. Luo, K. Lee, J. Han, P. Jiang, Z. Shen, M. Wang, N. Wang, R. Xu, X. Wu, R. Manchester, L. Qian, X. Guan, M. Huang, C. Sun, and Y. Zhu. Searching for the Nano-Hertz Stochastic Gravitational Wave Background with the Chinese Pulsar Timing Array Data Release I. *Research in Astronomy and Astrophysics*, 23(7):075024, July 2023. doi: 10.1088/1674-4527/acdfa5.

J. M. Yao, R. N. Manchester, and N. Wang. A New Electron-density Model for Estimation of Pulsar and FRB Distances. *ApJ*, 835(1):29, Jan. 2017. doi: 10.3847/1538-4357/835/1/29.

N. Yonemaru, H. Kumamoto, S. Kuroyanagi, K. Takahashi, and J. Silk. Gravitational waves from an SMBH binary in M 87. **??***jnlPASJ*, 68(6):106, Dec. 2016. doi: 10.1093/pasj/psw100.

N. Yonemaru, H. Kumamoto, K. Takahashi, and S. Kuroyanagi. Sensitivity of new detection method for ultra-low-frequency gravitational waves with pulsar spin-down rate statistics. *MNRAS*, 478(2):1670–1676, Aug. 2018. doi: 10.1093/mnras/sty976.

N. J. Young, P. Weltevrede, B. W. Stappers, A. G. Lyne, and M. Kramer. On the apparent nulls and extreme variability of PSR J1107-5907. *MNRAS*, 442(3):2519–2533, Aug. 2014. doi: 10.1093/mnras/stu1036.

N. Yunes, K. G. Arun, E. Berti, and C. M. Will. Post-circular expansion of eccentric binary inspirals: Fourier-domain waveforms in the stationary phase approximation. *Phys. Rev. D*, 80(8):084001, Oct. 2009. doi: 10.1103/PhysRevD.80.084001.